TUM – Fakultät für Medizin

Development of an active radiation detector for clinical applications

Dimitrios Topaltzikis

Vollständiger Abdruck der von der Fakultät für Medizin der Technischen Universität München zur Erlangung des akademischen Grades eines Doktors der Naturwissenschaften genehmigten Dissertation.

Vorsitz: Prof. Dr. Gabriele Multhoff

Prüfer der Dissertation: 1. Prof. Dr. Michael J. Atkinson

2. Prof. Dr. Jan J. Wilkens

Die Dissertation wurde am 19.07.2021 bei der Technischen Universität München eingereicht und durch die Fakultät für Medizin am 12.04.2022 angenommen.

Technische Universität München
Fakultät für Medizin

Doktor der Naturwissenschaften (Dr. rer. nat.)

Development of an active radiation detector for clinical applications

Doctoral Dissertation of:
Dimitrios Topaltzikis

Supervisor:
Prof. Dr. Michael John Atkinson

Mentor:
Prof. Dr. Werner Rühm

External Expert:
Prof. Dr. Shawn Bishop

May 2021

The invisible attunement is superior to the visible.
Heracleitus, On the Universe

Abstract

The growing frequency of diagnostic and therapeutic medical procedures based on minimally invasive techniques of interventional radiology, has raised concerns about the occupational radiation doses to medical professionals. Radiation doses heavily depend, among others factors, on the complexity of the procedure and the operator's technique and experience. The very close proximity of medical operators to the incident beam increases significantly the risk for radiation-induced health effects such as malignancies, cataract development and radiation dermatitis. Monitoring the occupational radiation exposure during such procedures, has resulted in the reduction of radiation exposure and long-term dose-dependent health risks. Several types of active and passive radiation detectors have been used by medical professionals to monitor the radiation exposure during occupational ionizing radiation-based procedures. For most personal dosimeters, passive systems are used. Such systems usually accumulate radiation doses over an occupational period of one month. At the end of this period, the accumulated dose is being monitored. This requires the involvement of an accredited dosimetry service and special radiation readers, a practise that does not allow real-time monitoring of the accumulated dose. Although electronic personal dosimeters do offer real-time monitoring capabilities, the size of those devices implies usage limitations. In this study, the first step towards a small x-ray radiation detector is made, to incorporate the benefits of conventional passive dosimeters with the real-time capabilities of electronic personal dosimeters. Hence, an investigation of two independent material systems is presented; a) a system based on AlGaN/GaN high electron mobility transistor (HEMT) and b) a hybrid device consisting of a synthetic thin film diamond layer and a piezoelectric lithium niobate ($LiNbO_3$) surface acoustic wave (SAW) delay line. It was found that both material systems provide the capability of real time monitoring in the medical diagnostic dose-rate regime. The first system showed a rapid signal increase, and a similar signal decrease after the radiation was switched of. Moreover, a linear sensor response with dose rate was observed between about 20 to 50 $\mu Gy/s$. However, it turned out that the signal increase was only in the order of several tens to hundred pA which is difficult to be used in practical environments. In contrast, the second system shows a much more pronounced signal increase under exposure to ionizing radiation. Dependence on dose rate was rather linear with a tendency to saturate at higher dose rates of more than 800 $\mu Gy/s$. The system was tested under typical medical radiation fields (C-arm and CT-scanner) and turned out to be useful. The SAW detection principle offers the unique possibility for wireless remote powering and sensing, features that increase the practicability of such radiation sensor in clinical practice. This study can anticipate promising

applications of the developed prototypes as radiation detectors in radiation fields where lightweight, compact devices and modification flexibility matters in medical applications.

Zusammenfassung

Die zunehmende Häufigkeit diagnostischer und therapeutischer auf minimalinvasiven Techniken der interventionellen Radiologie basierenden medizinischen Verfahren hat Besorgnis hinsichtlich der berufsbedingten Strahlungsdosen für medizinische Fachkräfte erregt. Strahlungsdosen hängen u. a. stark von der Komplexität des Verfahrens sowie von technischer Kompetenz und Erfahrung des Bedienungspersonals ab. Die unmittelbare Nähe der medizinischen Fachkräfte zum Strahlungsfeld erhöht das Risiko für strahleninduzierte gesundheitliche Auswirkungen wie z.B. Malignome, Kataraktentwicklung und Strahlungsdermatitis. Die Überwachung der berufsbedingten Strahlenexposition während oben genannter Verfahren hat zu einer Verringerung der Strahlenexposition und somit der langfristigen dosisabhängigen Gesundheitsrisiken geführt. Verschiedene Arten von aktiven und passiven Strahlungsdetektoren sind in Gebrauch, um die Strahlenexposition bei der Anwendung von auf ionisierender Strahlung basierenden Verfahren zu überwachen. Für die meisten Dosimeter werden passive Systeme verwendet. Normalerweise akkumulieren derartige Systeme Strahlungsdosen über einen Zeitraum von einem Monat. Am Ende dieses Zeitraums wird die akkumulierte Dosis dokumentiert. Dies erfordert den Einsatz eines akkreditierten Dosimetriedienstes und spezieller Auslesegeräte, ein Verfahren, das keine Echtzeitüberwachung der akkumulierten Dosis ermöglicht. Zwar bieten elektronische Personendosimeter Echtzeitüberwachungsfunktionen, deren Nutzung ist jedoch durch die Größe dieser Geräte eingeschränkt. In dieser Studie wurde der erste Schritt in Richtung eines kleinen Röntgenstrahlungsdetektors gemacht, um die Vorteile herkömmlicher passiver Dosimeter mit der Echtzeitfähigkeit elektronischer Dosimeter zu verbinden. Dazu wurde eine Untersuchung zweier unabhängiger Materialsysteme durchgeführt: a) ein System basierend auf einem AlGaN/GaN Transistor mit hoher Elektronenmobilität (HEMT) und b) ein Hybridsystem, das aus einer dünnen synthetischen Diamantschicht und einer piezoelektrischen Verzögerungsleitung für akustische Lithiumniobat (LiNbO3)-Oberflächenwellen (SAW) besteht. Es wurde festgestellt, dass im Prinzip beide Materialsysteme die Fähigkeit zur Echtzeitüberwachung im medizinisch-diagnostischen Dosisleistungsregime bieten. Das erste System zeigte einen schnellen Signalanstieg und einen ähnlich schnellen Signalabfall nach dem Ausschalten der Strahlenquelle. Außerdem wurde eine lineare Sensorantwort in Abhängigkeit von der Dosisleistung zwischen etwa 20 und 50 uGy/s beobachtet. Es stellte sich jedoch heraus, dass der Signalanstieg nur in der Größenordnung von mehreren zehn bis hundert pA lag, was in der täglichen Arbeitspraxis schwierig anzuwenden ist. Im Gegensatz dazu zeigt das zweite System einen viel stärkeren Signalanstieg unter Einwirkung ionisierender Strahlung. Die Abhängigkeit von der Dosisleistung war annähernd linear mit

einer Tendenz zur Sättigung bei höheren Dosisleistungen von mehr als 800 uGy/s. Das System wurde unter typischen medizinischen Bestrahlungsfeldern (C-Arm und CT-Scanner) getestet und erwies sich als nützlich. Abschließend sei betont, dass das SAW-Prinzip die einzigartige Möglichkeit bietet, das gemessene Signal drahtlos auszulesen, was einen auf diesem Prinzip basierenden Sensor für Anwendungen in der klinischen Praxis besonders attraktiv erscheinen lässt. Die im Rahmen dieser Arbeit erzielten Ergebnisse zeigen, dass insbesondere das zweite untersuchte System der Kombination einer dünnen Diamantschicht und einer SAW-Verzögerungsleitung großes Potential für die Entwicklung von leichten und kompakten Strahlungsdetektoren bei medizinischen Anwendungen aufweist.

Contents

Introduction 1

Recent years have brought an increase in medical procedures with the use of ionizing radiation as diagnostic and therapeutic tool, for example in vascular and interventional radiology (IR), interventional cardiology, orthopaedics, urology and interventional neuroradiology (INR) [1]. The minimally invasive procedures in these fields have been benefited from fluoroscopy-guided procedures, raising concerns about the radiation exposures and associated health risks to medical operators and patients [2]. The inevitable occupational radiation dose that medical operators are exposed during interventional therapeutic or diagnostic procedures, is affected by various factors such as procedure time, patient condition and complexity of the procedure [3]. As the number of fluoroscopically guided interventional procedures have increased over time [4], the necessity for radiation monitoring increases concurrently and attention should be given to the medical professionals that daily utilize such procedures, from their first training up to their retirement [1]. Radiation monitoring of medical professionals is based on active personal dosimeters, such as passive thermoluminescence dosimeters (TLDs) and electronic personal dosimeters, which are the most widely used solutions among medical professionals [5]. Nevertheless, crucial drawbacks in terms of precision, real-time readout, flexibility and operational costs, in combination with the continuous improvement of semiconductor materials, have increased the interest for alternative solutions in radiation detection and dosimetry [6].

Wide band-gap III-V compound semiconductor materials like GaAs [7], GaN [8], synthetic diamond [9][10], as well as structures like the high mobility AlGaN/GaN transistor [11][12] and radiation-sensitive field-effect transistor (RADFET) [13] have been introduced as alternative solutions for radiation detection applications based on their physical properties, compared to other semiconductors [14]. Semiconductor-based detectors exhibit higher material density than gas detectors [6], as well as lower ionization energy when compared to gas detectors and scintillators [15]. In principle, there is absence of internal amplification of the radiation-induced signal, with the exception of materials that have the two-dimensional electron system (2DES) channel. Thus, the small output signal and the additional electronic components that accompany such detectors result in the increase of manufacturing costs [16]. The capability of such materials to be combined with simple electronic circuits [13], could overcome the obstacle of passive readout (for the thermoluminescence dosimeters) and size limitations (for the electronic personal dosimeters). Allthough III-V compound semiconductors have been suggested as radiation detection materials, they exhibit low displacement energy and are thus subject to defects during irradiation [7][17]. In contrast, such defects are absent from diamond as this material exhibits a higher displacement energy, thus resulting in radiation hardness compared to other semiconductor materials [18]. Despite this remarkable characteristic, a comparison with other semiconductor materials shows that diamond exhibits very low mass attenuation coefficient for x-rays, due to low atomic number ($Z = 6$) and mass density ($\rho = 3.515\ g \cdot cm^{-3}$) [19]. This causes diamond devices to be more efficient for very high dose-rates, while for lower dose-rates the coupling of additional equipment such as radiation converters is required [20].

Another approach that has been suggested as radiation detection solution with capabilities for wireless real-time readout are surface acoustic wave (SAW) devices [21][22]. The use of SAW-based devices offers relatively low production costs [23][24], in combination with high sensitivity for very low conductivities [25]. Previous studies about the operation of SAW delay-lines in radiation environment concluded that such devices are radiation hard and there is no modification of the delay-line as result of exposure to ionizing radiation [26]. SAW-based radiation detectors could follow the operation principles of sandwich structures. Such structures have been extensively studied in the field of semiconductors, for example the interaction of SAWs with the 2DES channel in GaAs/AlGaAs heterostructures, through the dependence of attenuation and sound velocity of the propagating SAW as function of conductivity change [27][28][29], as well as interactions of SAW with graphene layer [30].

The present work investigates the idea of combining radiation hard semiconductor structures and materials, such as AlGaN/GaN high-electron mobility transistor (HEMT) and heteroepitaxial synthetic diamond, with SAW structures according to the operational principles of a sandwich structure, for low-energy continuous x-ray fields in the keV range, which are typical in the medical diagnostic procedures. The investigated AlGaN/GaN HEMT system was commercially fabricated on custom-made wafer that was developed specifically for this project. This approach was chosen to reduce instabilities that were observed in the first prototypes produced in the clean room of the University of Augsburg. The fabrication process that was followed is the standard photolithography in clean room environment [31][32]. Upon completion the HEMT devices were characterized under an optical microscope in order to confirm their physical condition of different parts. Resulting HEMTs were further evaluated for their electrical properties, using common current-voltage characteristics. Subsequently, the promising devices were characterized under low-energy x-rays at normal-off mode, in order to evaluate the radiation induced response from HEMTs. In this stage, the goal was to find the HEMTs with the proper response under irradiation and combine them with SAW structures for further investigation. Parallel to this approach, an independent fabrication of synthetic diamonds was performed using the fabrication technique of hetero-epitaxy [33][34][35]. In parallel, standard SAW devices were fabricated using photolithography and evaluated in terms of frequency domain characterization. Next, the final assembly of the sandwich structure was performed under clean room environment. The ready hybrid-devices were initially irradiated under the same technical x-ray configuration as the HEMT devices, with the resulting devices to be evaluated under ^{137}Cs gamma-source. Finally, the performance of the resulting hybrid-device was investigated using medical diagnostic radiation equipment, in order to evaluate the capabilities of such material combinations under real medical radiological fields.

The present thesis is divided into the following parts; in **Chapter 2** the necessary theoretical background is developed. Specifically, in **(Section 2.1)** there is a discussion of the AlGaN/GaN Material System, followed by the diamond **(Section 2.2)** and the SAWs **(Section 2.3)**. The theoretical part concludes with a brief discussion about the dosimeters that are currently being used from medical professionals **(Section 2.4)**. In **Chapter 3**, the components and materials that were used through-out this thesis are discussed **(Section 3.1)**, providing descriptions about the experimental methods and configurations that were employed **(Section 3.2)**. Subsequently, in **Chapter 4** the experimental results for both (AlGaN/GaN and SAW) approaches are scrutinized, accompanied by discussion of findings and solutions reported in the literature. Finally, the conclusions of this investigation are presented **(Chapter 5)** followed by the necessary **References**, an **Appendix** with textbook knowledge about the interaction of photons with matter, as well as a **List of Figures**, **List of Tables** and **Acknowledgements**.

Finally it should be mentioned that part of this study was published in a peer-reviewed journal on March 29th, 2021.[1]

[1] Dimitrios Topaltzikis, Marek Wielunski, Andreas L. Hörner, Matthias Küß, Alexander Reiner, Theodor Grünwald, Matthias Schreck, Achim Wixforth, and Werner Rühm, "Detection of x rays by a surface acoustic delay line in contact with a diamond crystal", Applied Physics Letters 118, 133501 (2021) https://doi.org/10.1063/5.0047043

Theoretical Background 2

This chapter provides the necessary theoretical background of different components that were used in this thesis. Fundamental theoretical description of matter interaction with radiation can be found in the Appendix section.

2.1 AlGaN/GaN Material System

2.1.1 Properties

An overview of the crystal structure of gallium nitride (GaN) is shown in Figure 2.1. Gallium (Ga) assembles a tetrahedral bond structure to nitrogen (N) under a theoretical sp^3 hybridization angle of 109.47°. The combination of such tetrahedral structures results in the formation of either binary cubic zincblende (β-GaN) or a hexagonal wurtzite (α-GaN) crystal structure [32][36][37]. The former is a metastable crystal structure while on the contrary the latter is a stable structure that was used in this study. The sp^3 hybridization corresponds to an ideal wurtzite lattice with zero net total polarity, as consequence of the symmetrical binary system of dipolar bonds. Despite the fact that Ga and N differ in Pauling electronegativity, the geometry of these bonds allows to construct a wurtzite structure without a macroscopic polarization [32].

The consideration of wurtzite lattice as finite unit increases the contribution to the total crystal energy of surface charges. The break of tetrahedral symmetry as consequence of the abrupt termination of the crystal lattice, causes distortion of the crystal as the charge round the structure countervails for the boundaries [32]. This leads to the counterbalance of positive and negative charge of wurtzite structure, hence driving the crystal to new point of equilibrium causing the break down of tetrahedral symmetry, resulting in the spontaneous polarization of the crystal at zero strain [32]. The

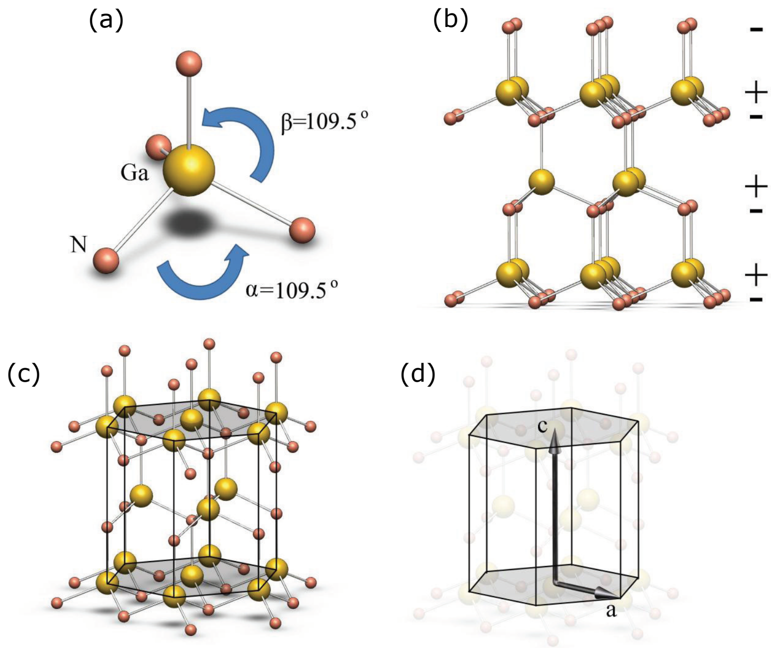

Figure 2.1: Crystal structure of GaN (from Ref. [32]). **(a)** Theoretical sp^3 hybridization angle of 109.47° of tetrahedral bond structure formed between Ga and N. **(b)** Creation of periodic dipoles due to differences in electronegativity of the atoms. **(c)** Binary hexagonal structure of the thermodynamically stable form of GaN. **(d)** Wurtzite crystal unit cell with unit vectors c and a.

electrical properties of the device that is fabricated on top of this layer of GaN are strongly affected by the vector of spontaneous polarization, as the above mentioned difference in electronegativity induces a polar behaviour in each GaN crystal structure [38].

Depending on the selection of the direction of crystal growth, different physical properties are created as consequence of the polar effects of the material; layers that start growing from Ga-atoms ending with a surface of N-atoms, typically called *N-face*, as well as conversely, layers grown starting from N-atoms that end with a surface of Ga-atoms, so called *Ga-face*. Figure 2.2 shows the schematic drawing of the above mentioned faces.

At this point, it should be mentioned that throughout this study, heterostructures of Ga-face <0001> gallium nitride (GaN) and aluminium gallium nitride/gallium nitride (AlGaN/GaN) grown on sapphire (Al_2O_3) were investigated, similar to Ref. [32].

The advantages of GaN over the dominant materials typically used in the field of semiconductors, like Si and SiC, are quantitatively presented in Table 2.1. In more detail, the wide band-gap of GaN typically results in

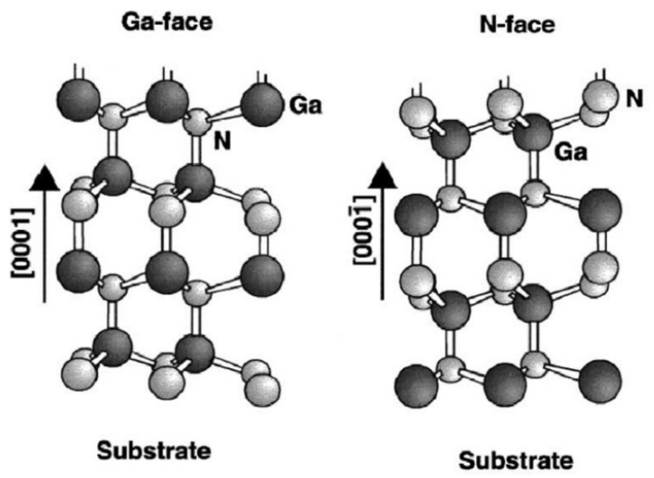

FIGURE 2.2: Sketch of the crystal structure of wurtzite Ga-face and N-face layer for GaN (from Ref. [39]).

Parameter	Silicon (Si)	GaN	SiC
Band Gap (eV)	1.12	3.39	3.26
Breakdown Field (MV/cm)	0.23	3.3	2.2
Saturation Velocity (cm/s)	0.8×10^7	2.5×10^7	2.0×10^7
Electron Mobility ($cm^2/V \cdot s$)	~ 1400	1500	950
Permittivity ϵ_r	11.8	9	9.7
Thermal Conductivity ($W/cm \cdot K$)	1.5	1.3	3.8
Johnson's figure of merit	1	20	27.5

Table 2.1: Material Properties of Silicon, GaN and SiC (from Ref. [40][41]).

a high breakdown voltage, as a result of the high electric-field (Breakdown Field) that is required to initiate band-to-band impact ionization. From the combination of high electric-field with high carrier velocity saturation, *Johnson's figure of merit (JM)* index could be extracted that indicates the power and frequency limit of a material based solely on its physical properties, as shown in Equation (2.1) [41].

$$JM = \frac{E_{breakdown} \cdot u_{saturation}}{2\pi} \tag{2.1}$$

Moreover, as the energy band gap of a material relates to the strength of chemical bonds between the atoms in the crystal lattice, it indicates that higher energy band gap materials like GaN, are less susceptible to radiation effects [38].

Recently, GaN has become more attractive compared to Si and SiC, due to its ability to establish heterostructures, that has enabled the fabrication of High Electron Mobility Transistors (HEMTs), which is part of the subject of this study [40]. Such devices are based on a heterostructure bounded by materials of high-energy gap, that permit the integration of the high carrier concentration including in the doped-layer, with the high mobility of the channel that is located on the intrinsic semiconductor. Historically, the initial HEMT devices were developed on an AlGaAs-GaAs heterostructure accompanied by an n-doped layer *(barrier layer)* of AlGaAs on top and an intrinsic layer *(buffer layer)* of GaAs on the bottom [38]. In case of GaN, the crystal structure from Figure 2.1(a) results in piezoelectric properties that in turn results in very high conductivity compared to other semiconductor materials. These piezoelectric properties are mainly caused by the displacement of charged elements in the lattice. Presuming the crystal lattice is subjected to strain, a diminutive shift of the atoms in the lattice will be caused that will result in the generation of an electric field. As GaN is an n-doped system, by growing a layer of AlGaN on top of this buffer layer, a Ga-face polarity GaN−AlGaN heterostructure is created that induces a compensating **two dimensional electron gas (2DEG)** [32][40]. The channel of 2DEG is highly conductive, mainly due to the confinement of a large amount of electrons to a very thin region at the interface. The mobility of the electrons increases, as result of this enclosure, from about 1000 $cm^2/V \cdot s$ in slacked GaN up-to 2000 $cm^2/V \cdot s$ in the 2DEG channel [40].

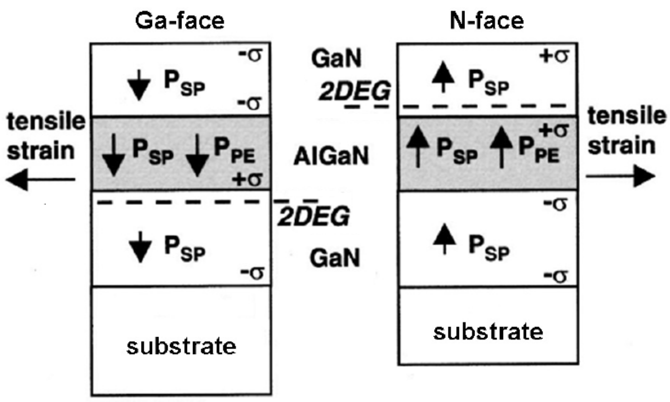

Figure 2.3: Creation of a 2DEG for Ga-face and N-face topology with the induced interface charge (from Ref. [38]). It should be distinguished that P_{SP} correspond to spontaneous and P_{PE} to piezoelectric polarization vectors.

The high carrier concentration between the layers, appears for only one combination in each topology, as shown in Figure 2.3. Hence, the arrangement of layers for Ga-face will have an AlGaN barrier layer on top of the GaN buffer layer, with the tensile strain on the AlGaN that engenders the 2DEG on the upper interface of GaN layer. On the contrary, for N-face the channel of 2DEG is located between the GaN channel on top of the structure and the AlGaN barrier layer.

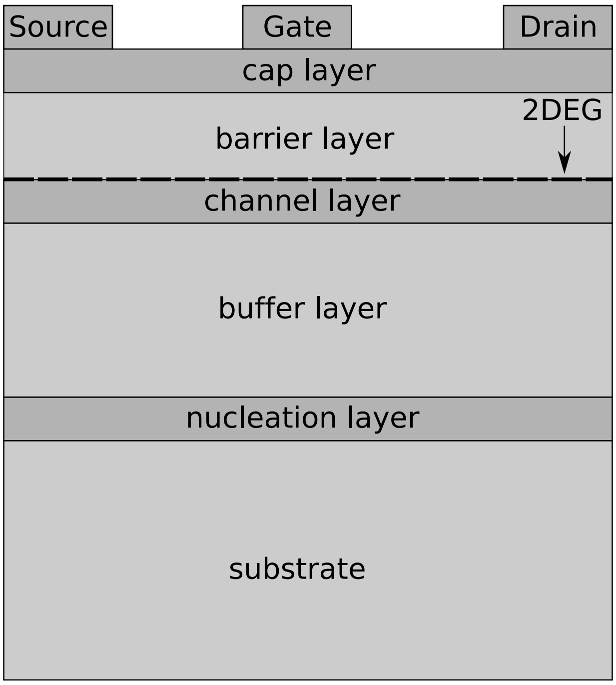

FIGURE 2.4: Cross Section of classical structure for AlGaN/GaN HEMT. (not to scale)

In Figure 2.4 the conventional structure for Ga-face AlGaN/GaN HEMT devices is presented. The main heterostructure is growth by molecular-beam-epitaxy (MBE) or metal-organic chemical vapor deposition (MOCVD) above the substrate [42], with the three contacts of source, gate and drain on top to be fabricated by photolithography [43]. The substrates on which HEMTs are currently grown are silicon [44], sapphire [45], silicon carbide [46] and GaN [47].

In more detail, the substrate should exhibit high thermal stability and close crystal lattice matching with the AlGaN/GaN layer, at reasonable cost [40]. The nucleation layer that is located between the substrate and the buffer layer, scales down the defects propagation from the substrate to the active layers, due to lattice mismatch [16]. Moreover, the channel layer reduces the residual scattering that is created as consequence of interface roughness, improving the confinement of electrons and escalating electron mobility [38][48]. The barrier layer that is grown on top of the channel layer exhibits a higher energy band-gap and smaller electron affinity than the channel layer [49]. The polarization difference as well as the conduction offset between the barrier and channel layer, results in the creation of a potential quantum well where the electrons are trapped inside, thus creating the channel of 2DEG. The contacts on top of the protective layer (cap layer) are made of metal (Al, Au, Ni or Ti) according to the preferred characteristics and desired properties of the device. Most preferred example is the formation of drain and source contacts or *ohmic contacts* by evaporating Ti/Al/Ni/Au followed by annihilation at high temperature to attain the connection with the layer [38]. Various comprehensive and thorough fabrication methods, as well as the physical properties of HEMT devices are reported in Ref. [50].

2.1.2 Ionizing Radiation and AlGaN/GaN High Electron Mobility Transistors

AlGaN/GaN HEMTs are recognized as promising solutions for radiation-harsh environments such as those encountered in space applications, due to their relative radiation hardness [51]. Moreover, the soaring demand for dosimetry solutions in modern medical environment, like in brachytherapy or interventional medicine, with small energy efficient detectors, has already triggered research towards that direction [12]. The use of HEMT structures overcomes the physical limitations of GaN concerning its interaction with ionizing radiation. More precisely, the low absorption coefficient of GaN impacts the ability of the material in x-ray detection [8]. As the absorption of x-rays is substantial for photon energies between 10 and 20 keV, in combination with the enormous absorption reduction at higher energies [52], multilayer GaN structures are required to increase the incoming photons. As it was mentioned before, AlGaN/GaN HEMT devices have already been proposed and investigated as GaN-based multilayer structure for ionizing radiation detection with promising results for x-ray dosimetry [53].

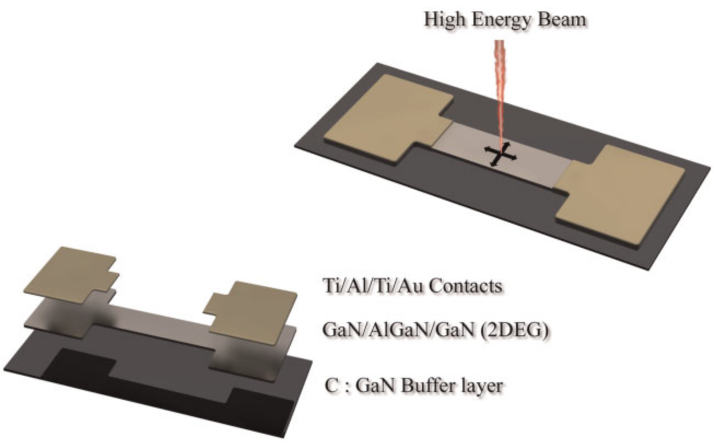

Figure 2.5: Schematic illustration of GaN/AlGaN/GaN HEMT with the related 2DEG channel (from Ref. [11]).

It has been suggested that the radiation tolerance of GaN-based HEMTs is due to the intrinsic defectiveness of the GaN material, with radiation-induced defects to have almost no impact [54]. In addition, considering the high threshold energy for atomic displacement of GaN compared with other III-V materials [55], there are proportionately fewer atoms to be displaced [56]. As for this device's performance, it was reported that unfocused x-rays shift the characteristic I-V curves with increasing dose-rate, indicating change in gate leakage current and source drain current [57].

In contrast, investigation of AlGaN/GaN High Electron Mobility Transistors with focused x-ray beams (Figure 2.5) from Ref. [11], showed extremely large sensitivities for medical dose-rate regimes, as shown in Figure 2.6. The AlGaN/GaN heterointerface creates an intrinsic amplification of the collected number of electrons, through the 2DEG channel, thus resulting in the reported sensitivities [11].

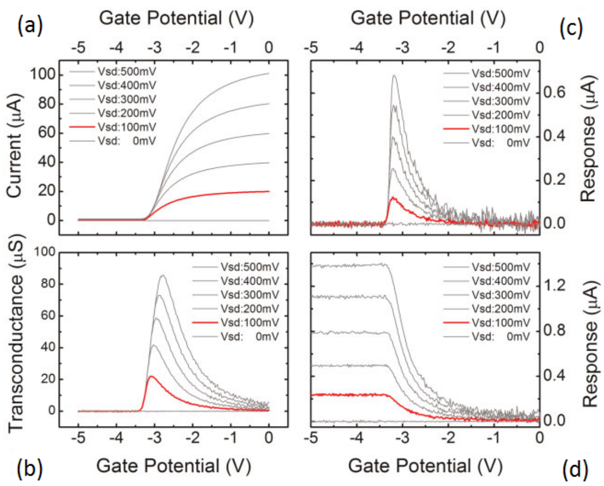

FIGURE 2.6: Characteristic curves of an AlGaN/GaN HEMT-based device under focused radiation beam (from Ref. [11]).

2.2 Diamond

2.2.1 Properties

Diamond is the hardest known natural material. Diamond lattice is constructed by tetrahedrally bonded sp^3 carbon atoms, which form a face-centred cubic (fcc) crystal structure as shown in Figure 2.7. The conventional structure is formed by two interpenetrating fcc lattices, permitting each carbon atom to form four covalent bonds. It is the lattice arrangement that results in the extreme stability of this allotrope of carbon.

Diamond is categorised as electrical insulator at room temperature due to its extremely high thermal conductivity, in combination with very high

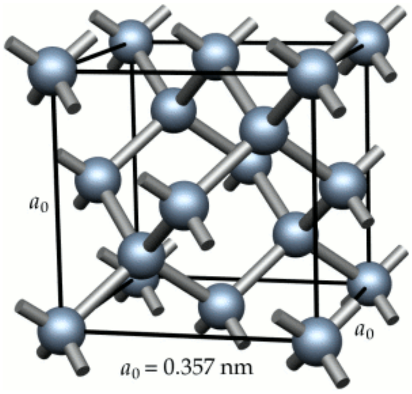

Figure 2.7: Diamond structure with characteristic cubic edge length α_0 at room temperature [58].

electrical resistivity or very low electrical conductivity [1].

Property	Diamond	Silicon (Si)
Band Gap (eV)	5.5	1.12
Breakdown Field (V/cm)	10^7	3×10^5
Electron Mobility ($cm^2/V \cdot s$)	1800	~ 1400
Hole Mobility ($cm^2/V \cdot s$)	1200	450
Saturation Velocity (cm/s)	2.2×10^7	0.8×10^7
Atomic Number	6	14
Dielectric Constant	5.7	11.9
Energy to create e-h Pair (eV)	13	3.6
Resistivity ($\Omega \cdot cm$)	$> 10^{11}$	2.3×10^5
Thermal Conductivity ($W \cdot m^{-1} \cdot K^{-1}$)	~ 2000	150
Intrinsic Carrier Density (cm^{-3})	$< 10^3$	1.5×10^{10}
Wigner Energy (eV)	43	13-20

Table 2.2: Properties of diamond and silicon (Si) at room temperature [6][59][60].

Many of the properties (see Table 2.2) of diamond, promote it as a promising candidate for semiconductors applications against silicon (Si), a material that is widely used for radiation detection. Diamond exhibits a higher band gap energy than silicon, resulting in a lower leakage current which implies less noise at the same bias voltage in high radiation environments. Its high thermal conductivity gives diamond the advantage of operation without the necessity for active cooling. Moreover, its atomic number ($Z_C = 6$) which is very close to the mean atomic number of human

[1] Electrical resistivity is the reciprocal of electrical conductivity

soft tissue ($Z_{tissue} = 6.5$), characterizes diamond as almost tissue equivalent.

One of the significant advantages of diamond, in comparison with other semiconductor materials such as silicon (Si), gallium nitride (GaN), gallium arsenide (GaAs) and germanium (Ge), is the high Wigner Energy (the energy needed to remove an atom from its lattice site) that results in the radiation hardness in radiation harsh environments [6][60]. The benefit from high resistance to radiation damage may allow for the development of detectors that do not require recalibration or replacement. Thus, diamond is an excellent material for radiation detection applications in space, nuclear facilities, as well as in medicine.

2.2.2 Synthesis

The first attempts to synthesize diamond, date back to the 1880s when researchers understood that diamond was a high temperature, high pressure form of carbon. Despite the fact that many research groups were claiming the synthesis of diamond in a laboratory environment, it was not until 1955 when researchers at General Electric Laboratories announced the synthesis of diamond, using a high-pressure-high-temperature (HPHT) laboratory process [61].

Even thought that the HPHT process resulted in remunerative diamond industry, it was the development of the Chemical Vapor Deposition (CVD) process in the early 1980s that expanded the field of diamond applications. Moreover, the attempts of diamond replacing silicon (Si) as alternative band gap semiconductor material for electronic devices, resulted in the increase of funding towards the CVD method. Despite the fact that diamond has not managed to substitute silicon (Si), the ongoing research has revived the use of CVD diamond in electronic devices and sensors [61].

The CVD process involves the deposition of solid material from a gas mixture on a substrate, under particular conditions. Figure 2.8 shows the principal components of the CVD process. The whole process takes place inside a reactor chamber, under very low atmospheric pressure. Initially, we have the decomposition of the gas mixture, that consists of methane (CH_4) highly diluted in hydrogen (H_2), with the use of hot filaments or lasers [63]. The transferred energy causes fragmentation of molecules into reactive radicals and atoms. This results in the creation of ions and electrons that heat up the gas mixture up to a few thousand kelvins. Then, the gas molecules react with the substrate, with the dissociated H_2, preventing the development of graphitic sp^2 bonds, allowing instead the deposition of sp^3 bonds, that results in diamond growth [61][64].

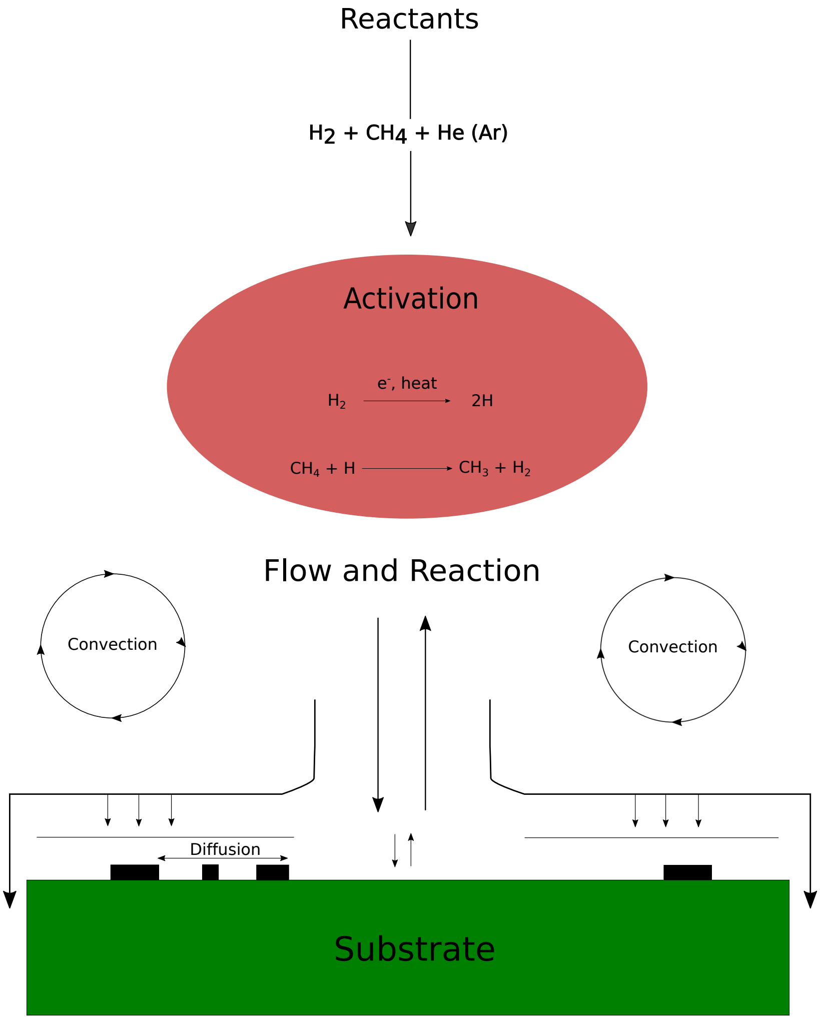

Figure 2.8: Schematic diagram of the CVD process [62].

2.2.3 Ionizing Radiation and CVD Diamond

The behavior of CVD diamond under ionizing radiation, shows similarities with the other semiconductor materials that are used as solid-state detectors, as the mechanism by which the transit of charged particles through the detector is measured is the generation of an electrical signal in an appropriate external circuit [64]. This indirect approach is the basis for modern radiation detectors that use CVD diamond as sensing material and will be the vehicle to describe the physical processes that occur during the exposure to ionizing radiation.

A typical diamond-based radiation detector is fundamentally being constructed by a high resistivity diamond sandwiched between two metal electrodes [65], as shown in Figure 2.9. When a charged photon with energy about three times the bandgap energy [65] passes through the volume of the diamond, it leaves behind a trail of excited and ionized atoms that re-

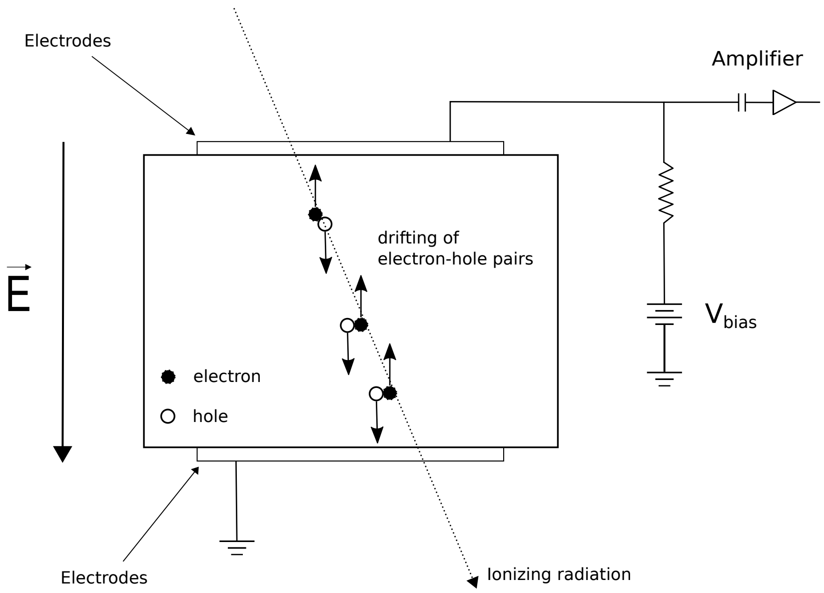

FIGURE 2.9: Schematic diagram of a typical CVD diamond radiation detector.

sult in the production of electron-hole pairs [66]. These electrons and holes are both able to move within the diamond lattice and in the absence of an externally applied electric field they would recombine quickly. However, in the presence of an electric field, the electron-hole pairs are separated between the electrodes and eventually become pinned or trapped within the defects of the material or travel up to the boundaries [66]. The signal on a diamond-based radiation detector is generated in the external circuit, because of the charge movement within the diamond. Tapper [66] gives a quite simple explanation about the charge which flows in the external circuit. More specifically, when one positive (+q) and one negative (-q) charges[2] separate in a distance x in a homogenous electric field E, the total work done for maintaining the electric field by the power source would be

$$W = Eqx \tag{2.2}$$

If we consider as l the width of the gap and V the applied potential, then the electric field would be

$$E = \frac{V}{l} \tag{2.3}$$

and if we combine equations (2.2) and (2.3), we could write the work as

$$W = \frac{Vqx}{l}. \tag{2.4}$$

[2]It should be evident that by positive charge, we refer to holes and by negative charge to electrons.

As Formula 2.4 represents the amount of energy that is transferred to the detector, there should be a relevant electrical current flowing around the external circuit. The time integral of this current would represent the total charge which actually flows and is given by dividing equation (2.4) by voltage, which results in the final equation (2.5) for the total charge that flows within the circuit.

$$Q = \frac{qx}{l} \tag{2.5}$$

For calibrated ionizing radiation detectors (so called dosimeters) it is the correlation of this total charge with the absorbed dose within the sensitive volume, that provides the necessary information about the existence of a dose due to exposure to ionizing radiation to the user. The total charge is proportional to the production of electron-hole pairs from the incident radiation and the presence of defects populations (such as impurities, point defects, dislocations, etc) usually leads to a reduction in conductivity, because they trap or scatter charge carriers [60].

In general, these populations are classified as either shallow or deep, with the classification to depend on the temperature or energy at which they are electrically emptied. In Figure 2.10 there is a very informative example from the literature, illustrating the result of such defects on the temporal response of a CVD diamond. At the beginning of irradiation, there is a progressive increase in the radiation-induced current, because of the charge carriers that are no longer able to fill the traps in the material, as they steadily become more detected. After a certain time, the gradual increase of the induced current slows down, as traps in the diamond volume are filled. The de-trapping of charge in shallow defects in the diamond appear as a tail, after the stop of irradiation until the moment when there is a second irradiation of the diamond. The radiation-induced current reaches saturation more rapidly, as there was no sufficient time for the de-trapping process to complete and empty the deep traps in the diamond's volume.

A CVD diamond shows some important properties that are relevant for a detector material and describe the physical background of diamond as radiation detector. The physical processes that are relevant to the radiation detector technology are the following;

- Charge pair production
- Recombination
- Drift of charge pairs
- Leakage current

The **charge pair production** process in a CVD diamond shows the same behaviour as in other semiconductor materials. Diamond requires

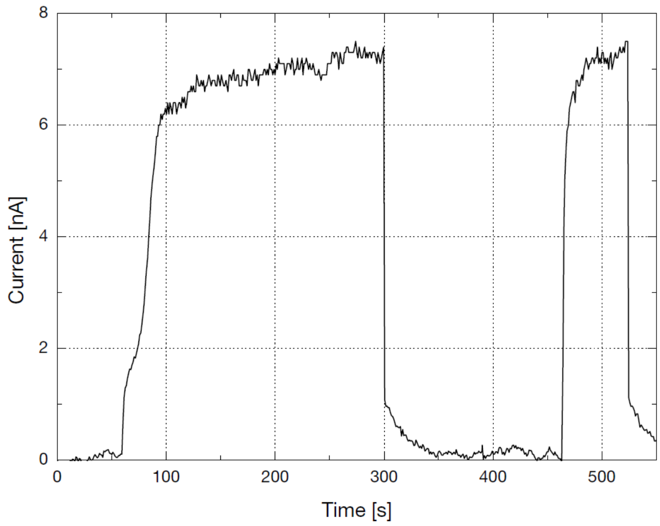

FIGURE 2.10: Example of priming effects in a CVD diamond radiation detector under X-ray irradiation in clinical conditions (from Ref. [67]). Priming effect is defined as the process of filling the diamond lattice traps with charged carriers and it is correlated with material quality.

higher energy to create electron-hole pairs (see Table 2.2) than silicon. This results in the production of fewer charge pairs for the same amount of deposited energy. Furthermore, the physical phenomenon of **recombination** occurs through two processes, with its lifetime to depend primarily on the level of impurities of the material. Impurities and defects in the crystal lattice of a CVD diamond create intermediate energy levels within the forbidden region of energy (band gap) that expedite the recombination of charge pairs, so called *extrinsic recombination*. In addition to this, the usual direct recombination of an electron that falls from the conduction to the valence band takes also place, the so called *intrinsic recombination*. The expected lifetime for both recombination processes depends on the quality of the material and according to Table 2.3 varies from a few ns to about 1 s.

Recombination Process	Lifetime
Intrinsic	few μs to 1 s
Extrinsic	0.1 - 10 ns

Table 2.3: Charge-carrier lifetime ranges for the characteristic recombination processes in CVD diamond [6].

In general, the effective charge-carrier lifetime depends on the recombination lifetime of all volumetric recombination processes that occur both in the bulk and at the surface of the considered material. Equation (2.6) describes the lifetime of the carriers

$$\frac{1}{\tau_{eff}} = \frac{1}{\tau_{int}} + \frac{1}{\tau_{ext}} + \frac{1}{\tau_s}, \tag{2.6}$$

where τ_{int} is the lifetime of intrinsic recombination, τ_{ext} the extrinsic lifetime and τ_s the carrier lifetime due to surface recombination [68]. As surface recombination could be considered as insignificant for semiconductor applications, it is apparent that the effective lifetime of a CVD diamond is dominated by the extrinsic lifetime process [6][69].

In the Appendix, Figure 6 describes the three dominant interaction mechanisms that are probable to take place, during interaction between photons and matter. For diamond, the photoelectric effect dominates for energies below 30 keV, while in the energy range from 30 keV to 20 MeV the Compton effect is prepotent, with pair production to be the dominant effect for energies greater than 20 MeV [64].

2.3 Surface Acoustic Waves

The first demonstration of surface acoustic waves was by Lord Rayleigh in his 1885 publication, describing the behaviour of seismic waves in an isotropic material after a ground shock [70]. His work became the stepping stone in the investigation of acoustic waves by other researchers, introducing experimental methods in the fields of seismology, non-destructive evaluation of materials and radars [71]. In 1965, R. M. White and F. W. Voltmer demonstrated the generation of surface acoustic waves through the fabrication of an interdigital transducer (IDT) on a quartz (SiO_2) crystal substrate [72]. This combination (Figure 2.18) of an IDT on a piezoelectric substrate proved to be a technological milestone that laid the foundation for the fabrication and application of SAW devices in modern electronics [73].

The low acoustic losses, together with the high Q-values and the remarkable versatility made SAW-devices indispensable components in almost every industrial and commercial electronic product [71]. Mobile phones, mechanical sensors, biosensors and environmental sensors cover the most traditional usage of SAWs [74].

2.3.1 Propagation of Acoustic Waves in Solids

In order to describe the propagation of acoustic waves in solids, we will first consider an isotropic, homogeneous and perfectly elastic material with density ρ. To simplify the approach, it is assumed that there are no external forces acting on the material, as well as no free charges and that it shows

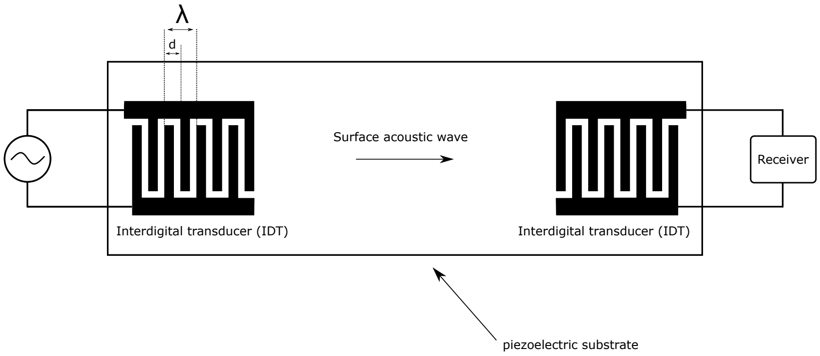

FIGURE 2.11: Sketch of the first IDT application on piezoelectric substrate (from Ref. [72]).

no piezoelectricity. The displacements will be expressed in terms of strain (S) while the forces in terms of stress (T).

Suppose that an infinitesimal volume element of the material is located, in the equilibrium state, at the point $\mathbf{x} = (x_1, x_2, x_3)$. If this volume has a displacement from its equilibrium state by a distance $\mathbf{u} = (u_1, u_2, u_3)$ to a new position $\mathbf{x}'$, then we have the following correlation $\mathbf{x}' \rightarrow \mathbf{x} + \mathbf{u}$. Assuming that the displacement $\mathbf{u}$ is time-independent and there are no internal forces, the strain at each point is defined by

$$S_{ij}(x_1, x_2, x_3) = \frac{1}{2}(\frac{\partial u_i}{\partial x_j} + \frac{\partial u_j}{\partial x_i}), \quad i, j = 1, 2, 3 \tag{2.7}$$

where S_{ij} is a symmetrical second-rank tensor, therefor $S_{ij} = S_{ji}$ [75].

In order to describe the internal forces, we will consider one infinitesimal volume element of the material in Cartesian coordinates as in Figure 2.12. As the material is elastic, any deformation that occurs due to applied forces will be reversible after the release of the force. The statement by Hook's Law that for relatively small deformations of an object the displacement is proportional to the deforming force, could be generalised and one can state that in one-dimensional case stress is proportional to strain [76]. This correlation is described by

$$T_{ij} = \sum_k \sum_l c_{ijkl} S_{kl}, \quad i, j, k, l = 1, 2, 3 \tag{2.8}$$

where c_{ijkl} is defined as stiffness tensor which is also symmetric [75].

Assuming that stress and strain are functions of time and position, it is derived that the motion of the material is subject to the Laws of Newton, thus it could be combined with equations (2.7) and (2.8) to obtain the equation of motion. It can be proved [75] that for all points $\mathbf{x}'$ the equation of motion is defined by

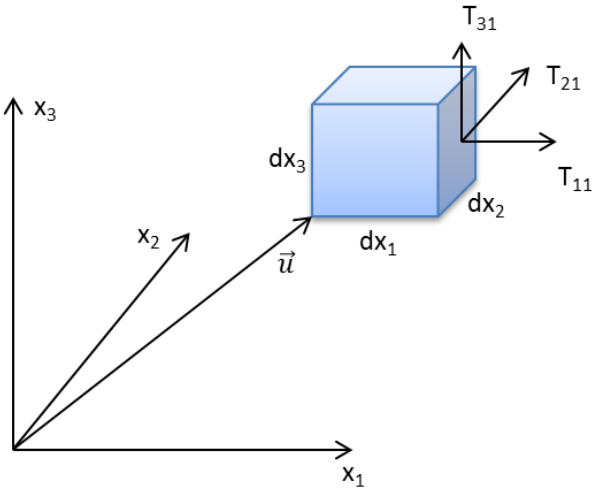

Figure 2.12: Infinitesimal volume element with example of applied forces [77].

$$\rho \frac{\partial^2 u_i}{\partial t^2} = \sum_j \frac{\partial T_{ij}}{\partial x_j}, \quad i, j, k = 1, 2, 3. \tag{2.9}$$

For piezoelectric materials, the elastic stresses and strains are coupled to electric fields and displacements [75]. These materials show piezoelectricity because of their anisotropy and lack in symmetry that derive from their internal crystal structure. In addition to the strain components S_{ij}, the stress components T_{ij} depend on the electric field $\mathbf{E}$ with the relation as follows

$$T_{ij} = \sum_k \sum_l c^E_{ijkl} S_{kl} - \sum_k e_{kij} E_k, \tag{2.10}$$

with the tensor c^E_{ijkl} to correspond as stiffness tensor for a constant electric field.

Similarly, there is the dependence of the electric displacement $\mathbf{D}$ with the electric field $\mathbf{E}$ as follows

$$D_i = \sum_j \epsilon^S_{ij} E_j + \sum_j \sum_k e_{ijk} S_{jk}, \tag{2.11}$$

where ϵ^S_{ij} is the tensor of permittivity for constant strain.

In equations (2.10) and (2.11), the tensor e_{ijk} is called the piezoelectric tensor. It relates elastic to electric fields and its symmetry derives from the expression of the stress component tensor T_{ij} [75].

The propagation of elastic waves in a piezoelectric material are described by Maxwell's equations [77]. As equation (2.8) is applied for piezoelectric materials, we could express this in terms of the displacements u_i and the electric potential Φ [75]. As the propagation velocity of elastic disturbances is many orders of magnitude smaller than the electromagnetic ones [78], the electric field that derives from Maxwell's theory can be expressed using a quasi-static approximation, where the electrical variables are dominated by electrostatics, as follows

$$E_i = -\frac{\partial \Phi}{\partial x_i}. \tag{2.12}$$

The equation of motion after the combination of equation (2.12) with equations (2.10) and (2.7) becomes

$$\rho \frac{\partial^2 u_i}{\partial t^2} = \sum_j \sum_k \left\{ e_{kij} \frac{\partial^2 \Phi}{\partial x_j \partial x_k} + \sum_l c^E_{ijkl} \frac{\partial^2 u_k}{\partial x_j \partial x_l} \right\} \quad [75]. \tag{2.13}$$

As our material is considered to be an insulator, there will be no free charges. Thus, the differential form of Gauss's law as the divergence of the displacement **D** will give $\nabla \cdot \mathbf{D} = 0$ [79][75]. Combining with equation (2.11) we conclude to the following;

$$\sum_i \sum_j \left\{ \epsilon^S_{ij} \frac{\partial^2 \Phi}{\partial x_i \partial x_j} - \sum_k e_{ijk} \frac{\partial^2 u_j}{\partial x_i \partial x_k} \right\} = 0 \quad [75]. \tag{2.14}$$

The system of equations (2.13) and (2.14) give the relations for the three mechanical displacements u_i and the electric potential Φ. If we specify the z-axis ($x_3 = z$) as propagation direction of the displacement, then it derives that the displacement in the x- and y-axis, ($x_1 = x$) and ($x_2 = y$) respectively, will be constant.

Taking this into consideration, the system of equations (2.13) and (2.14) will be transformed as follows;

$$\rho \frac{\partial^2 u_z}{\partial t^2} - e_{z3} \frac{\partial^2 \Phi}{\partial z^2} - c_{33} \frac{\partial^2 u_z}{\partial z^2} = 0 \tag{2.15}$$

$$e_{x3} \frac{\partial^2 u_z}{\partial z^2} - \epsilon_{zz} \frac{\partial^2 \Phi}{\partial z^2} = 0 \tag{2.16}$$

If we eliminate the electric potential Φ, then equation 2.15 will be transformed as

$$\begin{aligned} \rho \frac{\partial^2 u_z}{\partial t^2} &= \frac{e^2_{z3}}{\epsilon_{zz}} \frac{\partial^2 u_z}{\partial z^2} + c_{33} \frac{\partial^2 u_z}{\partial z^2} \Rightarrow \\ \Rightarrow \rho \frac{\partial^2 u_z}{\partial t^2} &= c_{33} \left(1 + \frac{e^2_{z3}}{\epsilon_{zz} c_{33}}\right) \frac{\partial^2 u_z}{\partial z^2} \end{aligned} \tag{2.17}$$

In absence of piezoelectricity the piezoelectric tensor e_{x3} equals to zero. Hence, equation 2.17 is transformed as follows

$$\rho \frac{\partial^2 u_z}{\partial t^2} = c_{33} \frac{\partial^2 u_z}{\partial z^2}. \tag{2.18}$$

Comparing equations 2.17 and 2.18, we could notice that in presence of piezoelectricity the tensor could be written as

$$c_{33}^* = c_{33} \left(1 + \frac{e_{z3}^2}{\epsilon_{zz} c_{33}} \right). \tag{2.19}$$

The factor $\frac{e_{z3}^2}{\epsilon_{zz} c_{33}}$ in the above equation is called electromechanical coupling coefficient K^2 and corresponds to the efficiency of a given piezoelectric material, that is associated with a surface acoustic wave, to convert an applied electrical signal into mechanical energy [80]. The electromechanical coupling coefficient K^2 could also be expressed in terms of the velocity v as

$$K^2 = \frac{2\Delta v}{v} \tag{2.20}$$

where Δv corresponds to the velocity change of an SAW that occurs when the free surface of the piezoelectric material accommodates a highly conducting thin metal film and v is the velocity of the SAW [80][27]. Coupling coefficient and velocity of SAW exemplify the most important material parameters in the field of SAW devices, as they determine the suitability of the selected materials like lithium niobate ($LiNbO_3$), quartz (SiO_2) and lithium tantalate ($LiTaO_3$) in terms of applications [75]. Table 2.4 shows the differences between the values of the above parameters for these materials.

Parameter	Y-Z $LiNbO_3$	128° Y-X $LiNbO_3$	ST-X SiO_2	36° Y-X $LiTaO_3$
velocity (m/s)	3488	3979	3159	4212
K^2 (%)	4.8	5.4	0.12	4.8

Table 2.4: Electromechanical coupling coefficient and velocity values for common surface-wave materials [75].

2.3.2 Rayleigh Waves

The transition from bulk-waves that we have discussed so far to surface acoustic waves, should introduce necessary boundary conditions on equations 2.13 and 2.14. The mechanical boundary defines that the atoms at the surface, experience forces only in the direction of the medium, while the forces that are perpendicular to the surface are zero [81][82]. As there are no forces on the surface, stress tensors will be $T_{13} = T_{23} = T_{33} = 0$ at $x_3 = 0$. In the presence of a piezoelectric material it is also essential to apply an electrical boundary condition at the surface. For the description of this condition, we will consider the following two cases [75][77];

Free-surface case: The space above the surface is considered to be vacuum with zero conductivity, thus without free charges and with wave velocity v_f. Generally, the space above the surface is not absolute vacuum and will have a potential.

Metallized case: It is assumed the surface to be covered with a thin metallic layer with infinite conductivity. The thickness of the layer causes the elimination of the horizontal component of the electric field at the surface, leaving unaffected the mechanical boundary condition. In analogy with the free-surface case, there is a velocity v_m that describes this case.

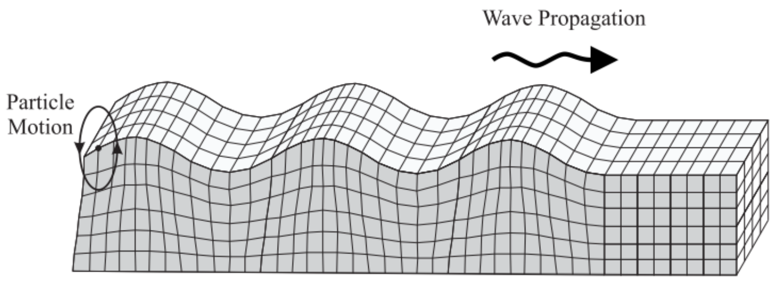

FIGURE 2.13: Schematic representation of a Rayleigh wave (SAW), with the sketch ellipsis to indicate the direction of motion of the individual molecules at the surface of the piezoelectric substrate. The motion of the molecule is counterclockwise [83].

The wave that accompanies theses constraints is commonly known as *Rayleigh-wave* (Figure 2.13). This wave runs on the surface of the material, forcing the particles on elliptical orbits and has approximately the penetration depth of a wavelength. As it was mentioned earlier, in piezoelectric materials every mechanical wave is accompanied by an electrical wave. This fact alters the apparent stiffness of the material as well as the sound velocity, causing different speeds of sound for both electrical boundary conditions. The difference between the velocities at the free-case v_f and metallized-case v_m, is a measure of the coupling between the mechanical and electrical perturbations at the surface and it correlates with the electromechanical coupling coefficient K^2 from equation (2.21) as follows

$$K^2 = 2\frac{\Delta v}{v_f} = 2\frac{v_f - v_m}{v_f}. \tag{2.21}$$

2.3.3 Interaction with Conductive Layers

The interaction between surface acoustic waves and different media has been employed to study various acoustoelectric effects [28]. Physical quantities for the characterization of semiconductors have been obtained by using the configuration shown in Figure 2.14. In this approach the electric component that accompanies the mechanical wave on the piezoelectric material, penetrates and interacts with the semiconductor located above it. More specifically, the semiconductor material (GaAs/AlGaN heterostructure) contains in its structure layer a two-dimensional electron system (2DES) that interacts with the electric component of the mechanical wave.

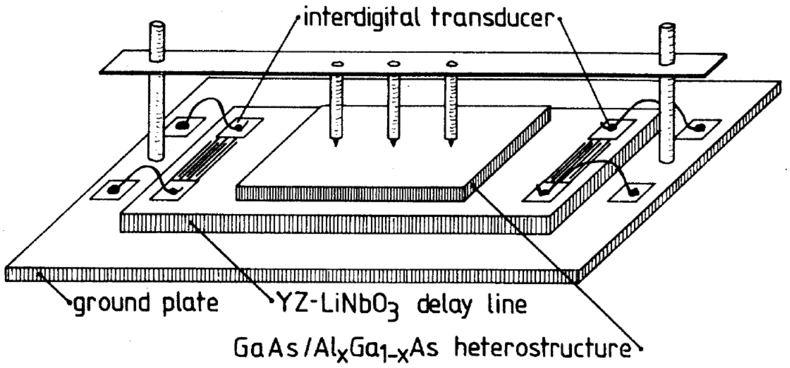

Figure 2.14: Sketch of an early configuration for studying the properties of GaAs-based heterostructures [28].

As the principle of such configuration (Figure 2.14) is the basis of this thesis, an introduction to the theoretical background of this technique is the purpose of this subsection [77][82][84]. Considering the one-dimensional model of an extrinsic semiconductor, the expression for the current density may be written in terms of electric field **E** and electric displacement **D** as follows

$$J = e\left(n_0 + n_1\right)\mu E + qD_n \frac{\partial n_1}{\partial x} \tag{2.22}$$

were q is the electronic charge, n_0 is the charge charrier density in equilibrium, while n_1 is the conductivity modulation and D_n the diffusion constant.

Poisson's equation could be written as

$$\frac{\partial D}{\partial x} = -qn_1 \tag{2.23}$$

and equation of continuity as

$$\frac{\partial J}{\partial x} = q\frac{\partial n_1}{\partial t}. \tag{2.24}$$

After combining equations (2.22), (2.23) and (2.24) we have a relation between electric field **E** and electric displacement **D** as follows

$$\frac{\partial^2 D}{\partial t \partial x} = -n_0 q\mu \frac{\partial E}{\partial x} + \mu \frac{\partial E}{\partial x}\frac{\partial D}{\partial x} + \mu E \frac{\partial^2 D}{\partial x^2} + D_n \frac{\partial^3 D}{\partial x^3}. \tag{2.25}$$

Supposing that the plane wave time and space dependences could be expressed as $E = E_0 + E_1 e^{i(kx-\omega t)}$ and $D = D_0 + D_1 e^{i(kx-\omega t)}$, where constants E_0 and D_0 correspond to the longitude external field [77]. We could substitute these wave expressions to equation (2.25) and by considering that the product of D and E is negligible, as well as that the conductivity modulation is small ($n_1 << n_0$), we have the relation between electric field and electric displacement

$$D_1 = -\frac{inq\mu}{\omega + ik^2 D_n + \mu E_0 k} E_1 \quad [77][84]. \tag{2.26}$$

Combining this equation with (2.10) and (2.11), as well as with (2.15) and (2.16) we can acquire an expression for the complex elastic constant in relation with electric field E

$$c^* = c \cdot \left(1 + K^2 \cdot \frac{\frac{\omega}{\omega_R}\left(1 + \frac{\mu E_0}{v}\right) + i\frac{D_n k^2}{\omega_R}}{\frac{\omega}{\omega_R}\left(1 + \frac{\mu E_0}{v}\right) + i\left(1 + \frac{D_n k^2}{\omega_R}\right)} \right) \tag{2.27}$$

were $\omega_R = \frac{\sigma_{3R}}{\epsilon^*}$ is defined as conductivity frequency [84]. In this expression σ_{3R} corresponds to the average conductivity as $\sigma_{3R} = nq\mu$, while the reciprocal ϵ^* is defined as dielectric relaxation time [84] with the following mathematical expression $\epsilon^* = \epsilon_0 \left(\epsilon_{piezo} + 1\right)$ [82].

From equation (2.27) we can extrapolate the following parameter

$$\gamma = 1 + \frac{\mu E_0}{v} = 1 + \frac{v_d}{v} \tag{2.28}$$

were it is described as electron-drift parameter by velocity v_d under the presence of external field [77]. As it is suggested in [77], if we consider the following wave number expression $k = \omega/v + i\Gamma$ as well as that $\rho\omega^2 = c^* k^2$ and $v_f = \sqrt{c/\rho}$, then we will have the expressions for attenuation and velocity of the surface acoustic wave as follows

$$\frac{\Gamma}{k} = Im\left(\frac{c}{c^*}\right)^{1/2} \tag{2.29}$$

$$\frac{v}{v_f} = Re\left(\frac{c^*}{c}\right)^{1/2} \tag{2.30}$$

From equations (2.31) and (2.32) we could generate the following formulas

$$\frac{\Gamma}{k} = \frac{K^2}{2} \cdot \frac{\frac{\omega_R}{\gamma\omega}}{1 + \left(\frac{\omega_R}{\gamma\omega}\right)\left(1 + \frac{D_n k^2}{\omega_R}\right)^2} \tag{2.31}$$

$$\frac{\Delta v}{v_f} = \frac{K^2}{2} \cdot \frac{1 + \left(\frac{\omega_R}{\gamma\omega}\right)^2 \left(\frac{D_n k^2}{\omega_R}\right)\left(1 + \frac{D_n k^2}{\omega_R}\right)}{1 + \left(\frac{\omega_R}{\gamma\omega}\right)^2 \left(1 + \frac{D_n k^2}{\omega_R}\right)^2} \tag{2.32}$$

The interaction of the electrical component of the SAW with 2DES implies the transfer of energy, impacting the transmission of the SAW in relation with the conductivity of the system [82]. The ratio of wave frequency with conductivity frequency, correlates the conductivity of 2DES with the conductivity for maximum attenuation σ_m as

$$\frac{\omega}{\omega_R} = \frac{\sigma_m}{\sigma} \quad [82]. \tag{2.33}$$

For the above ratio we will distinguish the following three cases [77][27][82]:

$\omega_R >> \omega$: The charge carriers are restructured quite fast and the piezoelectric field will be shielded, meaning that the energy transferred from the SAW to the charge-carriers is small.

$\omega_R << \omega$: The high frequency results in the absence of charge-carrier diffusion.

$\omega_R \approx \omega$: The resonance implies in maximum transfer of energy from the SAW to the charge-carriers, thus maximum wave attenuation.

From the above considerations of the simple relaxation model and the attenuation due to Joule losses [85], we can express the attenuation coefficient Γ and the velocity shift of SAW, as non-monotonic functions of conductivity σ

$$\Gamma = \frac{K^2}{2} k \frac{\frac{\sigma}{\gamma\sigma_m}}{1 + \left(\frac{\sigma}{\gamma\sigma_m}\right)^2} \tag{2.34}$$

$$\frac{\Delta v}{v_f} = \frac{K^2}{2} \frac{1}{1 + \left(\frac{\sigma}{\gamma\sigma_m}\right)^2} \tag{2.35}$$

In absence of an external electric field the drift parameter γ will equal to one. There are examples in the literature of the conductivity dependence of the attenuation coefficient Γ, as well as of the velocity shift of SAW from the research field of graphene and gallium arsenide (GaAs) [77][27][82][85].

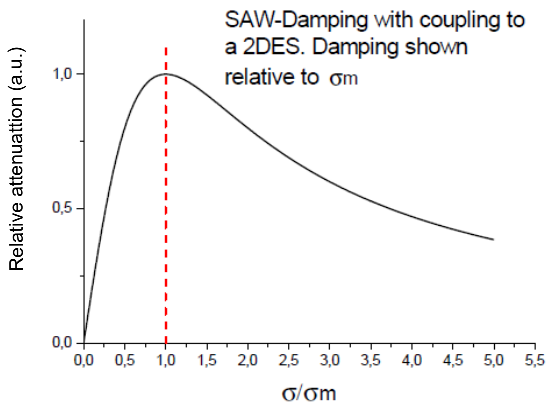

FIGURE 2.15: Example of relative attenuation of SAW in terms of conductivity change of 2DES (from Ref. [82]).

From Figures 2.15 and 2.16 we can extract that the attenuation of a SAW rapidly increases with layer's conductivity σ until it reaches a maximum when $\sigma = \sigma_m$, while beyond the attenuation shows a rapid decrease. Similar behaviour shows the velocity shift, caused by the modulation of the conductivity of the layer.

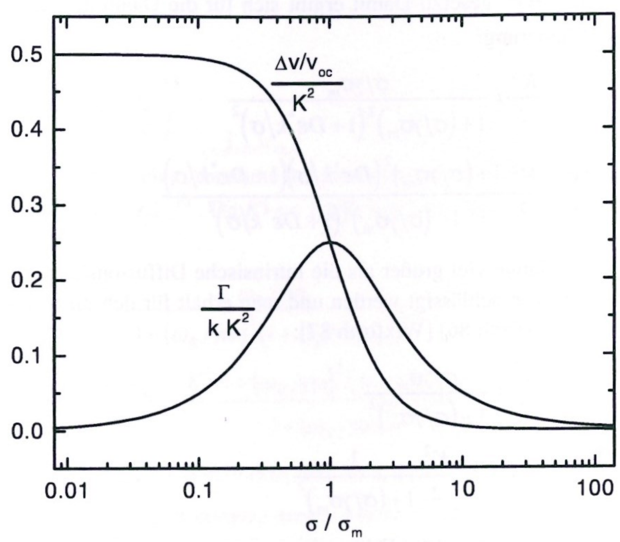

FIGURE 2.16: Example of relative attenuation and velocity shift of SAW in terms of conductivity change of 2DES (from Ref. [77]).

2.3.4 Stimulation and Detection

Those acoustic waves that propagate along the surface of a piezoelectric substrate could have a broad range of propagation frequencies from several MHz to GHz [80]. As it was mentioned in the beginning of this section, these acoustic waves are stimulated by IDTs where their function is to convert the electrical energy into mechanical energy and vice versa. Figure 2.17 shows the first published suggestion for IDT application from R. M. White and F. W. Voltmer.

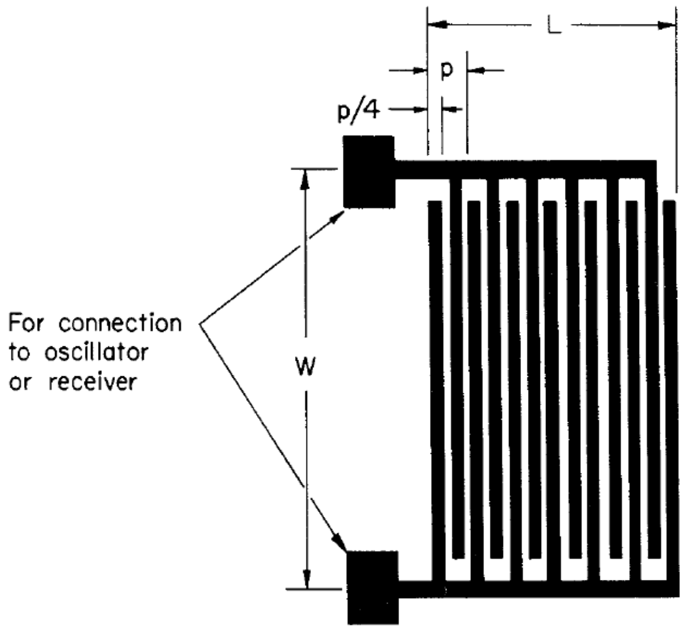

Figure 2.17: The first published sketch of an IDT for stimulation and detection of Rayleigh-waves (from Ref. [72]).

The application of an AC voltage $V(t) = V_0 e^{i\omega t}$ across the electrodes causes the creation of dynamic strains in the substrate, which results in the launch of elastic waves (Rayleigh waves) that run perpendicular to the electrodes with wave velocity v_R [81]. The finger pairs of IDT induce the stress wave that travels along the surface of the substrate in both directions. In order to make sure the in-phase stress and constructive interference, the distance d between two consecutive fingers (Figure 2.18) should be equal to half the wavelength λ_R from which we have $d = \lambda_R/2$.

The propagated wave that is produced from the electrode-fingers of the first IDT, is associated to a frequency known as synchronous frequency f_0, according to $f_0 = v_R/\lambda_R$, where the transducer converts electrical to acoustical energy with maximum efficiency [81]. Even though that there can be many different designs of SAW devices, Figure 2.18 shows the simplest SAW device called as delay-line. The IDT that is connected to the AC

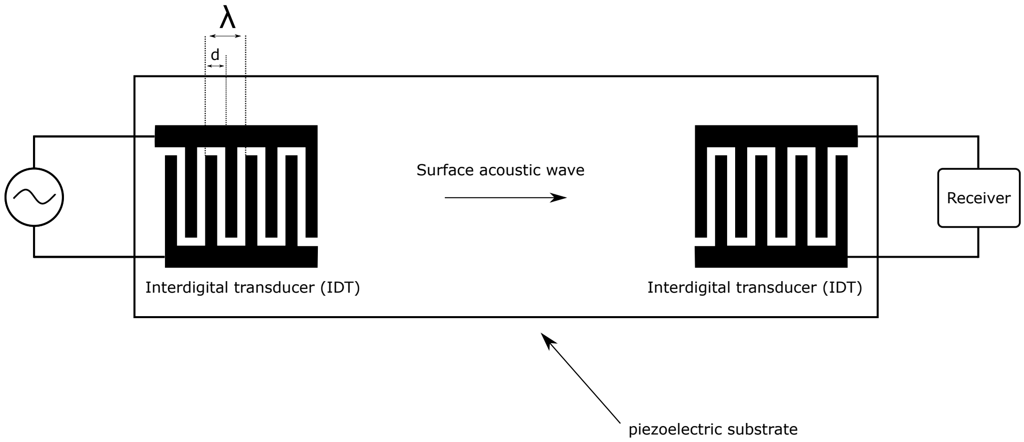

FIGURE 2.18: Schematic of a SAW device with built-in identical IDTs, as well as input and output overview (top-view perspective). The device is called delay-line, because of the propagation velocity difference between the electrical and mechanical component of the surface acoustic wave by a factor of 10^5 [86].

electrical source, creates an electric field in the substrate that generates through piezoelectric effect a wave that propagates along the surface of the substrate. When the propagated wave reaches the receiving transducer it converts to an electrical signal. The propagated SAW reaches the receiving transducer after time $\Delta t = W/v_R$, where W is the aperture of the IDT shown in Figure 2.19.

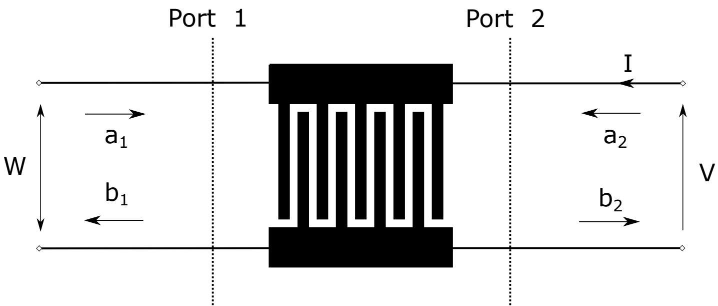

FIGURE 2.19: Interdigital transducer with the used parameters. The variables a_1 and a_2 represent the incident waves to Ports 1 and 2 respectively. Similarly, the variables b_1 and b_2 represent the reflected waves. V corresponds to the applied AC voltage across the electrodes, I to the generated circuit current and W is the aperture of the IDT.

The output of surface acoustic devices can be sampled using specialised equipment like a frequency counter, voltage meter or network analyser. Network analysers offer the benefit of sweeping across the range of oscillation frequencies. In modern times, this is the most common solution for SAW detection and the one that also was used through-out this work. Such devices measure the characteristic admittance Y or impedance Z of the device under testing, detailing frequency shifts from resonance, as well as changes in the quality factor Q.

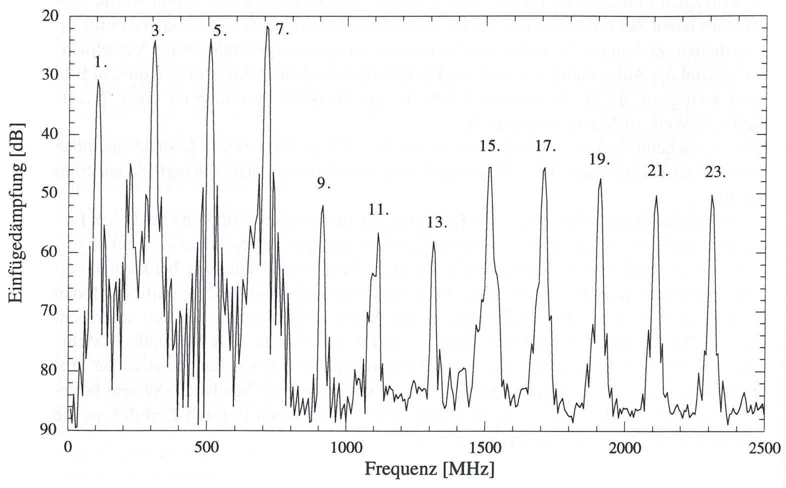

Figure 2.20: Example of transmission response from spectrum analyser for Split-4 IDTs on $LiNbO_3$ substrate (from Ref. [87]).

A theoretical description of the frequency response for IDTs could be provided through the delta impulse model [87]. According to this model, every electrode of the transducer is considered to excite surface acoustic waves as delta function excitation centre. The frequency response $H(f)$ for a specific point outside of the transducer is given by the following equation:

$$H(f) = \sum_{n=1}^{N} (-1)^n \cdot a_n \cdot e^{-2\pi i f t_n} \tag{2.36}$$

where a_n is defined as the weighting factor of an individual IDT electrode and t_n is labelled as the delay between successive gaps between the fingers of IDTs, while the factor $(-1)^n$ defines the polarisation of electrodes. Considering that a_n is identical for every unweighted electrode we obtain the following equation:

$$|H(f)| = N \cdot \frac{sinF}{F} \tag{2.37}$$

with $F \propto f - f_0$, where f_0 corresponds to the characteristic resonant frequency of the transducer. Figure 2.20 describes Equation (2.38) in terms of an IDT's frequency response, with the bandwidth of the latter to be referred as

$$\frac{\Delta f}{f_0} = \frac{1}{N}. \tag{2.38}$$

IDTs can have different geometries in order to reduce the undesired effects of finger reflection and cancel out at centre frequency, avoiding the summation as for single IDT [80]. Figure 2.21 shows three designs of interdigital transducers that are used to achieve different characteristics in terms of centre frequency, capacitance or impedance [88].

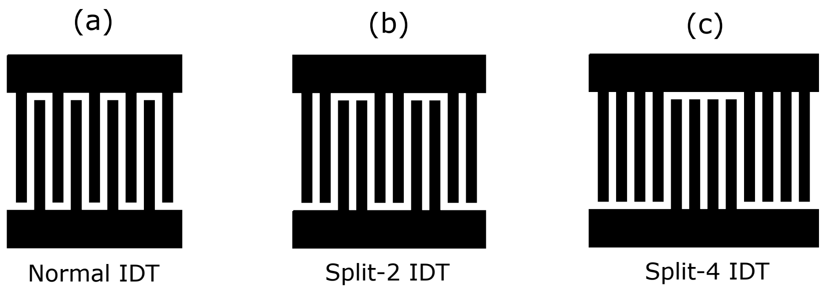

FIGURE 2.21: Example of different IDT SAW designs; (a) Single conventional IDT, (b) Split-2 IDT and (c) Split-4 IDT.

The main disadvantage of split-IDTs is the increased complexity in the photolithography process, as it requires much more complicated photomask patterns to fabricate the electrodes. Moreover, the effective electromechanical coupling coefficient K^2 differs among the design patterns, as well as the capacitance C_T of a split-design, that is almost 1.4 times larger than that of a normal IDT [80].

2.3.5 Fabrication of Surface Acoustic Wave Devices

The fabrication sequence for surface acoustic wave devices follows the basic steps of optical photolithography, where the ultra-violet (UV) illumination of a photoresist-coated sample with the use of a photomask structures the photoresist layer according to the pattern of the photomask [31]. The photoresist could be negative or positive, with the type to determine its reaction to the UV illumination. In case of a negative photoresist, UV illumination initiates a polymerization process which makes the exposed areas more difficult to wash away during the step of development. In contrast, the illumination of exposed areas that are covered with a positive photoresist makes them less difficult to be washed away [89]. The two types of photoresists are used in accordance with the following photolithography procedure, because negative photoresists are mainly used for Physical Vapor Deposition (PVD) due to the optimal behaviour during lift-off after deposition, while positive photoresists are more preferred for etching [31][89].

Figure 2.22 shows schematically the fabrication steps for a SAW delay-line, with the use of PVD and lift-off technique. In the beginning the piezoelectric substrate should be cleaned with technical laboratory chemicals like acetone and isopropanol, in order to remove any contamination

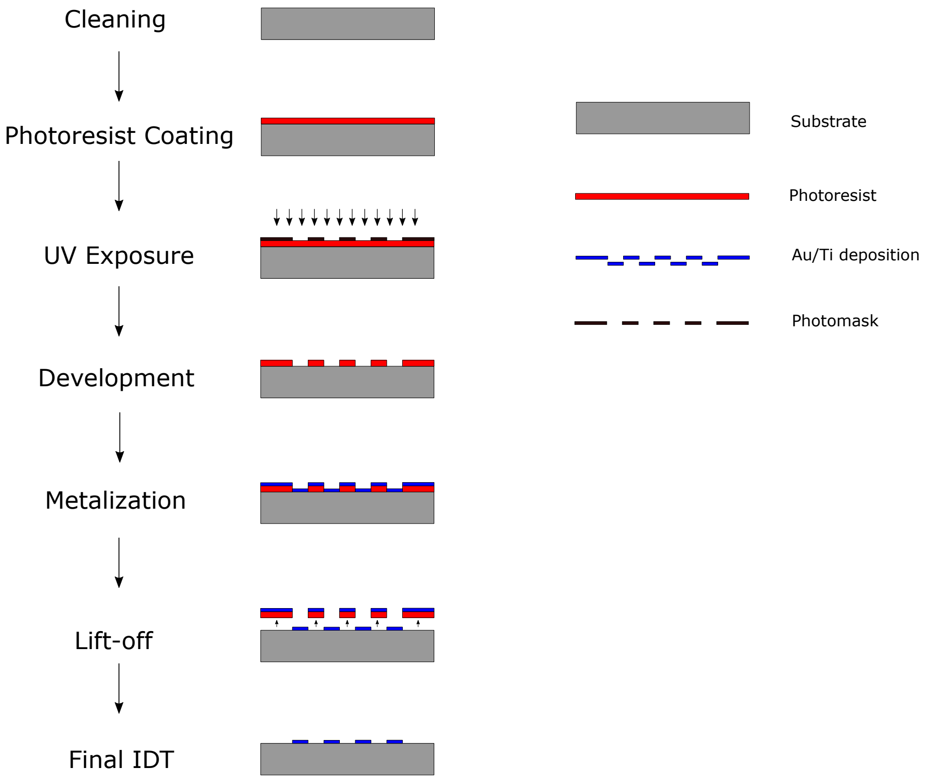

Figure 2.22: Schematic overview of the working principle to fabricate a surface acoustic wave device.

from the surface [90][91]. Afterwards, the negative photoresist is coated to the surface of the substrate and the illumination of the substrate with the photomask in contact takes place. Following the development of the illuminated structure, the metalization takes place. At this step an appropriate metal layer or several layers are deposited with the use of the PVD technique, followed by the stripping of the photoresist to produce the planned IDT structure of the device [91].

After the final step, there are many delay-lines fabricated on the piezoelectric substrate / wafer, thus it is necessary to dice the wafer and extract single devices for quality control and characterization [91]. The characterization of the device in terms of frequency response is measured using a Network Analyzer that acquires a similar response like that shown in Figure 2.20.

2.3.6 Behaviour in a Radiation Environment

Radiation effects on electronic components are major challenge for further advancement of space mission technology. Displacement damage effects, gain degradation, threshold shifts or burnout of transistors, are few examples of possible effects that could occur because of radiation exposure [92].

Effects of interaction of surface acoustic waves with ionizing radiation were first published in 1973 by N. Berg and J. Speulstra [26]. In their work, it is concluded that $LiNbO_3$-based surface acoustic wave devices are radiation hard structures for high-intensity x-ray beams with dose-rates above 10^9 Gy/sec. Later researchers have investigated under extreme ionizing radiation exposure the operation of different types of SAW devices with very high quality factor Q and narrow bandwidth [92].

It was suggested that ionizing radiation does not cause any severe physical damage. In addition, it was noticed that for devices made from non-swept quartz, drastic frequency shifts occur under gamma and proton radiation as shown in Figures 2.23, 2.24 and 2.25. As a radiation beam penetrates into a quartz substrate, causes displacement of atoms and ionization damage of the surface. The radiation-induced damage to the substrate changes the physical properties of the surface and, thus, the properties of the propagating surface acoustic wave. For this reason, there is a shift in the frequency and it was suggested that the following mathematical expression (Equation 2.39) can describe the observed frequency shift;

$$\Delta F_{average} = Ae^{B\Phi}(1 - Ce^{-D\Phi}) \tag{2.39}$$

were A, B, C and D correspond to fitting parameters according to the type of resonator and radiation beam, while Φ corresponds to the total accumulated dose [92][93].

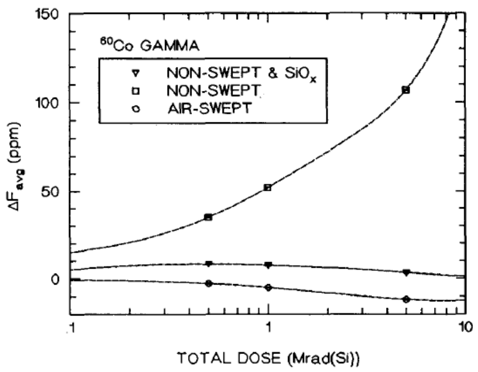

FIGURE 2.23: Example of average frequency shift as a function of total dose due to exposure to gamma radiation from a Cobalt-60 source (from Ref. [93]).

Similar investigations, in terms of frequency shifts from the resonant frequency, have been done under fast neutron and gamma ray exposures for thermosensitive quartz crystal resonators [92][94]. As presented in Figure 2.26a there is an influence of gamma radiation on response frequency until a certain point where the frequency starts becoming constant. Lower doses result in an increase in response frequency; this could be explained

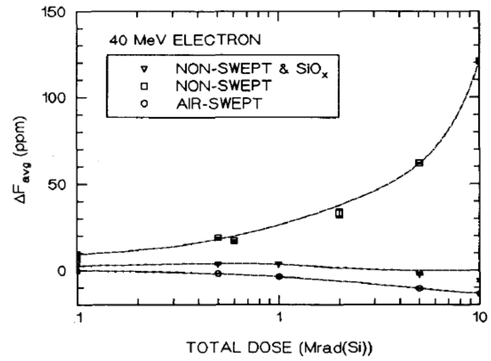

Figure 2.24: Example of average frequency shift as a function of total dose due to exposure to a 40 MeV electron beam (from Ref. [93]).

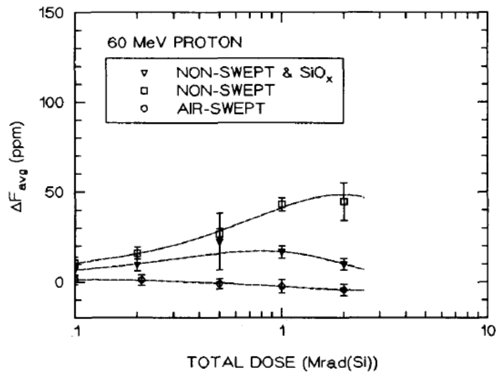

Figure 2.25: Example of average frequency shift as a function of total dose due to exposure to a 60 MeV proton beam (from Ref. [93]).

by the radiation-induced effects on the measurement setup rather than on the substrate [92]. A similar conclusion has been drawn from the investigation with fast neutrons (Figure 2.26b) in terms of a temperature-induced instability of the measurement setup rather than a radiation-induced effect on the SAW device [92][94].

The most recent investigation of ionizing radiation effects on quartz SAW devices by A. Ternawly [92], did not show any significant effects of gamma and neutron radiation exposure even for extremely high doses, confirming the very small frequency shifts that have been reported by other researchers. These slight changes suggest some changes in the environment backdrops due to radiation exposure, thus allowing the fundamental claim that SAW devices are radiation-hard and unaffected by ionizing radiation.

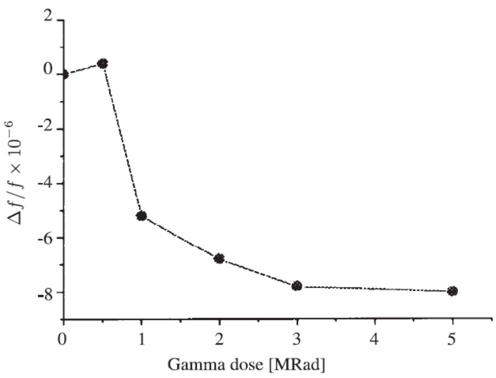

(a) Influence of gamma irradiation.

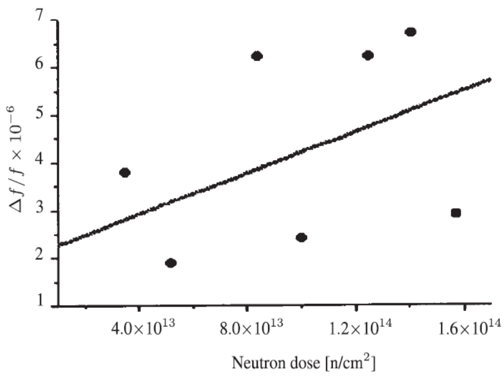

(b) Influence of fast neutron irradiation at room temperature.

FIGURE 2.26: Example of average frequency shift under different radiation beams for the same substrate (from Ref. [94]).

2.3.7 Examples of SAW-based Sensors

The broad applications of SAW-based devices throughout industry or research include many examples of different IDT designs and materials as substrates. Typical operational frequencies for sensing applications are within the range of 10 - 500 MHz and combined with the proper piezoelectric substrate result in the desired sensing device [73]. One of the most common applications for SAW-based devices is chemical sensing which allows the detection of biochemicals, organic and inorganic vapors, as well as explosives [73].

SAW-based sensors consist of a sensing layer on a piezoelectric substrate that is designed to change its physical properties once exposed to the chemical of interest, plus the interdigital transducers for triggering and read out the surface acoustic wave. The most common configurations for chemical sensing applications are sketched in Figure 2.27. In both cases, a surface acoustic wave is produced at the input IDT and as it propagates through the sensing layer, it interacts with the absorbed molecules of the layer, thus resulting in a perturbation of SAW's properties which is expressed as frequency shift that is detected at the readout IDT [95]. In order to further increase the sensitivity of a delay-line, it is common to fabricate a resonator IDT (as in the bottom configuration in Figure 2.27) acting as a reflector, to set up a resonant cavity [73].

As we have already mentioned, the propagation speed v for surface acoustic waves is the speed of sound. This speed can change according to the properties of the sensing layer, resulting in a proportional shift for both the resonant frequency f and phase ϕ of the wave, according to the following expression;

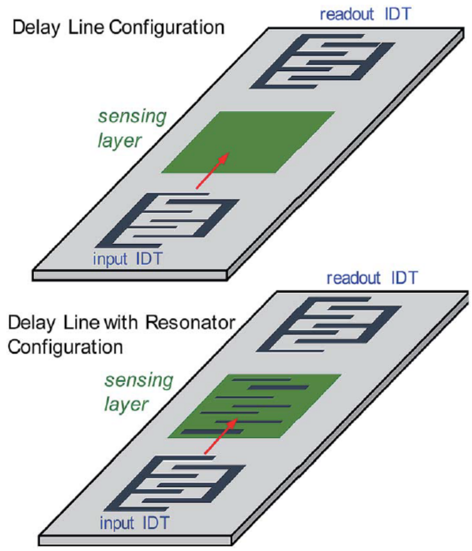

Figure 2.27: Common delay-line configurations using a pair of IDTs for sensing applications (from Ref. [73]).

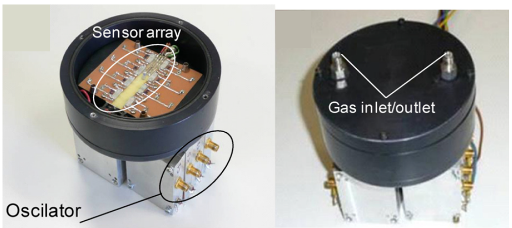

(a) View of sensor array, as well as the major components of the proposed sensor.

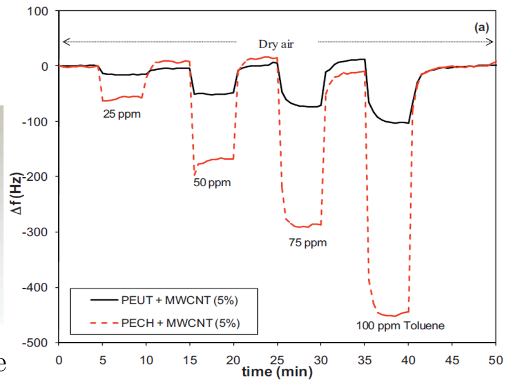

(b) Response of the sensor to different concentrations of polyepichlorohydrin (PECH) and polyetherurethane (PEUT).

Figure 2.28: Example and response of an SAW-based gas sensor (from Ref. [95]).

$$\frac{\Delta v}{v} = \frac{\Delta f}{f} = \frac{\Delta \phi}{\phi} \tag{2.40}$$

An example of an SAW-based sensor is presented in Figure 2.28a from Ref. [95], for gas-phased targets with polymer-based sensing layer on SiO_2 substrate.

Apart from the conventional fabrications of rigid SAW-based devices, there are examples of flexible delay-lines on proper substrates as shown in Figure 2.29. Such devices find applications as components of wearable sensor technology, due to their small size and flexibility.

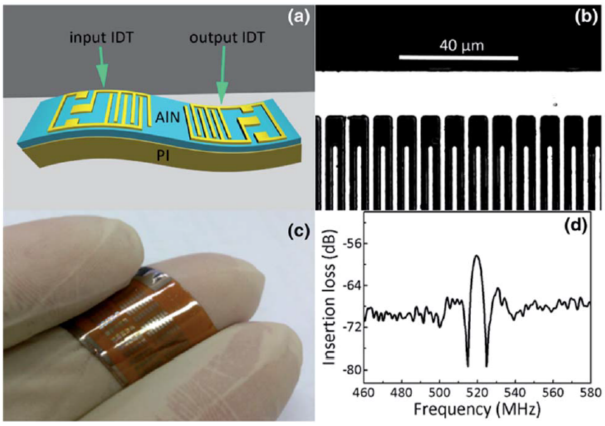

FIGURE 2.29: (a) Three-dimensional model of a flexible delay-line device of aluminum nitride (AlN) films on polyimide (PI) substrate, combined with (b) microscope image of IDT fingers, as well as (c) demonstration of the flexibility of the device with (d) the frequency response of the flexible SAW delay-line (from Ref. [96]).

Even though it was concluded in Ref. [96] that such a material combination shows relatively high insertion loss, it demonstrates the potential of SAW-based devices and the broad spectrum of possibilities for technological applications. SAW-based devices for radiation detection is not as common as with other sensing applications. Consequently, this work expects to add more value into the field of radiation detection with such devices. Suggested solutions were presented from Sandia National Laboratories, USA, in the form of passive radiation sensor that could be operated wirelessly [21]. The published patent generally describes a delay-line on a piezoelectric substrate including a radiation-sensitive material that could be comprised of a metal-halide-containing polymer film as shown in Figure 2.30.

Even though that this progress is a step forward towards radiation detectors of very small size, it is believed that the present work gives a more effective approach.

2.4 Radiation Monitoring in Medicine

The extensive application of ionizing radiation related techniques in the field of medical diagnostics and treatment has increased the necessity for radiation detection systems that allow quantification of the used radiation beam, providing information to the end-user according to the specific applications, such as imaging and dosimetry [97]. The plethora of radiation

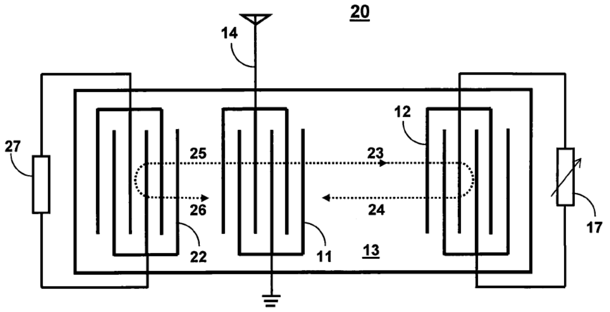

Figure 2.30: Sketch of patented SAW-based radiation sensor (from Ref. [21]). The projected numbers correspond to the detailed description of the invention as it is written on the official documents.

detectors available for personal dosimetry purposes, as the main scope of this work, includes common solutions like thermo-luminescence dosimeters (TLD), film dosimeters, radiophotoluminescent glass dosimeters (RPLGD), optically stimulated luminescence (OSL) dosimeters, electronic personal dosimeters and pen/pocket dosimeters [5]. Excluding the electronic personal dosimeter, all other types of dosimeters require the readout of the dose using specialized equipment by an Official Personal Monitoring Service in a country. Examples of the dosimeters that are operated by Official Personal Monitoring Services in Germany, such as AWST[3]/formerly belonging to Helmholtz Zentrum München, can be found in Figure 2.31.

The necessity for shipment to a centralized processor for analysis of accumulated doses, does not allow real-time monitoring of radiation exposure, thus impacting on the applicability during the operation with ionizing radiation. Even though that electronic personal dosimeters may allow for real-time monitoring, by providing to the user a direct reading of the dose and the dose-rate, they lack operational stability. For example it was reported that they show underestimation or overestimation of accumulated occupational doses. However, for occupational dosimetry with PET radiooisotope and patients, such active dosimeters showed a better performance than passive dosimeters [98]. Furthermore, some electronic personal dosimeters were reported to be sensitive to high-frequency electromagnetic fields, as well as to have slow response time [99]. In 1996 another type of electronic personal dosimeter was introduced, based on the direct ion storage principle, using a floating-gate MOSFET transistor as sensing element [100]. The resistance of the MOSFET transistor is measured through the adjacent charge of the floating gate, providing information on the absorbed dose by a digital voltmeter [101]. Such devices have been reported to be operated by medical personnel to actively monitor radiation exposure during common procedures like e.g. transesophageal echocardiography [102],

[3] Auswertungsstelle

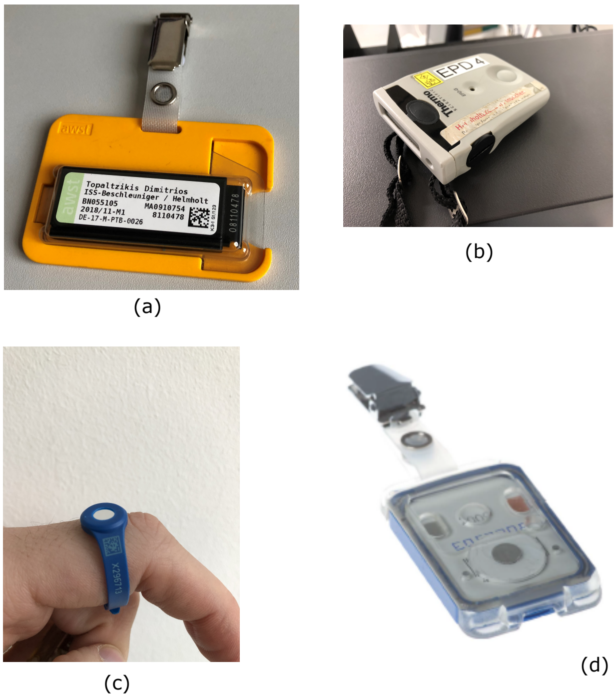

FIGURE 2.31: Examples of personal dosimeters used by the former Official Personal Monitoring Service at the Helmholtz Zentrum München, where this study was mainly conduced.

while at some hospitals direct ion storage (DIS) dosimeters have replaced TLDs as personal dosimetry solution [103]. Newest versions of DIS dosimeters offer wireless transmission of the measured dose using a Bluetooth Low Energy (BLE) communication protocol, thus increasing the capabilities for radiation monitoring of medical personnel [104].

Moreover, in the field of non-personal dosimetry in clinical environments, devices that are commonly used include gas detectors, such as Geiger-Müller counters, proportional counters and ionization chambers, as well as solid-state detectors, such as scintillator counters and semiconductor detectors [15][5]. These devices are mainly used for area dosimetry monitoring during radiotherapy procedures, monitoring the surrounding area of the radiotherapeutic facility. In the group of semiconductor detectors, apart from the commonly used solid materials, germanium and silicon, natural or synthetic diamonds have been introduced for radiation-monitoring applications within medical facilities [19][10], receiving the attention due to their physical characteristics explained in previous sections.

Materials and Methods 3

This chapter provides insights into the working principles of different techniques, experimental details, as well as the specifications of the materials that were used in this thesis. These insights, correspond to the following investigated approaches; a) an AlGaN/GaN high electron mobility transistor (HEMT) based system, and b) a hybrid-device consisting of a synthetic thin film diamond layer and a piezoelectric lithium niobate ($LiNbO_3$) surface acoustic wave (SAW) delay line.

3.1 Materials

3.1.1 Wafer

The two wafers that were used in this study, were fabricated at the Ferdinand-Braun-Institut (FBH) in Berlin, Germany, by growing single thin film layers of AlGaN/GaN HEMT on <0001> oriented sapphire (Al_2O_3). In more detail, on top of a $430\mu m$ c-plane Al_2O_3 substrate, the following layer stack was grown after mutual collaboration with the local scientific personnel: 50 nm AlN as nucleation layer, 3000 nm carbon-compensated (C:GaN) as buffer layer, 60 nm GaN as channel layer, 25 nm AlGaN as barrier and approximately 3 nm GaN as capping (cap) layer. Figure 3.1 shows a schematic sketch of the wafer structure, including the stoichiometric details about the consisting layers.

The 2DEG is located between the barrier and channel layer, with a sheet carrier concentration of $n_{2DEG} \approx 9 \times 10^{12}\ cm^{-2}$ and a mobility of $\mu \approx 1644 cm^2/Vs$, as it was measured after fabrication, at room temperature and 360 mT atmospheric pressure. Moreover, the produced wafers were examined in terms of sheet resistance distribution, as shown in Figure 3.2,

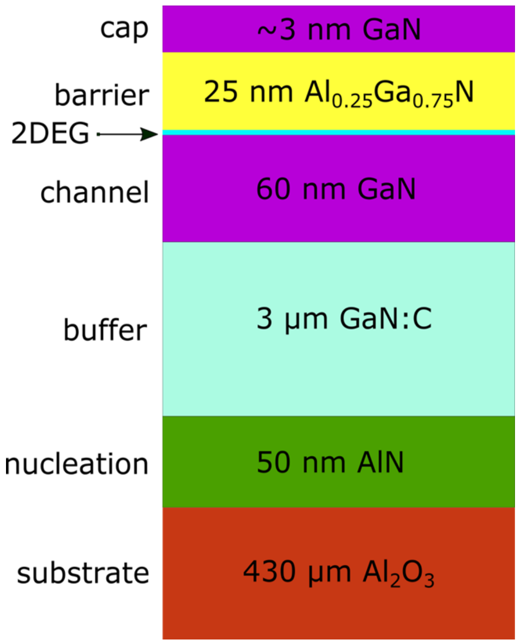

Figure 3.1: Schematic drawing of the wafer structure used in this thesis for fabricating the radiation detector, with the location of a 2DEG between the channel and barrier layer.

before they were laser-scribed into chips of $9x9\ mm^2$. The average sheet resistance R_S from Figure 3.2 was $412.75\,\Omega/s$.

As the material with the highest quality is located at the center of the wafer, pieces from this area on both wafers were used for the final measurements. For separation of the chips, a gentle push from the scribed side was required. For this the wafer was fixed between two plastic blocks and pushed on the free end [105].

After extraction of proper pieces, the samples were cleaned in an ultrasonic bath (Sonorex Super 10 P, Bandelin, Germany) in acetone for 20 min at medium intensity, then treated in isopropanol under the same procedure and then finally rinsed with deionized water for 10 min and dried with N_2 gas.

3.1.2 AlGaN/GaN - High Electron Mobility Transistor

In this thesis, the AlGaN/GaN - HEMT based devices were fabricated at the Instytut Technologii Elektronowej (Institute Electronic Technology) in Warsaw, Poland, to ensure the quality of the fabrication process. The whole process was conducted by the scientific personnel of the institute, on the scribed pieces of the Al_2O_3 wafer mentioned in Section 3.1.1. Technical characteristics of the desired layers' structure were provided in advance, in

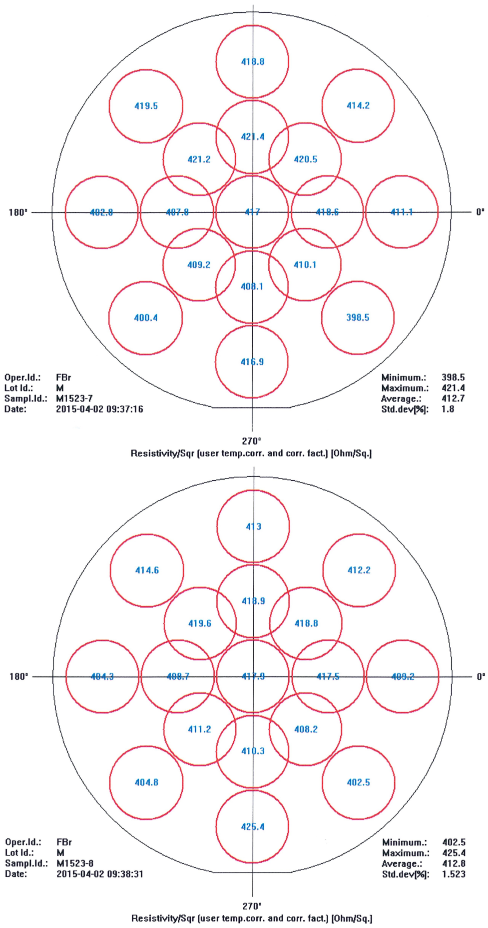

FIGURE 3.2: Schematic drawing of sheet resistance distribution for the wafers produced in the frame of this thesis for different areas. The numerical values are given in terms of Ohm/Sq.

order for the technicians to modify the steps of photolithography. The order of fabricated layers was as folllows:

1. Ohmic contacts with alignment marks for layers positioning.

2. MESA structure, which is the layer for structuring the underlying 2DEG by ion implantation.

3. Passivation layer, meaning the growth of an insulating layer through Atomic Layer Deposition (ALD) over the complete sample.

4. Structuring of the dielectric that is used to open the previous passivation layer for the source and drain contacts.

5. Metallization for source, gate and drain contacts.

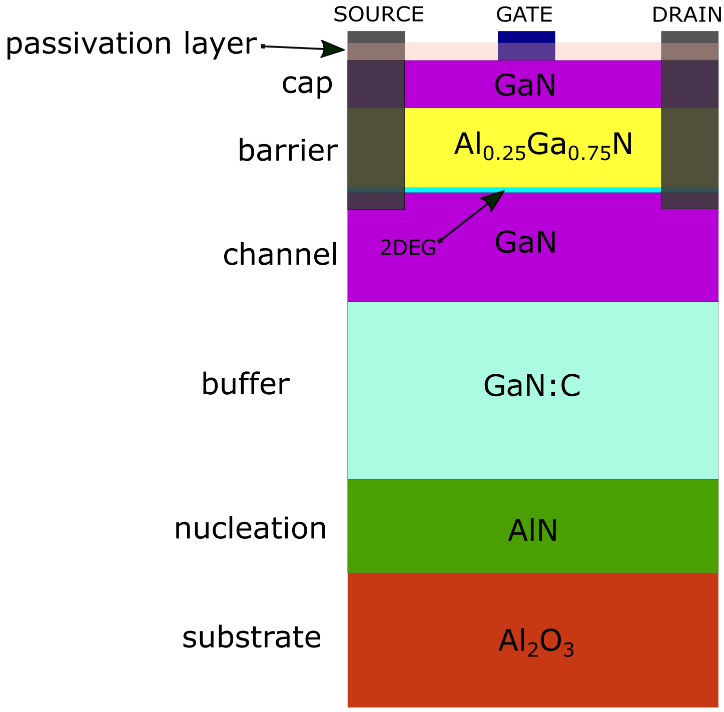

Figure 3.3: Schematic cross section of the GaN-HEMT device produced as part of this thesis, with contact pads and passivation layer.

The chromium (Cr) lithographic photomask that was used for this specific purpose, was also generated at the same facility to maintain the same quality standards. Figure 3.4 shows the CAD design of the photomask, while Figure 3.5 shows a picture of the actual photomask.

The final chips were meticulously cleaned in clean room environment, in order to remove any dust particles that would affect the performance of the produced devices. The chips were placed into acetone for 10 min in the ultrasonic bath (Sonorex Super 10 P, Bandelin, Germany) at low intensity. Then the devices were placed into isopropanol and treated for 10 min in an ultrasonic bath at low intensity. Finally, the devices were cleaned with deionized water for 10 min in the ultrasonic bath at medium intensity, followed by rinsing in deionized water and drying with N_2 gas.

Then the cleaned chips were positioned at the centre of a rectangle lead chip carrier (28 Lead Side Brazed Package, Kyocera, Japan) with given dimensions 1.4 in x 0.61 in, in clean room environment with the use of silver glue. Upon drying of silver glue, gold (Au) bonds were formed between the gate, source and drain contacts of each the GaN-HEMT devices and the chip carrier pins, with the use of a wire bonder (Model 747677E, West-Bond, USA). Figure 3.6 shows the final six chip carriers with the bonded devices, inside a transport box.

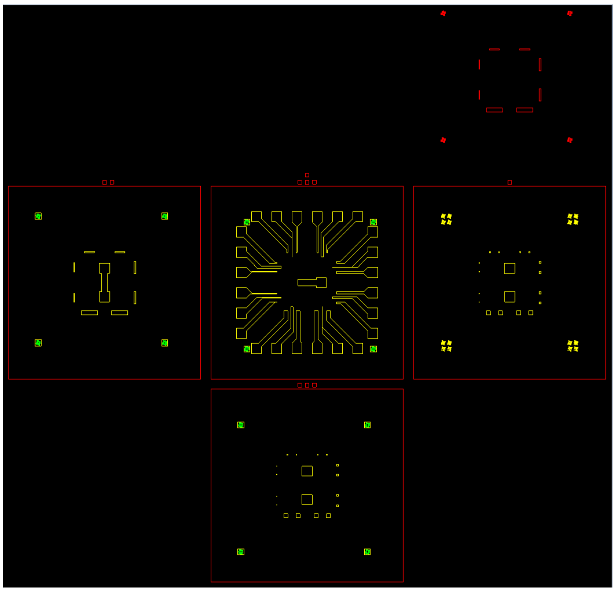

FIGURE 3.4: CAD file of the photomask corresponding to the different layers that were required to fabricate a GaN-HEMT device.

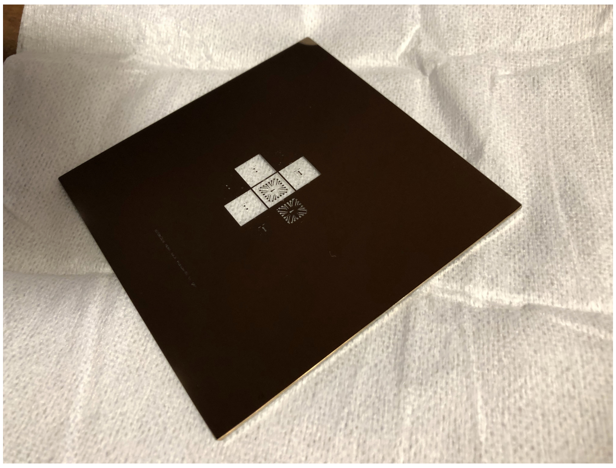

FIGURE 3.5: Photo of the actual chromium (Cr) photomask that was generated from the design of Figure 3.4.

3.1.3 $LiNbO_3$ - Surface Acoustic Device

In this work a lithium niobate ($LiNbO_3$) substrate was used for the fabrication of the required delay-line (Table 3.1):

For launching the surface acoustic waves, two IDTs were deposited on each of the 128° Y-cut $LiNbO_3$ substrates by evaporating 5 nm of titanium (Ti) and 50 nm of gold (Au) employing optical lithography and a subsequent lift-off technique, according to the general description in Chapter 2.

The fabricated IDTs included a Split-4 pattern, which resulted in a fundamental frequency of 113.00 MHz, which allows higher harmonic gen-

Figure 3.6: GaN-HEMT devices produced as part of this thesis inside a transport box after completion of the bonding procedure.

Substrate	Propagation	Propagation velocity (m/s)	K^2 (%)
128° Y-cut $LiNbO_3$	X	3979	5.4

Table 3.1: Table of used lithium niobate substrate, with information about the propagation direction, velocity and electromechanical coupling (K^2) [75].

eration of the third, fifth and seventh surface acoustic wave mode.

3.1.4 Hetero-epitaxial Diamond

In this work, hetero-epitaxial diamond was used that was deposited on the multilayer substrate consisting of iridium/yttria-stabilized-zirconia/silicon (Ir/YSZ/Si). The buffer layer of yttria-stabilized-zirconia was grown with the use of pulsed laser deposition (PLD) on a 4 inch Si (001) wafer, while iridium was deposited by e-beam evaporation. The details about this particular technique were described in Chapter 2. In order to generate epitaxial diamond nuclei on iridium, bias enhanced nucleation (BEN) treatment at a voltage of about -300 V in a gas mixture of 3% CH_4 in H_2 was applied.

Microwave plasma chemical vapor deposition (MWPCVD) was used to grow a sample with a thickness of approximately 1.3 mm using a gas mixture of 8% CH_4 in H_2 without any intentional nitrogen N_2 addition. Two plates of 5 x 5 x 0.5 mm^3 were prepared from the upper part of the sample with highest structural quality by laser cutting and mechanical polishing. Both sides of each sample were treated for 15 min in air plasma at approximately 1 mbar in order to guarantee an oxygen termination of the surface.

3.1.5 Hybrid-Device Fabrication

The $LiNbO_3$ SAW devices were thoroughly cleaned to remove any dust particles from the delay-line surface, in clean room environment. The devices were placed into acetone for 5 min in an ultrasonic bath (Sonorex Super 10 P, Bandelin, Germany) at medium intensity. Then the devices were placed into isopropanol and treated for 5 min in the ultrasonic bath at medium intensity. Finally, the devices were cleaned with deionized water for 10 min in the ultrasonic bath at medium intensity, followed by rinsing in deionized water and drying with N_2 gas. The above mentioned cleaning process was repeated with the CVD diamond samples.

Then the cleaned SAW devices were positioned at the centre of round (diameter: 17.5 mm) chip carriers, in the clean room with the use of silver glue. Here, upon drying of silver glue, aluminium (Al) bonds were formed between the contacts of IDTs on the SAW device and the chip carrier pins, with the use of wire bonder (Model 747677E, West-Bond, USA). Upon successful bonding and in order to ensure the endurance of the bonds at the pins, one drop of silver glue per bond was used.

After bonding, the CVD diamond samples were aligned between the IDTs of the SAW device. Special attention was given to prevent contact between the CVD diamond samples and the IDTs. In order to avoid scratches from CVD diamond on the delay-line, a drop of deionized water was used to position the CVD diamond with the use of an optical microscope (Olympus, Japan) connected to a computer, as in Figure 3.7.

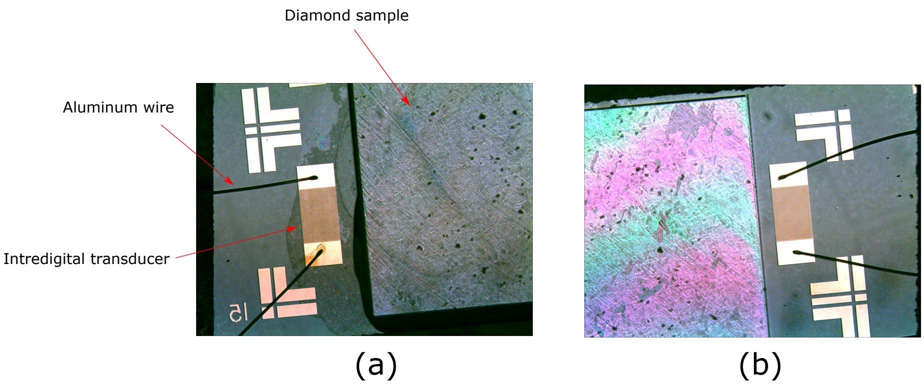

FIGURE 3.7: Pictures of CVD diamond sample in alignment with the delay-line elements from optical microscope. In both pictures the wires of the bonded IDTs are shown (black colour wires), as well as the gap between the CVD diamond sample and the IDTs. (a) part of deionized water drop is visible as black colour under the CVD diamond. (b) the iridescent diamond surface is caused by the modification of light conditions compared to (a).

To prevent the movement of the CVD diamond, as well as to ensure the direct contact with the $LiNbO_3$ surface, a modified identical chip carrier was used to gently press down the CVD diamond. Moreover, the inner dimensions of the chip carrier were modified, with the use of a drilling machine, to ensure the direct exposure of the sensor to a radiation beam. Figure 3.8 shows a description of the hybrid structure.

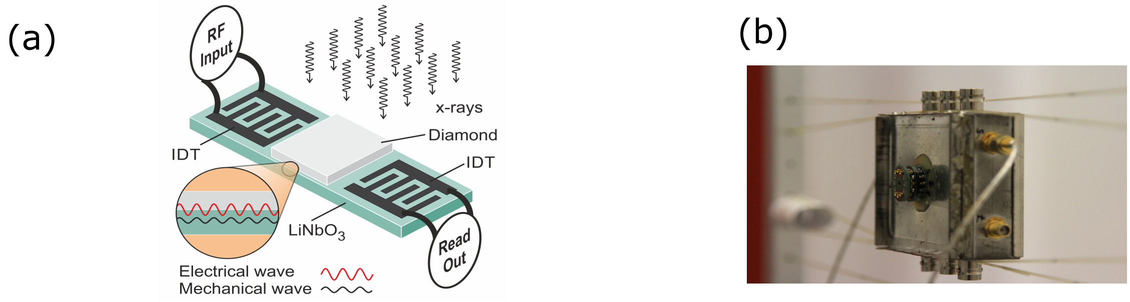

Figure 3.8: Description of the hybrid structure. a) Overview of working principle under ionizing radiation. The CVD diamond is mechanically pressed against the surface of the $LiNbO_3$ substrate. The electric field complementing the surface acoustic wave penetrates into the CVD diamond sample, due to the very small gap between the $LiNbO_3$ delay-line and the CVD diamond. b) Final device during characterization experiments.

3.2 Experimental Methods

3.2.1 AlGaN/GaN-Device Operation

The final AlGaN/GaN-HEMT device was characterized with the use of two identical source-measurement units (SMUs) (2400 SourceMeter®, Keithley, USA). Both units were operated at room temperature without additional cooling and were interconnected through a general purpose interface bus (GPIB) connection (IEEE-488 INTERFACE). Data acquisition, as well as remote control of the units, was achieved with the use of a specialized written program in LabView (National Instruments, USA), as shown in Figure 3.9. To achieve the desired measurement accuracies, the units were turned on and allowed to warm up for at least one hour following manufacturer's recommendations [106].

As each chip contains nine devices accommodated on a chip carrier, it was more convenient to design an experimental setup that would allow easy switch of the device under testing. Figure 3.10 shows the aluminium measurement box with steel front cover, that was designed and fabricated for this scope.

The device was operated under room temperature conditions throughout this thesis. Initial testing was conducted, in order to define the devices that were operational by measuring standard I-V curves for different gate

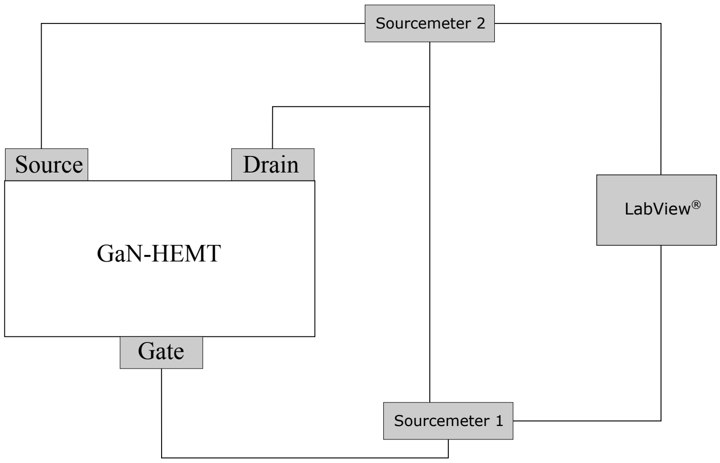

FIGURE 3.9: Schematic overview of the measurement setup used in this thesis for characterization of the produced AlGaN/GaN-HEMT device.

FIGURE 3.10: (a) Front view of measurement box with the socket for the chip carrier. (b) Inside view of the measurement box with the BNC cables soldered to the electric board. (c) Rear view of the measurement box with the BNC connectors corresponding to the individual device contacts. (d) Lead chip carriers with the bonded AlGaN/GaN-HEMT devices.

voltages [107]. As it was demonstrated by other groups that AlGaN/GaN-HEMT devices show increase in channel conductivity as well as a change in drain current under UV light conditions [108][109], the HEMT devices were investigated in absence of any natural or physical sources of light to eliminate any influence on detector's response as result of light absorption.

3.2.2 Hybrid-Device Operation

The device under test was characterized with a calibrated network/spectrum analyzer unit (Model ZVL3/ZVL-K1, Rohde & Schwarz, Germany).

The unit was connected with the device using coaxial transmission cables. For acquisition of the data obtained with network/spectrum analyser unit, a dedicated program in LabView (National Instruments, USA) was written, that provided control of the unit via Ethernet connection. In network analyzer mode, the scattering parameters (S-parameters) of the lithium niobate IDTs were measured (Figure 3.11).

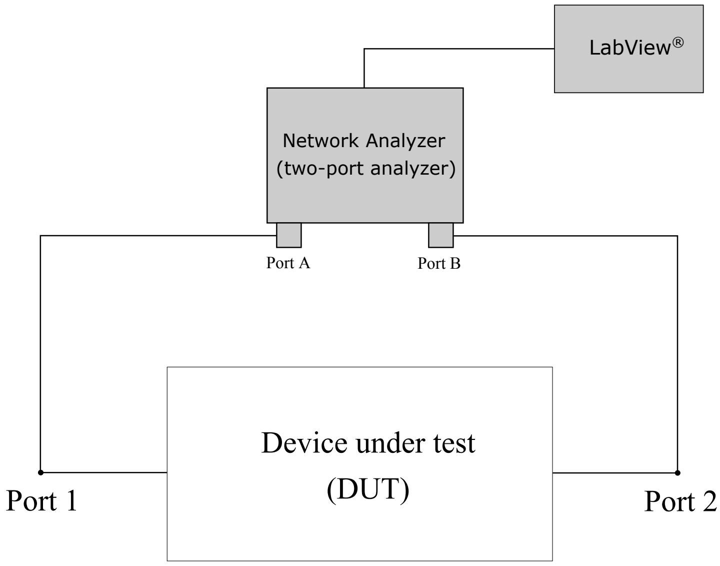

Figure 3.11: Schematic overview of measurement setup with network analyzer.

A brief schematic explanation of the relevant scattering parameters for a two port device is shown in Figure 3.12.

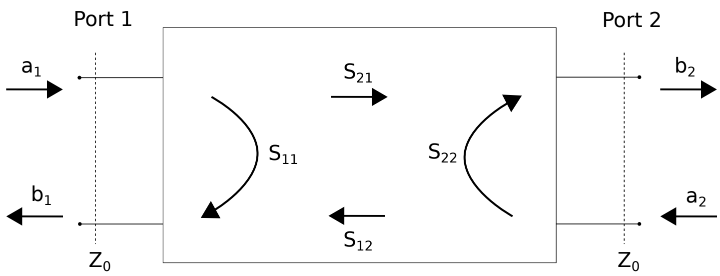

Figure 3.12: Incident wave a and reflected wave b with the defined scattering parameters S_{11}, S_{12}, S_{21} and S_{22}, for a reference impedance of $Z_0 = 50\Omega$. The latter renders a compromise, that relates to the coaxial transmission lines and optimises the performance, between the minimum attenuation at $Z_0 = 77\,\Omega$ and the maximum power handling capacity at $Z_0 = 30\,\Omega$ [86].

In Figure 3.12 the S-parameters are defined as the ratios of the incident wave a and the reflected wave b. These ratios can be obtained from the S-parameter matrix (S-matrix) of equation (3.1).

$$\begin{bmatrix} b_1 \\ b_2 \end{bmatrix} = \begin{bmatrix} S_{11} & S_{12} \\ S_{21} & S_{22} \end{bmatrix} \begin{bmatrix} a_1 \\ a_2 \end{bmatrix} \tag{3.1}$$

A network analyzer generates and visualizes the above mentioned S-parameters in form of impedance vs frequency response. The frequency response of surface acoustic wave resonators determines the resonant operational frequency of the device.

Furthermore, in spectrum analyzer mode, changes in amplitude of the SAW were measured as a function of time with the use of the zero span mode. For this purpose, the input port of the device was also connected to a signal generator (SMB-100A, Rohde & Schwarz, Germany), providing the proper characteristic frequency to the system (Figure 3.13).

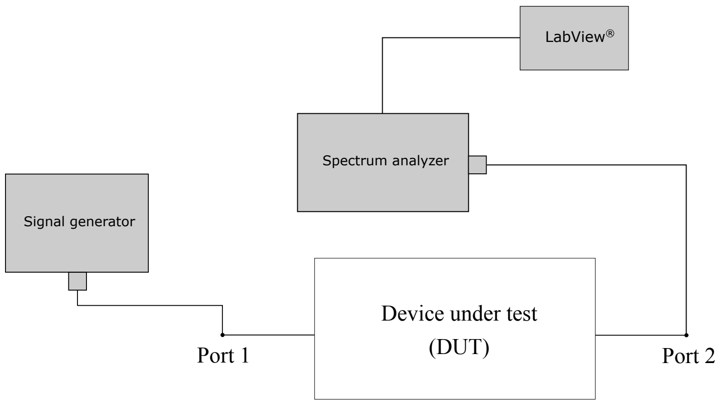

FIGURE 3.13: Schematic overview of measurement setup with spectrum analyzer.

The device was operated in a temperature-controlled environment with the use of a hybridization oven (Model HB-1000, UVP, USA). To control the humidity level inside the hybridization oven, orange silica gel bags (50 g (9 x 12 cm), Carl Roth, Germany) were used. Temperature and humidity levels were monitored and recorded with one minute sample rate, using a datalogger (Model OPUS 20, Lufft, Germany) connected via USB to a PC, together with the specialized software SmartGraph3 (Lufft, Germany).

3.2.3 X-ray Radiation Beam

The controlled X-ray irradiations were performed with an irradiation facility (MG 160, Philips Industrial X-rays, Hamburg, Germany) in the IAEA-WHO Second Standard Dosimetry Laboratory at Helmholtz Zentrum München. The devices were irradiated on a calibration bench under monitor control (TM 786, PTW Freiburg GmbH, Germany) with an electrometer (IQ4, PTW Freiburg GmbH, Germany). Radiation qualities of N40 (40 kV / 20 - 45 mA), N60 (60 kV / 20 - 45 mA), as well as C60 (60 kV / 45 mA) with

3.9 mm aluminium (Al) filtration were used. Figures 3.14 and 3.15 show the sideview of the x-ray facility, together with the additional equipment that was used during the radiation characterization measurements.

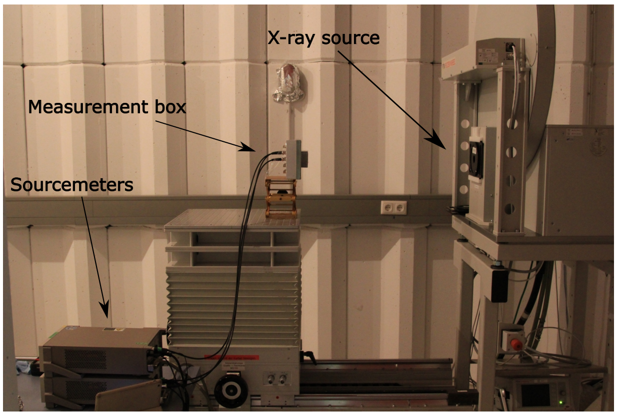

Figure 3.14: Side view of x-ray irradiation facility with additional measurement equipment for the characterization of AlGaN/GaN-HEMT devices.

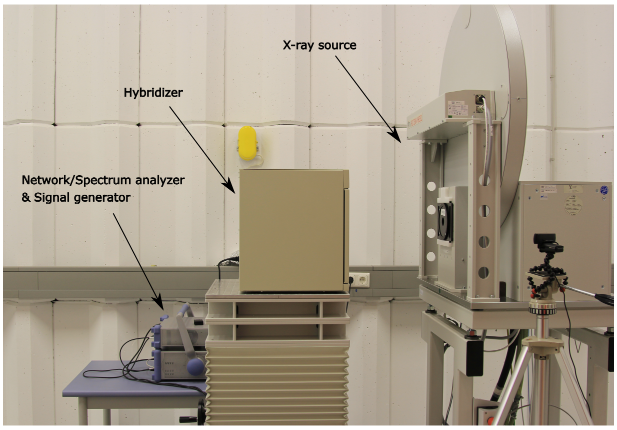

Figure 3.15: Side view of x-ray irradiation facility with additional measurement equipment for the characterization of $LiNbO_3$/CVD Diamond hybrid-devices.

Moreover, different dose-rates were produced through adjustment of tube current, between 20 - 45 mA as it was mentioned above, or variation of distance between the device under testing and the x-ray tube. Unless otherwise noted, for measuring air kerma doses a calibrated ionization chamber (DC300, IBA Dosimetry GmbH, Germany) with a dosimeter (DOSIMAX plus A, IBA Dosimetry GmbH, Germany) was used.

3.2.4 C-arm System

The behaviour of the developed hybrid-device under medical radiation qualities was also investigated for radiological equipment typically used as diagnostics within an emergency room (ER) and operating room (OR). For this purpose, a mobile C-arm fluoroscopic X-ray system was employed (SIREMOBIL Compact L, SIEMENS AG, Germany), as medical professionals are exposed to ionizing radiation during a variety of diagnostic imaging and invasive surgical procedures using such fluoroscopic systems [110][111][112]. Figure 3.16 shows the clinical system that was used, together with the supportive equipment and radiation protection measures.

FIGURE 3.16: Side view of the C-arm fluoroscopy X-ray system used in this thesis, with the measurement equipment on the left side and the radiation protection equipment in front of the sample.

3.2.5 Computed Tomography Scanner

Radiation measurements with clinical diagnostic equipment were performed in the former Institute of Radiation Protection at Helmholtz Zentrum München, in order to evaluate the behaviour of the radiation detectors developed in the frame of this thesis under medical radiation qualities. Computed tomography (CT) scanners have been playing a crucial role in medical diagnostics since their introduction in 1970s, becoming an indispensable diagnostic tool within radiology departments [113]. The investigation of hybrid-device developed in the frame of this thesis was performed using an in-house CT scanner (BrightSpeed, General Electric, USA), as in Figure 3.17, under controlled environmental conditions and for two different build-in filter-settings; head and body. These two filter-settings modify the bowtie filter of the CT scanner, according to the selected scanning protocol.

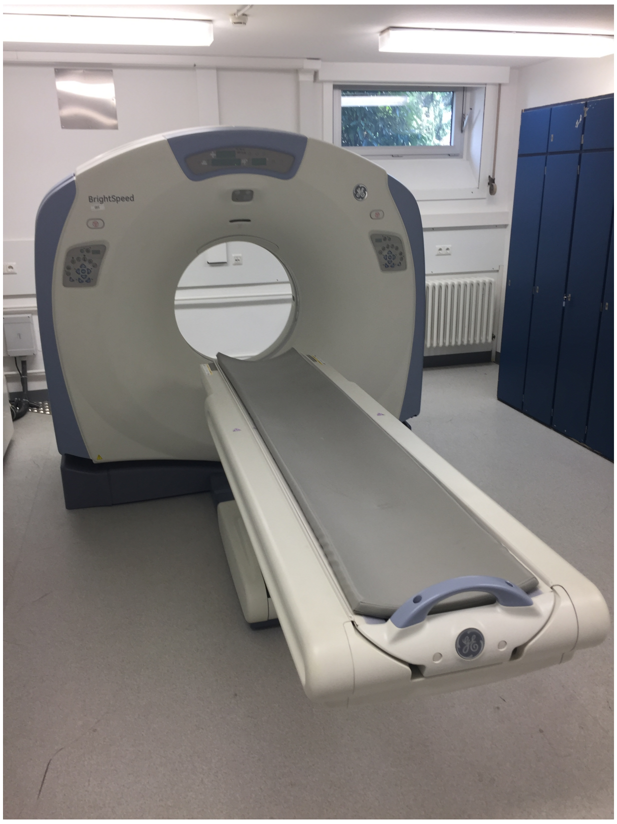

Figure 3.17: Front view of the CT scanner system, installed at the former Institute of Radiation Protection/Helmholtz Zentrum München.

Results 4

4.1 Characterization of AlGaN/GaN-HEMT

An investigation of the electrical characteristics of AlGaN/GaN-HEMT was performed under ionizing radiation. The experimental method that was presented in Section 3.2.1 was followed, in order to investigate the response of the HEMT device, using an unfocused x-ray beam. Ionizing radiation could potentially impact the performance of semiconductors because of electron-hole pair creation [114], thus affecting the DC measurements that reveal the performance of the semiconductor component. For this reason, typical I-V curves in absence and in presence of ionizing radiation were measured as shown in Figure 4.1. By keeping the source-drain voltage constant at 10 V, gate voltage sweeps were performed from -80 V to zero with steps of 1 V. From Figure 4.1 it can be deduced that AlGaN/GaN-HEMT is normally-off for gate voltages below -38 V, while in the presence of ionizing radiation the source-drain current reaches saturation faster and at a marginally lower level (about 4% less) than in absence of ionizing radiation. Moreover, the threshold voltage that is needed to establish a conductive connection between source and drain, shows a minuscule depletion in presence of ionizing radiation. Such behaviour confirms reports in the literature about the degradation of saturation source-drain currents [115] and about the negative-voltage threshold shifts in presence of ionizing radiation [17][116][117].

In principle, the suggested AlGaN/GaN-HEMT detector that is presented in this study, should be operated in normally-off mode according to the radiation detector for focused radiation beam reported in Ref. [11]. From the I-V curves shown in Figure 4.1 the gate-voltage region can be

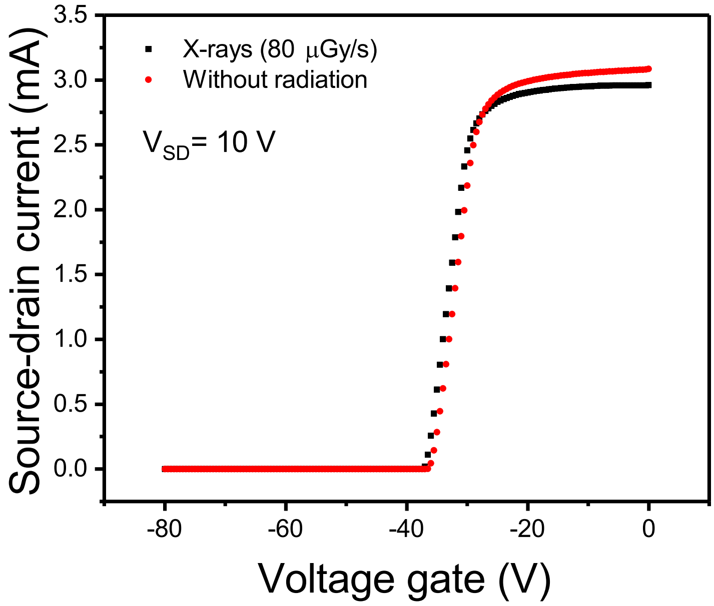

Figure 4.1: I-V characteristics for the AlGaN/GaN high electron mobility transistor produced in the frame of this thesis, in absence (red coloured symbol) and in presence (black coloured symbol) of radiation with radiation quality of N60 (60 kV / 45 mA) for room temperature conditions and in absence of natural or artificial light sources. The x-axis corresponds to gate voltage while the y-axis to source-drain (SD) current.

identified where the HEMT is normally-off, as well as the stability of the off-mode. As it can be seen the transistor exhibits tremendous stability, thus allowing for further investigations under irradiation while in off-mode.

4.2 Radiation Measurements with AlGaN/GaN-HEMT

As it was experimentally proven in Section 4.1, the region of gate-voltage where the transistor can be operated in off-mode extends from -80 V up to -38 V. Following the requirements that were elucidated in advance, it was chosen to continue the investigation of the transistor using -50 V as reference gate-voltage. Prior to any measurements, the influence of the measurement box on total signal response should be investigated. In addition to this, the electrical components such as motherboard, BNC connectors, BNC cables and chip socket that were fabricated and soldered, could be potential factors of inaccurate measurements as well. For these reasons, box stand-alone measurements were performed as shown in Figures 4.2a and 4.3a for radiation qualities N40 (40 kV / 20 - 45 mA) and N60 (60 kV / 20 - 45 mA) respectively, for a source-drain-voltage of 10 V. Upon completion, the response of the AlGaN/GaN-HEMT sensor that was mounted on the measurement box was measured using the same settings both for electrical and radiation equipment as shown in Figures 4.2b and 4.3b. The custom-made aluminium measurement box, with all the additional electrical components, generates an electrical current in the pico-ampere (pA) range.

The current increased with increasing dose-rates as is shown in Figures 4.2a and 4.3a, thus contributing to the total response value. Irradiating the measurement box having AlGaN/GaN-HEMT sensor mounted with x-rays, a similar behaviour can be seen in Figures 4.2b and 4.3b. Subtracting the average response of the measurement box from Figures 4.2b and 4.3b, the actual sensor response could be extracted for every measured dose-rate as shown in Figures 4.4 and 4.5. The response of the detector was evaluated by calculating the mean source-drain current and the standard deviation that corresponds to the measurement points for 200 seconds of the total 300 seconds of radiation exposure. The results of this statistical analysis are included at the error bars of Figures 4.4 and 4.5.

The linearity of sensor response with dose-rate, as well as the rapid response time, shows a similar behaviour to that reported by Ref. [11] and [64], allowing the consideration for further investigation under medical radiation fields. Comparing the sensor response with the reported literature by Ref. [11], [118] and [9], it may be concluded, however, that the detector response (which is only in the pA range) is too small to be used as a means for radiation detection applications [106].

From this perspective it was inevitable to explore alternative approaches and renounce the AlGaN/GaN-HEMT approach. After careful consideration of potential materials that could be used as radiation detectors [119][120], it was decided to proceed with synthetic diamond as detector material given the advantages of this material as described in Section 2.2, in combination with the advantages of SAW-based devices as reported in the literature [121][122]. As a consequence, the AlGaN/GaN-HEMT system was not subject of further investigation under radiation exposure. Thus, the following subsections in this Section describe the experimental results of a SAW-based radiation detector with synthetic diamond as sensing layer.

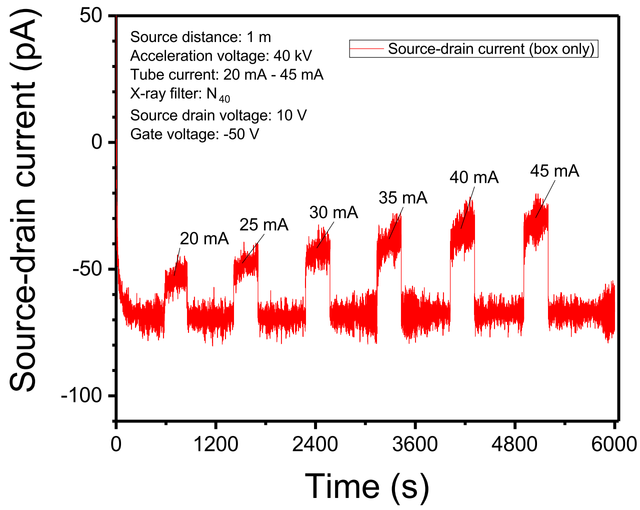

(a) Response of measurement box under ionizing radiation for different dose-rates.

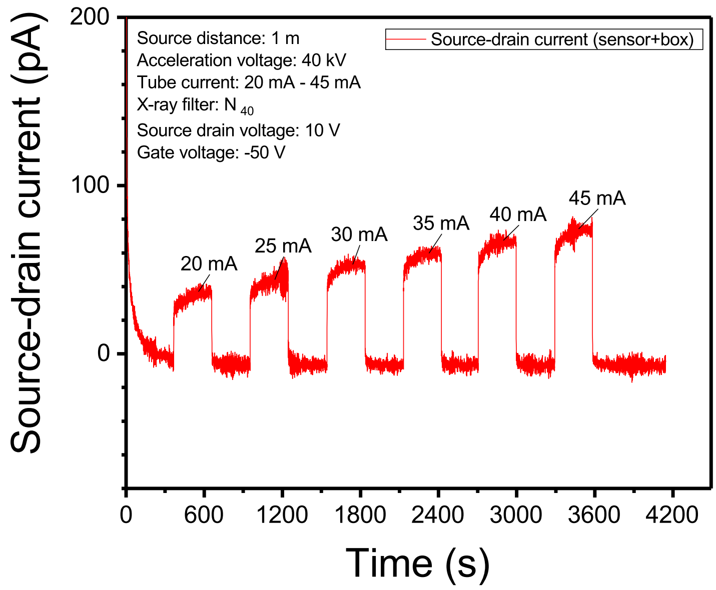

(b) Response of sensor mounted on measurement box under ionizing radiation for different dose-rates.

Figure 4.2: Dependence of source-drain current on dose-rate under constant gate-voltage and source-drain-voltage of -50 V and 10 V, respectively, for radiation quality N40 with (a) measurement box only and (b) AlGaN/GaN-HEMT sensor mounted to the measurement box.

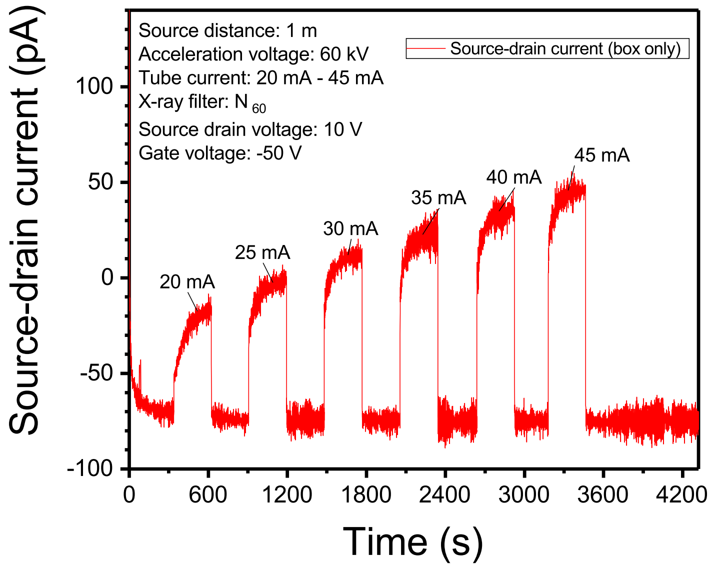

(a) Response of measurement box under ionizing radiation for different dose-rates

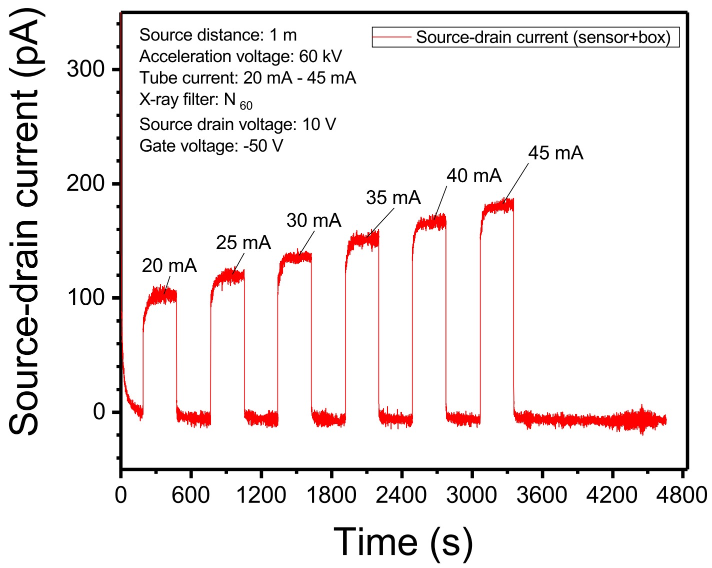

(b) Response of sensor mounted on measurement box under ionizing radiation for different dose-rates.

FIGURE 4.3: Dependence of source-drain current on dose-rate under and source-drain-voltage of -50 V and 10 V, respectively, for radiation quality N60 with (a) measurement box and (b) AlGaN/GaN-HEMT sensor mounted to the measurement box.

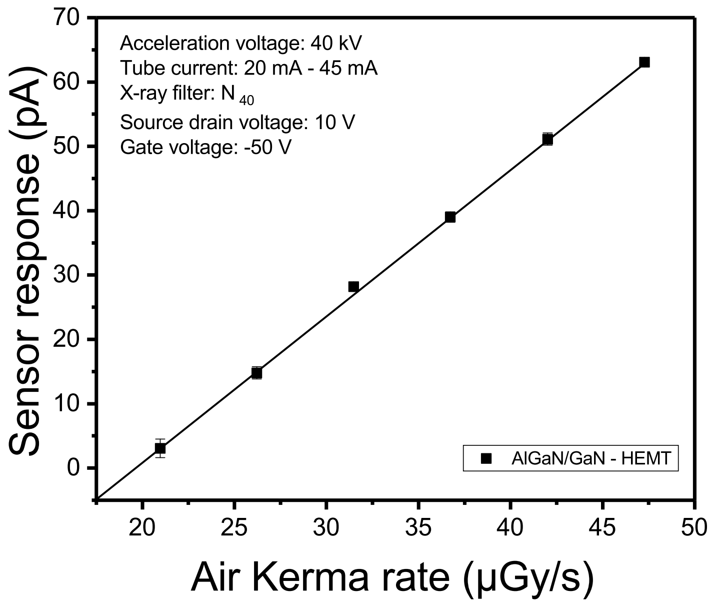

Figure 4.4: Plot of final sensor response as a function of air kerma rate for the AlGaN/GaN-HEMT sensor produced in this thesis under x-ray irradiation of N40 quality. Non-visible error bars correspond to uncertainties that are smaller than the size of the symbols.

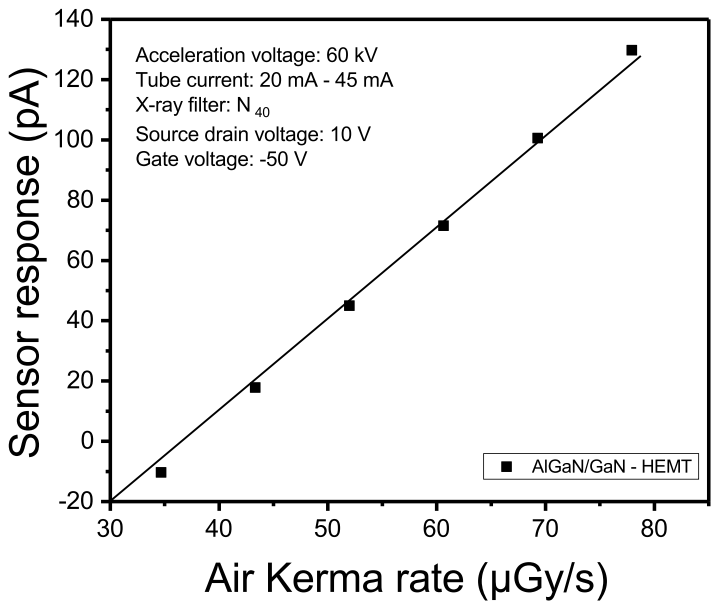

Figure 4.5: Plot of final sensor response as a function of air kerma rate for the AlGaN/GaN-HEMT sensor produced in this thesis under x-ray irradiation of N60 quality. Non-visible error bars correspond to uncertainties that are smaller than the size of the symbols.

4.3 Characterization of $LiNbO_3$ Delay-Line

After dicing the wafer with the fabricated delay-lines on top, the transmission frequency was characterized by using a vector network analyser as shown in Figure 4.6. As $LiNbO_3$ delay-lines are expected to be temperature-sensitive [75], extra care was taken in order to eliminate any effects from changes on temperature as it was described in Section 3.2.2.

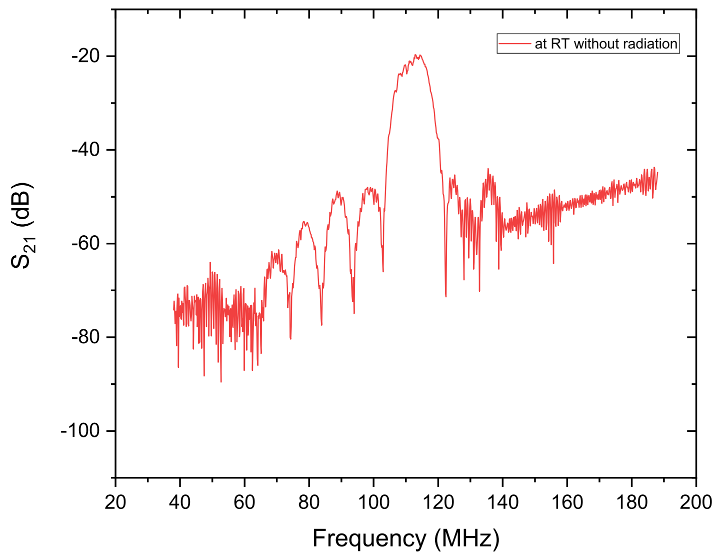

FIGURE 4.6: Characterization of transmission frequency of the $LiNbO_3$ delay-line with a network analyzer at temperature of $24°C$. The characteristic resonant frequency of the Split-4 IDTs of the delay-lines that were used throughout this work is 113 MHz.

The Split-4 design of the IDTs on the piezoelectric material, showed a characteristic frequency of 113 MHz which was used for the rest of this work.

Moreover, as the substrates were planned to operate in a radiation environment, it was necessary to determine the behavior of the transmission frequency parameter S_{21} curve during irradiation with x-rays.

Figure 4.7 shows the characteristic transmission curve S_{21} for the used $LiNbO_3$ SAW delay-line under x-ray exposure for the same environmental conditions as before. A radiation quality of C60 (60 kV / 45 mA) with 3.9 mm aluminium (Al) filtration was used, at a distance of 400 mm from the x-ray tube. The measured dose-rate for this radiation quality and distance was $3704 \pm 2\,\mu Gy/s$.

From Figure 4.7 an almost identical behaviour between the two transmission curves was noticed in terms of resonant frequency, thus no frequency shift was observed. In addition to this, there was an extremely small signal attenuation of approximately 0.001 dB between the two transmission

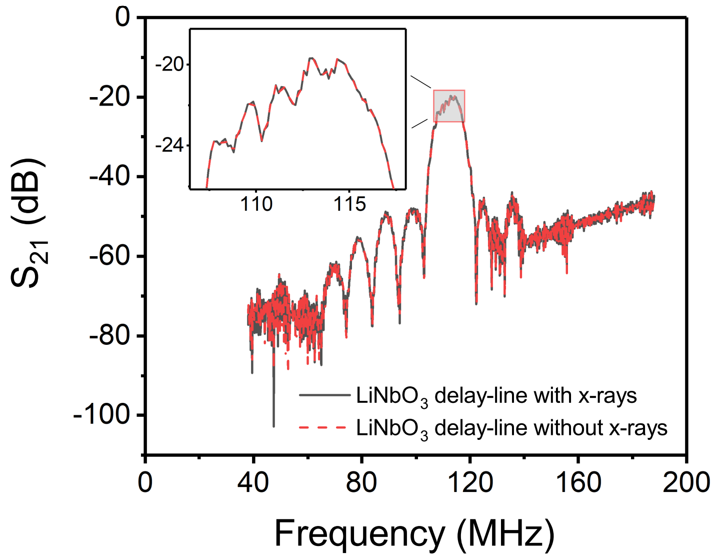

Figure 4.7: Characterization of transmission frequency of the $LiNbO_3$ delay-line measured with a network analyzer at temperature of $24°C$ with (red colour curve) and without (black colour curve) radiation. Inset shows in magnification, part of the frequency response curve of the delay-line where the resonance occurs.

curves. The attenuation of the SAW signal can be explained by a change of the dielectric constant of the $LiNbO_3$ material during irradiation. This variation occurs through the formation of a space-charge region in close proximity to the surface of the non-linear dielectric material [26]. Due to the existence of such region near the surface of the material, large electric fields are generated on this part of the piezoelectric material. The creation of electron-hole pairs on the surface as consequence of ionizing radiation exposure will cause a perturbation into the charge distribution on the surface [26]. As a consequence, the electric field will cause a redistribution of the extraneous surface charge, resulting in the acceleration of electrons towards the surface where the high-field region prevails [26]. As the acceleration will extract energy from the electric field, a decrease in total energy should be expected that will expel electrons from the material due to the magnitude of the correlated equilibrium electron density that is not sustainable [26]. This radiation-induced non-equilibrium condition results in the decrease of the electromechanical coupling coefficient K^2, which depends on the dielectric constant of the material at similar conditions [26]. This dependence is expressed through equation (4.1)

$$\gamma = \frac{\epsilon_p}{\epsilon_p + \epsilon_0} \tag{4.1}$$

were ϵ_p is the effective dielectric constant, ϵ_0 the permittivity and γ is the drift parameter [123]. The dielectric constant ϵ for non-linear dielectric materials will increase as the generated electric field decreases, thus increasing the capacitance of the material [26].

Furthermore, measurements were made employing the spectrum analyzer with the external signal generator as it was described in the previous section: The same delay line was irradiated for 600 s followed by 250 s relaxation time, applying the same dose-rate as in the above mentioned experimental configuration with the vector network analyzer, as shown in Figure 4.7. Irradiating the delay line at the maximum dose-rate for 600 s shows a slight increase in the amplitude by 0.002 dB when the beam was switched on, but no visible response is observed after the switch off, as shown in Figure 4.8. Thus, it can be concluded that the effect of radiation on the signals of the SAW structure alone without the diamond is small enough that it does not question the sensor concept.

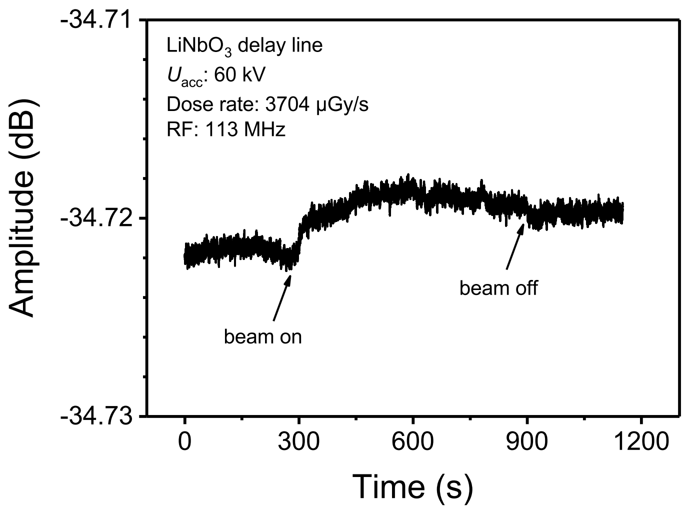

FIGURE 4.8: Amplitude when the $LiNbO_3$ delay-line without diamond was irradiated.

4.4 Radiation Measurements with the Hybrid-Device

4.4.1 Irradiations with x-ray and ^{137}Cs gamma-ray sources

After the characterization of the lithium niobate delay-line under irradiation and the fabrication of the hybrid-device, systematic measurements were performed employing the same configuration as used for Figure 4.8 measuring the attenuation of SAW signals under controlled temperature and for different dose-rates. The characterization included long irradiations, in order to evaluate whether the device will show saturation after relatively long irradiation; the recovery time after irradiation was also measured.

Figure 4.9 shows an example of the device response with details about the experimental protocol that was followed throughout this work. In more detail, the protocol that was followed included 10 min initial preradiation measurements to determine the baseline of the device for the given temperature and input power. The device under testing was then irradiated for 600 s followed by 1800 s relaxation time. A relatively long relaxation time of 1800 s was chosen to evaluate the stability of the device in case of consecutive irradiations. The data in Figure 4.9 permit several important conclusions: a) there is a clear response of the device upon x-ray exposure, yielding a signal with low noise, b) the signal has not reached a constant level even after 1800 s, which indicates high settling times, c) several repetitions of the switching with a constant duty cycle reveal a good reproducibility of a generated signals.

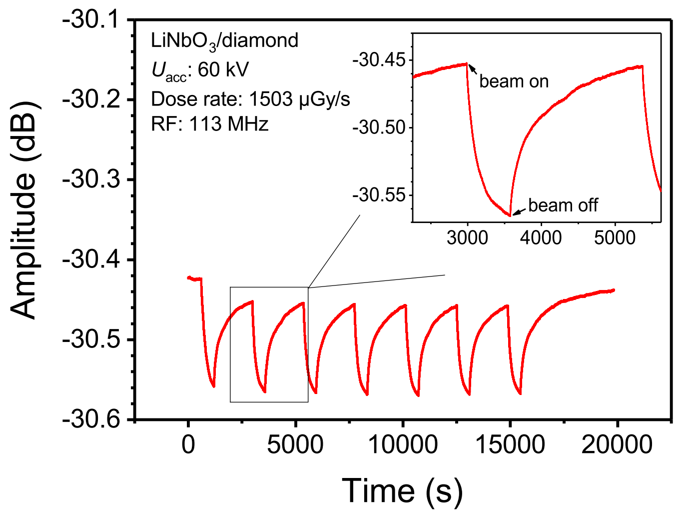

Figure 4.9: Example of hybrid-device response under ionizing radiation. The experiment included an irradiation time of 600 s followed by a relaxation time of 1800 s. Inset shows in magnification part of the response curve of the device.

In presence of ionizing radiation, radiation-induced electron-hole pairs are produced throughout the volume of the synthetic diamond layer, resulting in a change of conductivity. The variation in conductivity is detected through the interaction of the electric field of the SAW as it propagates along the delay-line and penetrates the volume of synthetic diamond layer. This interaction can be described by the plain relaxation model of Equations 2.34 and 2.35, describing the interaction between SAW and 2DES as it was presented in Section 2. The sandwich-like structure that is shown in

Figure 3.8, overcomes the low coupling coefficient K^2 (%) of semiconductor materials like GaN (K^2 = 0.09%) [124] by making use of their eminent electronic properties, in combination with the significantly higher coupling coefficient of 128° Y-cut X-propagated $LiNbO_3$ (K^2 = 5.6%) [125]. As it was mentioned earlier, using the proximity coupling technique, the sensing layer is brought into intimate contact with the surface of the delay-line through mechanical pressure, as shown in Figure 3.8. As the air gap between the sensing layer and the delay-line is significantly smaller than the wavelength of the SAW, the electric field that accompanies the SAW penetrates into the layer and interacts with the electric carriers, while the SAW propagates exclusively along the $LiNbO_3$ substrate, due to the acoustic mismatch between the two components [29][126]. Hence, the SAW electric field will interact with the non-piezoelectric synthetic diamond layer according to the suggested mechanism. The long time constant that can be extracted from Figure 4.9 can be explained in accordance with the semi-empirical model for the rise of RIC as shown in Figure 9. As maximum conductivity is reached by the irradiated material after a definable period of irradiation time, the decrease of conductivity will similarly follow a hyperbolic behavior with time until the inceptive conductivity of the irradiated material is reached, as shown in Figure 4.10.

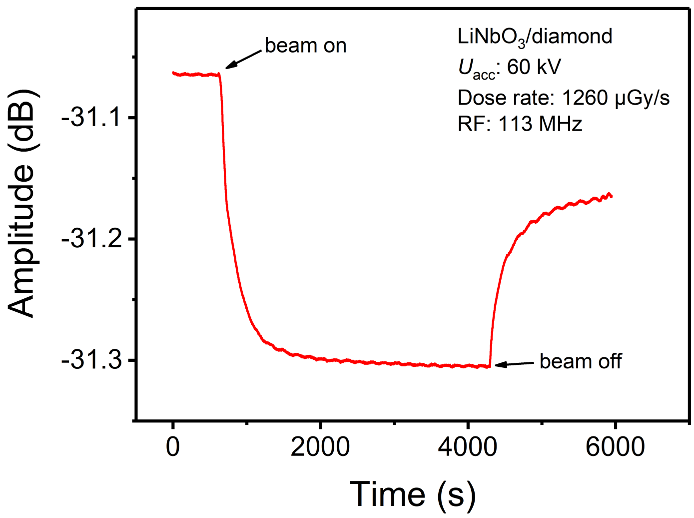

FIGURE 4.10: Change in amplitude of the transmitted RF signal for an increased exposure time of 3600 s. Within this time interval, the signal reaches a saturation value. Before the experiment, the device could settle without exposure overnight.

Thus, as the conductivity of synthetic diamond layer is slowly changed by the incident x-ray beam, the electric part of SAW interacts with the radiation-induced conductivity measuring the slow growth of the layer's conductivity as attenuation of the SAW signal. The reverse process happens when the x-ray beam is turned off, and the conductivity steadily decreases to its initial value.

The long rise and decay time constants (0.5–1 h) are critical features of the measured signals. They are similar to the values that have been found in the electrical measurements of the reference crystal equipped with metal contacts, which yields strong indications that they are caused by bulk properties rather than by the contacts [127]. They are also in good agreement with results reported in various former studies, which consistently found a correlation between high sensitivity or high gain values and long settling times [128][129][130]. This behavior was attributed to the incorporation of boron, which seems to be present in nearly every CVD setup as a background contamination [131]. It is concluded from the high dark conductivity that in the crystals used in the present thesis the boron concentration is higher than the nitrogen concentration, i.e., a small fraction of the boron is uncompensated by nitrogen. The interaction relevant for the energy deposition of photons in diamond depends on their energy. Below 100 keV, the absorption by the photoelectric effect dominates. In contrast, at higher energies, Compton scattering and pair production play a major role. Relevant for the present experiment is the generation of electron hole pairs in the crystal, which changes its conductivity (radiation-induced conductivity, RIC) [132].

As shown in Figure 4.10, the attenuated SAW signal is stabilized after approximately 1500 s of irradiation, while after switching-off the x-ray incident beam the hybrid system shows a rather slow recovery time, more than 1800 s until the initial value is reached again. Moreover, following Fowler's relation $\sigma \approx D$ [132], the radiation-induced conductivity is expected to be dose-rate dependent. By combining the dose-rate dependence of the conductivity with Equation 2.34, an increase in SAW signal attenuation with dose-rate is expected. This hypothesis was investigated by conducting further irradiations at different dose-rates employing the same configuration. As shown in Figure 4.11, a dependence of the SAW signal attenuation on dose-rate was indeed observed.

In addition to this, by applying the same experimental protocol under the same dose-rate, employing a ^{137}Cs gamma-ray source that produces photons of $\approx 662keV$, an attenuation which was higher by about 0.05 dB was observed compared to the attenuation observed for the x-ray source, as shown in Figure 4.12.

For the derivation of absolute values, a general problem was encountered with diamond detectors: an appreciable density of deep traps in the wide bandgap of the available crystals makes it difficult to transform the diamond sensor into an equilibrium state in acceptable time. Reports describe that the most reproducible detector results are obtained by performing several switching cycles or by pre-irradiating (priming) the sensor. The latter is even a mandatory procedure for commercial detectors containing carefully

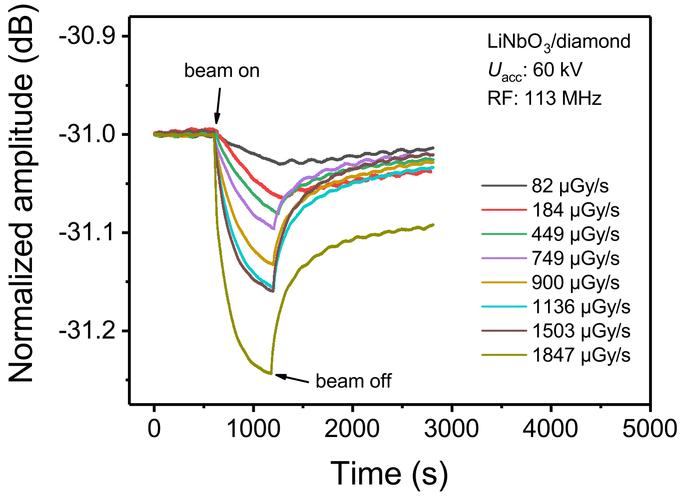

FIGURE 4.11: Example of radiation-induced response of the hybrid-device after overnight relaxation, under various dose-rates from an x-ray source for 600 s irradiation following 1800 s relaxation.

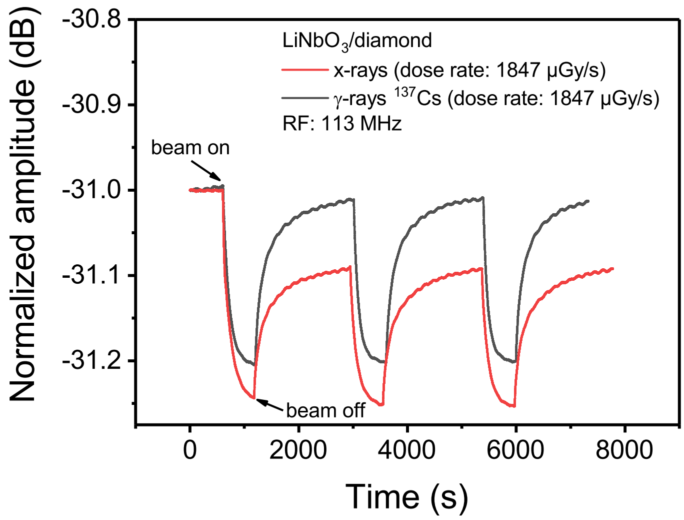

FIGURE 4.12: Example of radiation-induced response of the hybrid-device after overnight relaxation, under the same measured dose-rate for a ^{137}Cs gamma-ray source and an x-ray source.

selected crystals as regularly used in hospitals [133][134]. The problem is particularly present for the high gain heteroepitaxial diamond that was used in this part of the thesis. For the derivation of the values shown in Figure 4.13, it was therefore, determined the difference between the amplitude measured at the end of the first exposure cycle and the end of the first recovery cycle.

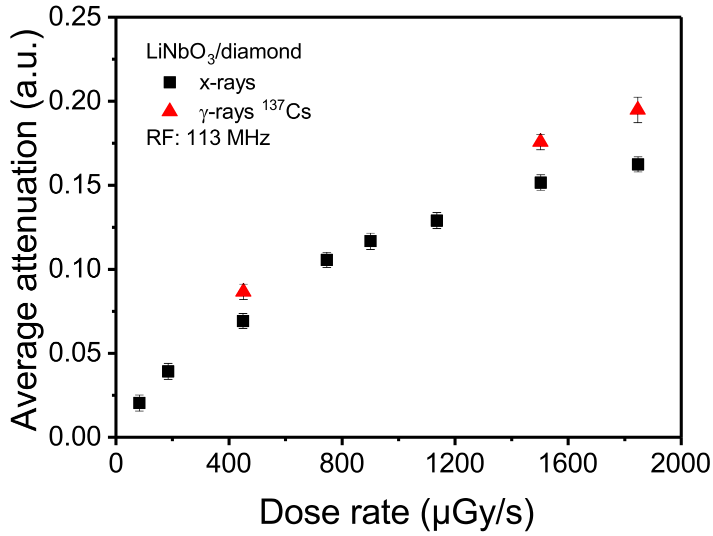

Figure 4.13: Dose-rate and energy dependence of SAW signal attenuation under stable temperature for x-ray and ^{137}Cs gamma-ray sources.

Over the whole range, the attenuation shows a sublinear variation with the dose-rate. This may partially be attributed to the relationship given by Equation 2.34 that predicts approximately a linear behavior at low conductivity σ, reaching a maximum and a transition to a decay $\approx 1/\sigma$ at high σ values. In addition, nonlinearities in scaling of the carrier density and conductivity in the diamond crystal with the dose-rate may also have an influence. Currently, the contributions of both effects cannot be decomposed. Provided that the effects are stable and reproducible, the nonlinearities in the characteristic curve are not an obstacle for quantitative measurements when appropriate calibration procedures are applied. As shown in Figure 4.13, irradiation with γ-rays of $\approx 662keV$ from the ^{137}Cs source yields a slightly higher attenuation $\approx 0.05dB$.

As the SAW signal attenuation increases with dose rate, it can be postulated that the response of the hybrid system developed in this thesis corresponds to the region that is defined by $\sigma < \sigma_m$ in Equations 2.34 and 2.35, expecting the attenuation to increase until $\sigma = \sigma_m$, where the maximum attenuation is observed [29][126].

4.4.2 Irradiations with mobile C-arm

The investigation with the mobile C-arm device shown in Figure 3.16, exhibited a fast response of the hybrid-device with incident beam, as shown in Figure 4.14. Within the exposure time of 120 s it is noticed that no saturation was achieved, as it was expected from Figure 4.10. Similarly, a relaxation time of 120 s was not expected to be sufficient for full recovery of the SAW signal to its initial value. The first round of irradiation shows an attenuation of the SAW signal of approximately 0.09 dB, a difference of 0.03 dB from the subsequent rounds, where there is an average attenuation of 0.06 dB accompanied by a progressive dive of the maximum attenuation value corresponding to the minima shown in Figure 4.14 for the specified timeframe. This steady decrease of the minima of the response curve is due to the short relaxation time that was chosen, which did not permit the recombination of all electron-hole pairs, resulting in an increase of electron-hole pair population from one round of irradiation to the next. For longer irradiation times, the device is expected to operate as in Figure 4.9 or Figure 4.10.

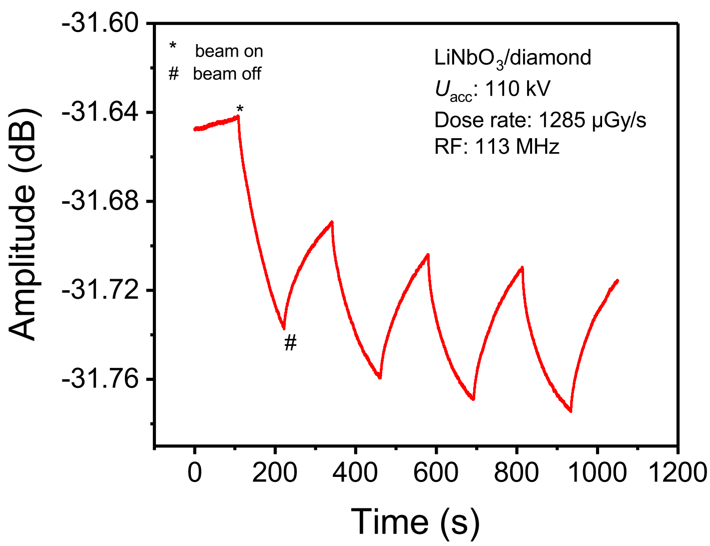

FIGURE 4.14: Characterization of the hybrid-device developed in this thesis, during exposure to ionizing radiation using mobile the C-arm device shown in Figure 3.16, under maximum dose-rate operation, following 120 s exposure and 120 s relaxation time, after overnight relaxation. The asterisk symbol indicates the start of irradiation, while the hash symbol corresponds to the termination of irradiation.

4.4.3 Irradiations with CT-scanner

The investigation of the hybrid-device was continued using an x-ray beam from the CT-scanner shown in Figure 3.17, under variable procedures. As shown in Figure 4.15, by employing the CT-scanner and performing irradiations without applying any diagnostic protocol under the same configuration as before, the behavior of the device was investigated for irradiation time of 10 s. The tube voltage was kept constant at 140 kV and through the modification of the tube current, it was possible to achieve different dose-rates (Table 4.1) and test the performance of the hybrid-device under variable radiation conditions.

Tube current (mA)	Filter	Dose-rate per 100 mA ($mGy/s/100mA$)	Dose-rate (mGy/s)
300	Head	3.78	11.34
300	Body	2.79	8.37
200	Head	3.78	7.56
200	Body	2.79	5.58
100	Head	3.78	3.78
100	Body	2.79	2.79
50	Head	3.78	1.89
50	Body	2.79	1.39

Table 4.1: Table of dose-rates used for the measurements shown in Figure 4.15.

The attenuation of the SAW signal shows a dose-rate dependence, as well as a relaxation time dependence. As it can be seen, for a dose-rate of 11.34 mGy/s the attenuation of the SAW signal is 0.15 dB, for 10 s total exposure time. As the dose-rate is reduced to 1.39 mGy/s, the attenuation decreased to 0.06 dB. For irradiation at 8.37 mGy/s, the measured response shows less attenuation compared to that at 5.58 mGy/s. It was explained earlier that during relaxation time the recombination of electron-hole pairs takes place and the charged electrons return to the valence zone, thus reducing the population of the electrons that are located at energy states in-between the valence and conduction bands. This reduction is expressed as relative increase of SAW signal attenuation, despite the expected decrease. At this point, it should be mentioned that the relaxation time between irradiations could not controlled by the user. On the contrary, it was controlled by the software of CT-scanner in order to protect the x-ray source of the radiological device from damage. This feature allowed to emulate as closely as possible the operation within a typical medical environment, where irradiation and relaxation times do not follow the strict protocols that were applied for the irradiations at the SSDL.

The performance of the hybrid-device was also evaluated using diagnostic/imaging protocols for three different areas of human anatomy, such as skull, pancreas and knee. These parts were selected on the basis of exposure time, medical diagnostic necessities and stability in acceleration voltage (120 kV) of the x-ray source. As traumatic brain injury (TBI) is a significant problem worldwide with tendency to increase [135], the necessity for CT-scanning rises the demands for radiation monitoring. Furthermore, the use of CT imaging to diagnose neoplasms such as pancreatic neuroendocrine tumors (PanNETs) [136] or pancreatic cystic lesions (PCLs) [137], triggered to investigate the performance of the hybrid-device for a pancreatic imaging protocol. Similarly, CT-scan imaging for knee arthroplastry

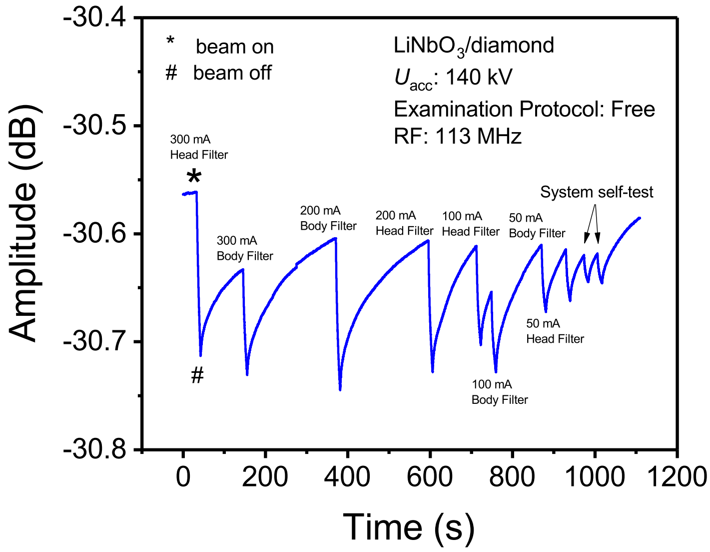

FIGURE 4.15: Radiation-induced response of the hybrid-device developed in this thesis, during exposure to an x-ray beam from a CT-scanner, without applying an examination protocol typical for medical examinations, after overnight relaxation. The asterisk symbol indicates the start of irradiation, while the hash symbol corresponds to the termination of irradiation.

[138] or musculoskeletal tumors [139], was also included in the selection of different imaging diagnostic protocols. These three protocols were chosen, in order to evaluate the hybrid-device developed in the present thesis as solution for radiation protection in the medical setting.

The hybrid-device shows a very fast response under the diagnostic protocol for skull imaging, as shown in Figure 4.16. For the selected protocol, the exposure time was 4 s, while the relaxation time was defined automatically by the controller of the CT-scanner. Within the exposure time, the SAW signal shows an attenuation of approximately 0.08 dB for each round of irradiation, but an absence of full recovery of the initial amplitude value during the involved relaxation time, which was obviously not long enough. A similar behaviour was observed for the pancreatic diagnostic protocol, as shown in Figure 4.17. The significant difference compared to the previous imaging protocol is the higher tube current of 260 mA against 200 mA, as well as the exposure time of 1.52 s against 4 s. The response of the hybrid-device is instantaneous to the short exposure time, with the attenuation of the SAW signal to be approximately 0.05 dB for each irradiation round.

Radiation-induced SAW signal attenuation was observed for the diagnostic imaging protocol of knee, likewise to the previous CT-scanning protocols, as shown in Figure 4.18. As the imaging protocol requires less tube current (50 mA) in comparison to the radiological examinations for skull (200 mA) and pancreas (260 mA), the dose-rate would be significantly less, resulting

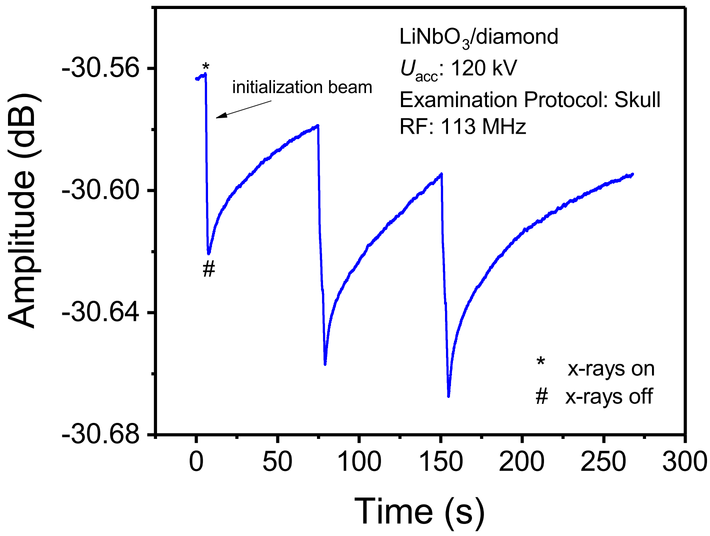

Figure 4.16: Radiation-induced response of the hybrid-device developed in this thesis, during exposure to a CT-scanner using an examination protocol typical for skull imaging. The first attenuation corresponds to the initialization beam of the CT-scanner, prior start of the diagnostic protocol. The asterisk symbol indicates the start of irradiation, while the hash symbol corresponds to the termination of irradiation.

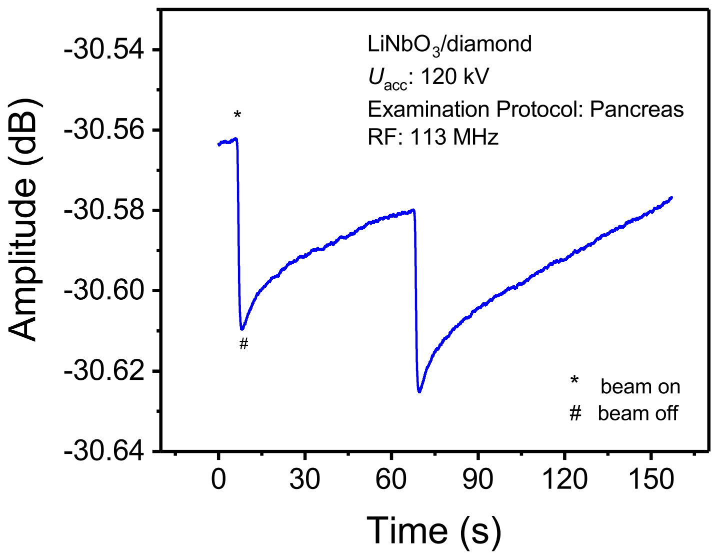

Figure 4.17: Radiation-induced response of the hybrid-device developed in this thesis, during exposure to a CT-scanner using an examination protocol for pancreas imaging. The asterisk symbol indicates the start of irradiation, while the hash symbol corresponds to the termination of irradiation.

in the reduction of SAW signal attenuation. Even though that the exposure time is only 1 s, the device shows a clear response at both irradiation rounds of approximately 0.02 dB.

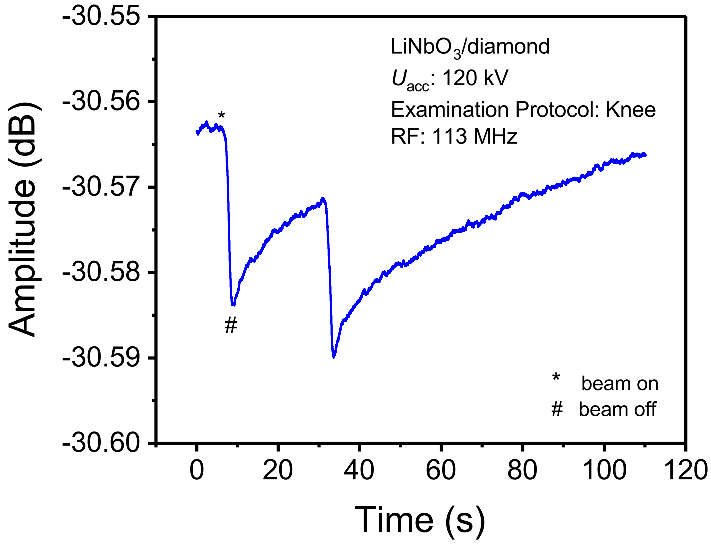

FIGURE 4.18: Radiation-induced response of the hybrid-device developed in this thesis, during exposure to a CT-scanner using an examination protocol for knee imaging. The asterisk symbol indicates the start of irradiation, while the hash symbol corresponds to the termination of irradiation.

From Figures 4.16, 4.17 and 4.18, it can deduced that the hybrid-device shows radiation-induced attenuation, when irradiated using diagnostic protocols, even for very short exposure times.

Conclusion 5

In this work, the development of two novel devices for the detection of low-energy ionizing radiation was pursued; an AlGaN/GaN-HEMT device and a device based on $LiNbO_3$-based SAW delay-line combined with a high-gain synthetic diamond layer. Prototypes of these two devices were fabricated independently at different locations, while they were successfully characterized at the radiation facilities, in terms of performance under low-energy ionizing radiation typically encountered in medical applications.

The AlGaN/GaN-HEMT device was fabricated with the method of photolithography in industrial clean-room environment and characterized by assessing its electrical properties under low-power x-rays. In the absence of exposure to x-rays and for gate voltages below -38 V, the I-V curves of the device demonstrated an exceptional stability of HEMT under low-energy irradiation, thus keeping the source-drain current to zero. The results revealed an extended voltage region from -80 V up to -38 V where the transistor can be operated in normally-off mode, hence suggesting the selection of -50 V as reference gate-voltage value. The suitability of the HEMT as ionizing radiation detector was tested by measuring the source-drain current during exposure to various dose-rates of radiation qualities N40 and N60. It was demonstrated that the HEMT sensor response was linear with dose-rate and reacted promptly in presence of incident x-ray beam. These characteristics were found to be in agreement with the literature. However, as the response of the HEMT detector was rather small and within only a few pA, it had to be concluded that this approach is not promising to be used for radiation detection applications. Specifically, this radiation detection system is considered far less sensitive to radiation-induce changes than already reported systems. As the fabrication of HEMT detectors had followed all the industry standards in terms of quality, and considering the excellent electrical characteristics of the fabricated HEMTs, it is concluded that further investigations of the correlation between material purities and radiation-induced response should be taken into consideration. It is noted that the presence of defects and impurities in materials has an impact on the formation of energy levels in the band-gap, thus affecting their capability of trapping electrons, which will result in the increase of detection sensitivity. For the future, it is advised to investigate this approach by varying the levels of defects and impurities of wafer-materials, in order to modify the energy levels of each layer and increase the detection of photons from the incident radiation beam.

In the second part, the use of a $LiNbO_3$-based SAW delay-line combined with a high-gain synthetic diamond layer as radiation detector was explored. The delay-line was fabricated with the method of photolithography in an academic clean-room environment, while the high-gain synthetic diamond was developed in an academic environment using the method of hetero-epitaxy. Moreover, the final hybrid-device was also assembled in an academic clean-room environment, with precautions to prevent contact between the diamond surface and the IDTs of the delay-line. The hybrid-device was initially characterized by employing a vector network analyzer for frequency domain characterization, where it was required that the fundamental frequency of the incorporated Split-4 IDTs correspond to 113.00 MHz. This frequency was kept constant throughout the characterization of the device under low-energy x-ray ionizing radiation. From the radiation experiments using a radiation quality of C60 with 3.9 mm Al filtration, as well as using a ^{137}Cs gamma-ray source, it was demonstrated that this hybrid structure can detect radiation-induced changes of conductivity that occur in the layer of the synthetic diamond. This was accomplished by measuring the attenuation of SAW signals at various dose-rates. Investigation at much higher dose-rates and energies could decrease the time for radiation-induced conductivity equilibrium, reducing the long time constant of the SAW that was observed at low dose-rates. Additional experiments employing medical radiological equipment for imaging purposes such as C-arm and CT-scanner, have demonstrated excellent performance for real medical fields and examination protocols. The detector exhibits instantaneous response, thus allowing the structure to generate the necessary response even for short duration of exposure time. Hence, such hybrid-device can be employed in wide range of departments within hospitals and clinics, for radiation protection of personnel and patients. The advantages of SAW circuit in terms of possible wireless readout and self-powered operation, classify this hybrid approach as well promising for the development of small-sized, low cost and durable radiation detectors for low-energy x-ray fields typical for medical applications.

Appendix

Interaction of Photons with Matter

The interaction of photons with matter is primarily taking place in the following three ways:

Photoelectric Effect: Absorption of photons by interaction with atomic electrons.

Compton Scattering: Photon scattering from an atomic electron.

Pair Production: Conversion of a photon into an electron-positron pair.

These mechanisms occur at different energy regions with the interaction cross sections depending on the exposed materials [6]. We can identify the dominating effects through the examination of the absorption coefficient (Figure 1) of a photon beam as it goes through the material [140]. As it can be seen, the photoelectric effect contributes most to photon interaction in the low energy range, in contrast to pair production that becomes dominant at high energies. Moreover, Compton scattering becomes the most probable interaction in the middle energy range.

In the following subsections, a more detailed description of the dominant photon interaction mechanisms will be given to better understand the theoretical background of radiation interaction with matter.

Photoelectric Effect

Having its origins in the wave-particle duality of electromagnetic waves early in the 20th century with Planck's and Einstein's theories [141], the photoelectric effect is an undergoing interaction of a photon with an absorber atom and the emission by the atom of an energetic photo-electron [15]. This emission predominantly takes place in the K atomic shell [6]. Depending on the target material, when the energy is lower than a threshold value it is not possible to eject electrons. Einstein explained this non classical effect, after having considered that electromagnetic waves can be considered as particles with an energy of

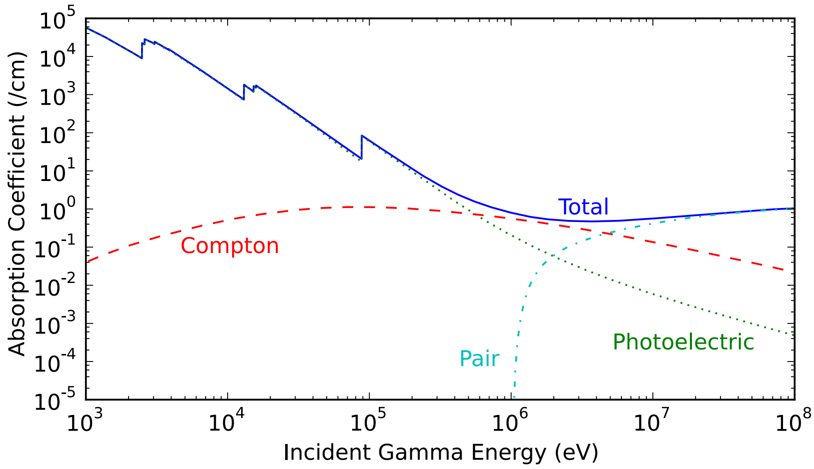

Figure 1: Example of absorption coefficients for a photon crossing lead (Pb) from Ref. [140].

$$E_\gamma = hf = \frac{hc}{\lambda} \tag{5.1}$$

where E_γ is the photon energy, f is the frequency and λ is the wavelength of electromagnetic waves, while c is the speed of light in vacuum. In order for the electrons to escape the electromagnetic force that keeps them bound to an atom, it is required to transfer an energy to the electron that is greater as or equal to the binding energy E_b. A graphical depiction of the photoelectric effect is shown in Figure 2. Mathematically speaking, the photoelectron appears when the $E_\gamma \geq E_b$ with energy

$$E_e = E_\gamma - E_b. \tag{5.2}$$

The photoelectric effect is the predominant interaction on the K atomic shell, as well as the most probable interaction for γ-rays of more than a few hundred keV [15]. Among the other cross section interactions, the photoelectric effects shows a strong atomic number Z dependence to be expressed as

$$\sigma_{pe} \propto \frac{Z^n}{E_\gamma^{3.5}} \tag{5.3}$$

where σ_{pe} is the corresponding cross section and the exponent n lies between the value of 4 and 5 [6][15]. From Relation 5.3 it can be extracted that the probability of the photoelectric absorption is high for materials of high atomic number, thus explaining the predominance of high atomic number materials for radiation shielding applications [15]. As a result of the photoelectric interaction it is possible during the emission of X-ray photon

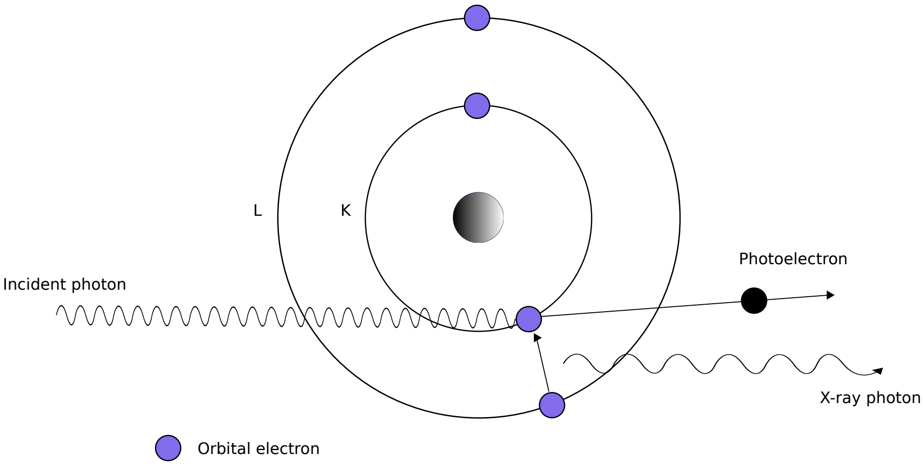

FIGURE 2: Illustration of the photoelectric effect in a free atom. If the incident photon knocks off an electron in the K-shell, a higher energy level electron fills the resulting vacancy, resulting in the emission of an X-ray photon [6].

the energy of this particular photon to be equal to the binding energy of an electron and get triggered to be emitted as Auger electron as shown in Figure 3. In that case, when a K-shell electron gets knocked off by an incident photon, it creates a vacancy that has to be filled to prevail the stability of the atom. When an electron from M-shell fills the created vacancy, it is possible for the release energy to excite another electron from M-shell in a radiationless electron emission [6].

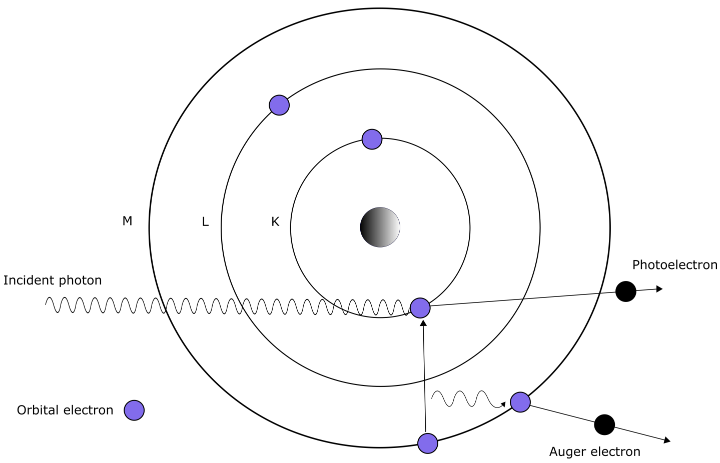

FIGURE 3: Schematic description of photoelectric effect resulting the emission of Auger electron [6].

Compton Scattering

This type of interaction is dominant for energy ranges between 0.1 and 10 MeV [92]. It typically occurs between the incident photon and an orbiting electron, where the first is deflected through an angle θ and the latter is kicked out of the atomic shell as result of partial energy transfer from the incident photon [15]. The scattered electron becomes an ionizining beta particle with scattering angle of ϕ, with respect to the energy and momentum conservation of the incident photon [15]. The above process for a bound electron is presented in Figure 4:

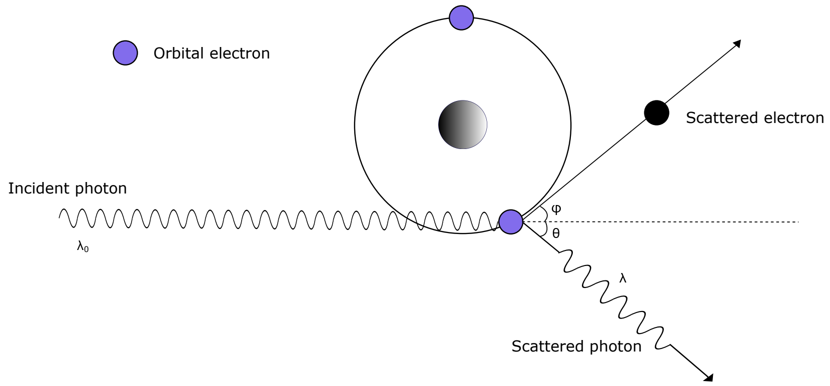

Figure 4: Illustration of Compton scattering [6].

As the scattered photon has lost some of its energy it is expected to have longer wavelength. The relation between wavelengths of incident and scattered photons is

$$\lambda = \lambda_0 + \frac{h}{m_0 c}(1 - \cos\theta) \tag{5.4}$$

were λ_0 and λ correspond the wavelengths of incident and scattered photons respectively, while m_0 represents the rest energy of the electron and θ the angle between scattered and incident photons.

When the energy of an incident photon is higher than the binding energy of the electron in the innermost shell, Compton interaction is more probable than the photoelectric effect. Furthermore, the increment of atomic number Z increases the probability of Compton scattering, as there are more available electrons that could serve as scattering targets [15].

Pair Production

Pair production is the process that results in the production of an electron-positron pair from an incident photon in the vicinity of an atomic nucleus and its Coulomb field [6], as is shown in Figure 5. This interaction is energetically feasible when the energy of the incident photon is greater than 1.02 MeV, double the rest-mass energy of an electron. As the incoming energy is shared among two particles with mass, there should be enough energy available for the process. All the excess energy of the incoming photon is shared by the produced electron and positron as kinetic energy [15].

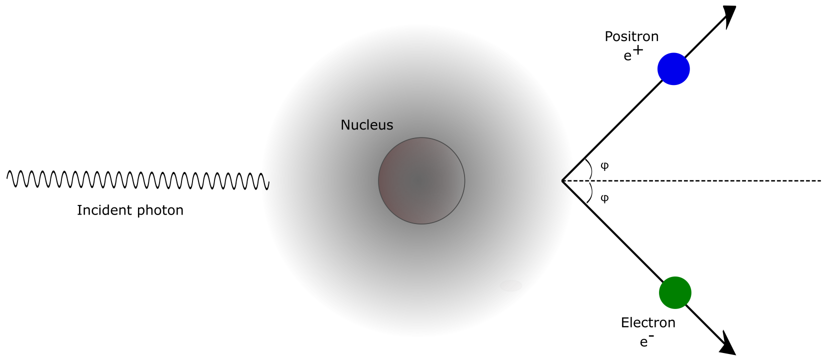

FIGURE 5: Schematic overview of pair production interaction.

The process of pair-production in the vicinity of the Coulomb field of the nucleus could be represented as

$$\gamma + X \rightarrow e^{-} + e^{+} + X^{*} \tag{5.5}$$

where X and X^{*} correspond to the ground and excited states of the nucleus, respectively [6]. Even though a simple expression describing the probability of pair production does not exist, its magnitude depends approximately on the square of the absorbing material's atomic number [15].

Concluding this section, the dependence of photoelectric effect, Compton scattering, and pair production, on atomic number Z and photon energy is presented in Figure 6. In the figure, lines indicate equal probability of neighbouring interactions. The curve at the left constitutes the energy at which Compton scattering and photoelectric effect have equal probability, while the curve of the right represents the relevant energy for equal probability between Compton scattering and pair production.

X-ray Attenuation

The three interactions presented in the previous subsections, occur according to the physical properties of the incoming photons and the absorbing material. When photon beams penetrate any material, the photoelectric effect, Compton scattering or pair production remove the photons from the incident beam either by absorption or by scattering [143]. This process can be expressed by summing the probability of the three main interactions, according to the thickness of the absorbing material. This sum is called *linear attenuation coefficient* and is expressed as follows;

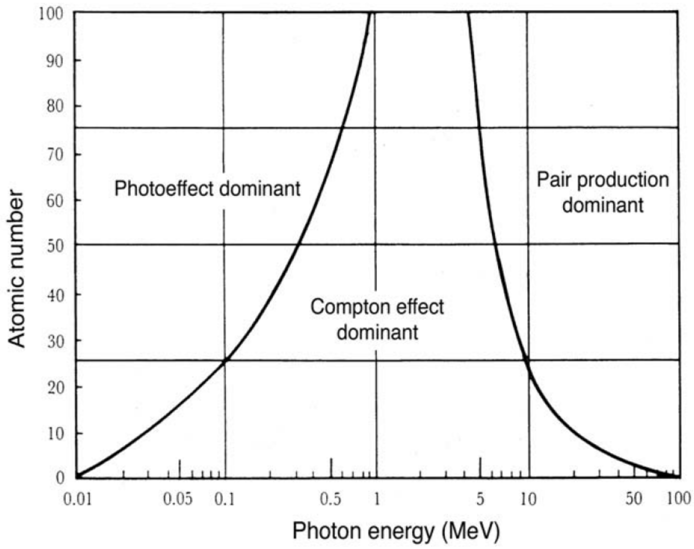

Figure 6: Regions of the three dominant interactions of photons with matter, for different atomic numbers and photon energies [142].

$$\mu_{total} = \sigma_{photoelectric} + \sigma_{Compton} + \sigma_{pair}. \tag{5.6}$$

If one considers a narrow beam of non-interacting photons with constant energy and with incident intensity I_0 penetrating a material of thickness x and density ρ, then the intensity I at given depth x will be

$$\frac{I}{I_0} = e^{-\mu_{total} x}. \tag{5.7}$$

Another quantitative parameter that characterizes photon interaction with matter is the *mean free path*. This parameter is defined as the average distance a photon has travelled in the absorbed material before the interaction takes place [15];

$$\lambda_m = \frac{1}{\mu_{total}}. \tag{5.8}$$

The *linear attenuation coefficient* describes the attenuation rate of certain photon beam, while it penetrates through a given material. It is expected that the attenuation coefficient does not only depend on the photon beam energy but also on the type and density of the absorbing material [6]. In order to consider the contribution of these parameters, another related quantity is introduced, defined as *mass attenuation coefficient* by Equation (5.9) from Ref. [6] and [15]. The mass attenuation coefficient is independent of the physical state of the material, thus showing the same value for water in liquid or in vapor state [15].

$$\mu_m = \frac{\mu_{total}}{\rho} \tag{5.9}$$

Combining equation (5.9) and (5.7), and considering the contribution of material density to attenuation, one gets the final expression

$$\frac{I}{I_0} = e^{-(\mu_{total}/\rho)\rho x} \tag{5.10}$$

where the product ρx corresponds to the *mass thickness* of the absorbing material, determining the degree of attenuation by a given material [15].

Radiation Induced Conductivity

From what has been discussed so far, the interaction of ionizing radiation with matter is accompanied by several radiation-induced effects that impact the physical characteristics of the involved material. One of the effects that take place when ionizing radiation interacts with either an insulating or a semiconducting volume is the increase of electrical conductivity, called *radiation induced conductivity (RIC)* [144]. The expression of conductivity σ is given by Equation (5.11)

$$\sigma = \sum ne\mu \tag{5.11}$$

where n is the number of free electrons per cm^3, e corresponds to the electron charge and μ is the mobility. As energy is deposited in the material from incident ionizing radiation, there is an increase in the number of free electrons and consequently in the number of mobile carrier density $n_e(T)$ [145]. The radiation induced conductivity σ_{RIC} is additive to the dark current (dc) conductivity of the specific material, as shown in Equation (5.12) [146].

$$\sigma_{total} = \sigma_{dc} + \sigma_{RIC} \tag{5.12}$$

The first RIC models were developed back to 1951 regarding insulating crystals and semiconductors [147], with further extension of the models for polymers in the subsequent years [144][148].

The process of RIC is described with the help of Figure 7 as follows: When an electron is excited into the conduction levels due to an incident radiation beam, it either becomes temporarily trapped. Then it may be thermally released into the conduction levels or recombines with an electron hole [132]. The effects of trapping and release might occur several times before the final capture of the electron by a very deep bound state. An electron in such a state has a higher probability for recombination with a free electron hole then being thermally excited [132]. It was reported that the effect of direct recombination becomes dominant at very high densities

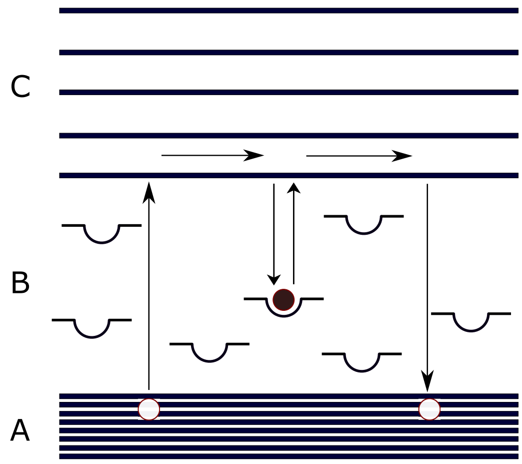

Figure 7: Example of energy level diagram for groups of atoms in insulating materials, with vertical representation of energy and horizontal representation of distance. Capital letters correspond as follows; (A) normally full levels, (B) normally forbidden levels, combined with metastable trapping levels and (C) normally empty conduction levels.

of both signs of carriers. Furthermore, impurities in crystal structure of the material define the physical properties of traps (region B in Figure 7) with the latter to be defined as metastable states where the electron does not have the freedom to move [132].

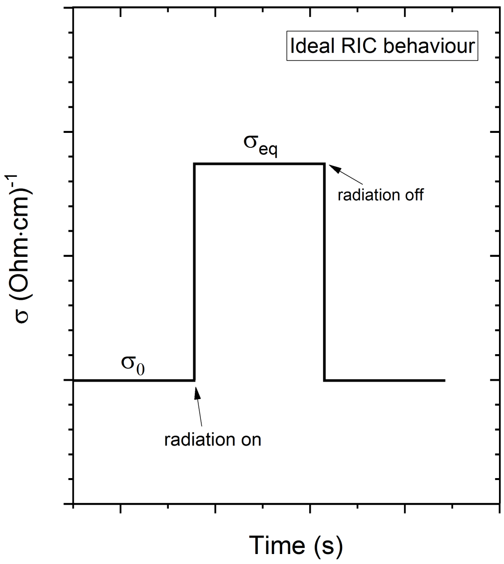

Figure 8: Ideal RIC behaviour model, revealing an immediate increase and decrease of conductivity with incident radiation.

The most important consequence of the existence of such traps is the reduction of the lifetime of electrons in the conduction levels (region C in

Figure 7). The lifetime of electrons is mathematically expressed as *conduction time*, τ_c, through Equation 5.13

$$\tau_c = \frac{1}{\upsilon q(m+n)} \tag{5.13}$$

where υ corresponds to the velocity of an electron, q is equivalent to the capture cross section of an electron, n expresses the number of electrons in conduction levels and m equals to the number of trapped electrons [132].

According to the physical model suggested by Fowler [132], the response time τ_0 of radiation induced conductivity is associated with the conduction time τ_c and the ratio of trapped electrons in the conductive region according to

$$\tau_0 = \tau_c \times m/n. \tag{5.14}$$

As it can be derived, the equilibrium value of radiation induced conductivity of any particular material will be function of dose rate. The idealized model of RIC behaviour for the case when an incident ionizing radiation beam is turned on, should describe an instantaneous increase of total conductivity from the dark current conductivity σ_{dc} of Equation 5.12 to the equilibrium conductivity that will correspond to total conductivity σ_{total} of Equation 5.12, as shown in Figure 8. Similarly, when the radiation beam is turned off the reverse effect takes place, reducing the conductivity of the particular material system to the initial σ_{dc}.

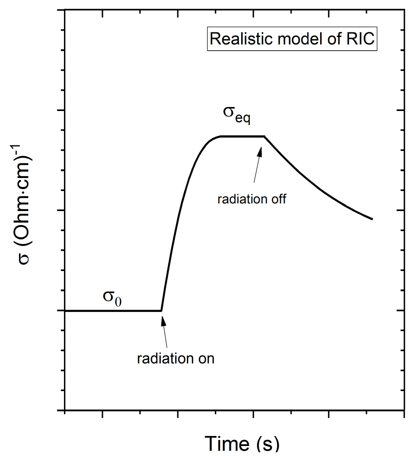

Figure 9: Realistic RIC behaviour model, exhibiting some time for the measured current to reach equilibrium, expressed as σ_{eq}, in presence or absence of ionizing radiation.

As a matter of fact, it takes a finite period of time for the conductivity to reach the equilibrium state after exposure to an incident ionizing radiation beam as well as to decay afterwards, as shown in Figure 9. Various suggested models were reported, correlating the dependence of hyperbolic decay of conductivity with the magnitude of total dose and the dose rate of incident ionizing radiation beam or exclusively with the dose rate [146].

References

[1] J. Sparenborg, C. Yingling, R. Hankins, *et al.*, “Determining Fluoroscopic Radiation Exposure to the Urology Resident,” *OMICS Journal of Radiology*, vol. 5, p. 215, January 2016.

[2] S. Ko, S. Kang, M. Ha, J. Kim, J. K. Jun, K. A. Kong, and W. J. Lee, “Health Effects from Occupational Radiation Exposure among Fluoroscopy-Guided Interventional Medical Workers: A Systematic Review,” *Journal of Vascular and Interventional Radiology*, vol. 29, no. 3, pp. 353–366, 2018.

[3] K. P. Kim, D. L. Miller, A. B. de Gonzalez, S. Balter, R. A. Kleinerman, E. Ostroumova, S. L. Simon, and M. S. Linet, “Occupational radiation doses to operators performing fluoroscopically-guided procedures,” *Health Physics*, vol. 103, no. 1, p. 80, 2012.

[4] H. Lim, M. S. Linet, M. E. Van Dyke, D. L. Miller, S. L. Simon, A. J. Sigurdson, and C. M. Kitahara, “Changing Patterns in the Performance of Fluoroscopically Guided Interventional Procedures and Adherence to Radiation Safety Practices in a US Cohort of Radiologic Technologists,” *American Journal of Roentgenology*, vol. 207, no. 6, pp. 1350–1359, 2016.

[5] A.-J. Garcia-Sanchez, E. A. Garcia Angosto, P. A. Moreno Riquelme, A. Serna Berna, and D. Ramos-Amores, “Ionizing Radiation Measurement Solution in a Hospital Environment,” *Sensors*, vol. 18, no. 2, p. 510, 2018.

[6] S. N. Ahmed, *Physics and Engineering of Radiation Detection*. Elsevier, 2nd ed., 2015.

[7] M. Jiang, H. Xiao, S. Peng, G. Yang, Z. Liu, and X. Zu, “A Comparative Study of low energy radiation response of AlAs, GaAs and GaAs/AlAs superlattice and the damage effects on their electronic structures,” *Scientific Reports*, vol. 8, no. 1, p. 2012, 2018.

[8] J. Wang, P. Mulligan, L. Brillson, and L. R. Cao, “Review of using gallium nitride for ionizing radiation detection,” *Applied Physics Reviews*, vol. 2, no. 3, p. 031102, 2015.

[9] M. Piliero, R. Hugtenburg, S. Ryde, and K. Oliver, "Development of CVD diamond detectors for clinical dosimetry," *Radiation Physics and Chemistry*, vol. 104, pp. 10–14, 2014.

[10] J. Damodar, D. Odgers, D. Pope, and R. Hill, "A study on the suitability of the PTW microDiamond detector for kilovoltage x-ray beam dosimetry," *Applied Radiation and Isotopes*, vol. 135, pp. 104–109, 2018.

[11] J. Howgate, M. Hofstetter, S. Schoell, M. Schmid, S. Schäfer, I. Zizak, V. Hable, C. Greubel, G. Dollinger, S. Thalhammer, *et al.*, "Ultrahigh gain AlGaN/GaN high energy radiation detectors," *Physica Status Solidi (A) Application and Materials*, vol. 209, no. 8, pp. 1562–1567, 2012.

[12] M. Schmid, J. Howgate, W. Ruehm, and S. Thalhammer, "High mobility AlGaN/GaN devices for β–dosimetry," *Nuclear Instruments and Methods in Physics Research Section A: Accelerators, Spectrometers, Detectors and Associated Equipment*, vol. 819, pp. 14–19, 2016.

[13] T. Cramer, I. Fratelli, P. Barquinha, A. Santa, C. Fernandes, F. D'Annunzio, C. Loussert, R. Martins, E. Fortunato, and B. Fraboni, "Passive radiofrequency x-ray dosimeter tag based on flexible radiation-sensitive oxide field-effect transistor," *Science Advances*, vol. 4, no. 6, p. eaat1825, 2018.

[14] J. Seco, B. Clasie, and M. Partridge, "Review on the characteristics of radiation detectors for dosimetry and imaging," *Physics in Medicine & Biology*, vol. 59, no. 20, p. R303, 2014.

[15] G. F. Knoll, *Radiation Detection and Measurement*. New York: Wiley, 3rd ed., 2000.

[16] D. Ehrentraut, E. Meissner, and M. Bockowski, *Technology of Gallium Nitride Crystal Growth*, vol. 133 of *Springer Series in Materials Science*. Heidelberg: Springer, 2010.

[17] S. Pearton, F. Ren, E. Patrick, M. Law, and A. Y. Polyakov, "Review-Ionizing Radiation Damage Effects on GaN Devices," *ECS Journal of Solid State Science and Technology*, vol. 5, no. 2, pp. Q35–Q60, 2016.

[18] P. Bergonzo, D. Tromson, and C. Mer, "Radiation detection devices made from CVD diamond," *Semiconductor science and technology*, vol. 18, no. 3, p. S105, 2003.

[19] M. Bucciolini, C. De Angelis, and C. Talamonti, *Comprehensive Biomedical Physics*, ch. Diamond Detectors for Dosimetry, pp. 229–248. Elsevier, 2014.

[20] M. Girolami, A. Bellucci, P. Calvani, and D. M. Trucchi, “Large single-crystal diamond substrates for ionizing radiation detection,” *Physica Status Solidi (A) Application and Materials*, vol. 213, no. 10, pp. 2634–2640, 2016.

[21] K. B. Pfeifer, A. N. Rumpf, W. G. Yelton, and S. J. Limmer, “Wireless Passive Radiation Sensor,” Dec. 3 2013. US Patent 8,596,862.

[22] W. C. Wilson and G. M. Atkinson, “Passive Wireless Sensor Applications for NASA’s Extreme Aeronautical Environments,” *IEEE Sens. J*, vol. 14, no. 11, pp. 3745–3753, 2014.

[23] F.-D. Lai and H. Huang, “Fabrication of high frequency and low-cost surface-acoustic wave filters using near field phase shift photolithography,” *Microelectronic Engineering*, vol. 83, no. 4-9, pp. 1407–1409, 2006.

[24] M. E. Morales-Rodriguez, P. C. Joshi, J. R. Humphries, P. L. Fuhr, and T. J. Mcintyre, “Fabrication of Low Cost Surface Acoustic Wave Sensors Using Direct Printing by Aerosol Inkjet,” *IEEE Access*, vol. 6, pp. 20907–20915, 2018.

[25] H. Krenner, D. Fuhrmann, S. Völk, F. Schülein, F. Knall, J. Ebbecke, and A. Wixforth, “Surface acoustic wave hybrid devices: High sensitivity conductivity probes and low-jitter single photon sources,” in *Proceedings SENSOR 2013*, pp. 117 – 120, 2013.

[26] N. Berg and J. Speulstra, “The Operation of Acoustic Surface Wave Delay Lines in a Nuclear Environment,” *IEEE Transactions on Nuclear Science*, vol. 20, no. 6, pp. 137–143, 1973.

[27] A. Wixforth, *Wechselwirkung Akustischer Oberflächenwellen mit einem Zweidimensionalen Elektronensystem*. PhD thesis, Universität Hamburg, 1987.

[28] A. Wixforth, J. Scriba, M. Wassermeier, J. Kotthaus, G. Weimann, and W. Schlapp, “Interaction of surface acoustic waves with a two-dimensional electron system in a $LiNbO_3$-GaAs/AlGaAs sandwich structure,” *Journal of Applied Physics*, vol. 64, no. 4, pp. 2213–2215, 1988.

[29] A. Wixforth, J. Scriba, M. Wassermeier, J. Kotthaus, G. Weimann, and W. Schlapp, “Surface acoustic waves on GaAs/AlxGa(1-x)As heterostructures,” *Physical Review B*, vol. 40, no. 11, p. 7874, 1989.

[30] A. Hernández-Mínguez, Y. Liou, and P. Santos, “Interaction of surface acoustic waves with electronic excitations in graphene,” *Journal of Physics D: Applied Physics*, vol. 51, no. 38, p. 383001, 2018.

[31] C. Mack, *Fundamental Principles of Optical Lithography: The Science of Microfabrication.* Wiley, 2007.

[32] J. Howgate, *GaN Heterostructures for Biosensing and Radiation Detection.* PhD thesis, Technische Universität München, 2012.

[33] S. Gsell, T. Bauer, J. Goldfuß, M. Schreck, and B. Stritzker, "A route to diamond wafers by epitaxial deposition on silicon via iridium/yttria-stabilized zirconia buffer layers," *Applied Physics Letters*, vol. 84, no. 22, pp. 4541–4543, 2004.

[34] S. Gsell, M. Fischer, T. Bauer, M. Schreck, and B. Stritzker, "Yttria-stabilized zirconia films of different composition as buffer layers for the deposition of epitaxial diamond/Ir layers on Si (001)," *Diamond and Related Materials*, vol. 15, no. 4-8, pp. 479–485, 2006.

[35] M. Fischer, S. Gsell, M. Schreck, R. Brescia, and B. Stritzker, "Preparation of 4-inch Ir/YSZ/Si (001) substrates for the large-area deposition of single-crystal diamond," *Diamond and Related Materials*, vol. 17, no. 7-10, pp. 1035–1038, 2008.

[36] J. H. Edgar, *Properties of Group III Nitrides.* EMIS Datareviews Series No. 11, Institution of Electrical Engineers, 1994.

[37] F. K. Yam, L. L. Low, S. A. Oh, and Z. Hassan, "Gallium Nitride: An Overview of Structural Defects," in *Optoelectronics-Materials and Techniques*, InTech, 2011.

[38] A. Stocco, *Reliability and failure mechanisms of GaN HEMT devices suitable for high-frequency and high-power applications.* PhD thesis, Università degli Studi di Padova, 2012.

[39] O. Ambacher, J. Smart, J. Shealy, N. Weimann, K. Chu, M. Murphy, W. Schaff, L. Eastman, R. Dimitrov, L. Wittmer, *et al.*, "Two-dimensional electron gases induced by spontaneous and piezoelectric polarization charges in N-and Ga-face AlGaN/GaN heterostructures," *Journal of Applied Physics*, vol. 85, no. 6, pp. 3222–3233, 1999.

[40] A. Lidow, J. Strydom, M. De Rooij, and D. Reusch, *GaN Transistors for Efficient Power Conversion.* John Wiley & Sons, 2014.

[41] U. K. Mishra, L. Shen, T. E. Kazior, and Y.-F. Wu, "GaN-Based RF Power Devices and Amplifiers," *Proceedings of the IEEE*, vol. 96, no. 2, pp. 287–305, 2008.

[42] T. J. Anderson, M. J. Tadjer, J. K. Hite, J. D. Greenlee, A. D. Koehler, K. D. Hobart, and F. J. Kub, "Effect of reduced extended defect

density in MOCVD grown AlGaN/GaN HEMTs on native GaN substrates," *IEEE Electron Device Letters*, vol. 37, no. 1, pp. 28–30, 2016.

[43] S. L. Zhao, B. Hou, W. W. Chen, M. H. Mi, J. X. Zheng, J. C. Zhang, X. H. Ma, and Y. Hao, "Analysis of the Breakdown Characterization Method in GaN-Based HEMTs," *IEEE Transactions on Power Electronics*, vol. 31, no. 2, pp. 1517–1527, 2016.

[44] J. Biscarrat, R. Gwoziecki, Y. Baines, J. Buckley, C. Gillot, W. Vandendaele, G. Garnier, M. Charles, and M. Plissonnier, "Performance enhancement of CMOS compatible 600 V rated AlGaN/GaN Schottky diodes on 200 mm silicon wafers," in *2018 IEEE 30th International Symposium on Power Semiconductor Devices and ICs (ISPSD)*, pp. 200–203, IEEE, 2018.

[45] M. Hiroki, K. Kumakura, and H. Yamamoto, "Efficient heat dissipation in AlGaN/GaN high electron mobility transistors by substrate-transfer technique," *Physica Status Solidi (A) Application and Materials*, vol. 214, no. 8, 2017.

[46] R. Quay, D. Schwantuschke, E. Ture, F. van Raay, C. Friesicke, S. Krause, S. Müller, S. Breuer, B. Godejohann, and P. Brückner, "High-Power Microwave GaN/AlGaN HEMTs and MMICs on SiC and Silicon Substrates for Modern Radio Communication," *Physica Status Solidi (A) Application and Materials*, vol. 215, no. 9, p. 1700655, 2018.

[47] A. Fontserè, A. Pérez-Tomás, M. Placidi, N. Baron, S. Chenot, J. Moreno, and Y. Cordier, "Bulk temperature impact on the AlGaN/GaN HEMT forward current on Si, Sapphire and free-standing GaN," *ECS Solid State Letters*, vol. 2, no. 1, pp. P4–P7, 2013.

[48] F. Medjdoub, J. Carlin, C. Gaquiere, N. Grandjean, and E. Kohn, "Status of the Emerging InAlN/GaN Power HEMT Technology," *Open Electrical & Electronic Engineering Journal*, vol. 2, pp. 1–7, 2008.

[49] S. Hamady, *New concepts for normally-off power gallium nitride (GaN) high electron mobility transistor (HEMT).* PhD thesis, Universite Toulouse III Paul Sabatier, 2014.

[50] R. Dimitrov, M. Murphy, J. Smart, W. Schaff, J. Shealy, L. Eastman, O. Ambacher, and M. Stutzmann, "Two-dimensional electron gases in Ga-face and N-face AlGaN/GaN heterostructures grown by plasma-induced molecular beam epitaxy and metalorganic chemical vapor deposition on sapphire," *Journal of Applied Physics*, vol. 87, no. 7, pp. 3375–3380, 2000.

[51] E. Patrick, M. Choudhury, F. Ren, S. J. Pearton, and M. E. Law, "Simulation of Radiation Effects in AlGaN/GaN HEMTs," *ECS Transactions*, vol. 66, no. 1, pp. 21–31, 2015.

[52] J.-Y. Duboz, M. Laügt, D. Schenk, B. Beaumont, J.-L. Reverchon, A. D. Wieck, and T. Zimmerling, "GaN for x-ray detection," *Applied Physics Letters*, vol. 92, no. 26, p. 263501, 2008.

[53] M. Hofstetter, J. Howgate, I. D. Sharp, M. Stutzmann, and S. Thalhammer, "Development and evaluation of gallium nitride-based thin films for x-ray dosimetry," *Physics in Medicine & Biology*, vol. 56, no. 11, p. 3215, 2011.

[54] K. Nordlund, M. Ghaly, R. Averback, M. Caturla, T. D. de La Rubia, and J. Tarus, "Defect production in collision cascades in elemental semiconductors and fcc metals," *Physical Review B*, vol. 57, no. 13, p. 7556, 1998.

[55] M. Ohring, *Reliability and Failure of Electronic Materials and Devices*. San Diego: Academic Press, 1998.

[56] A. Ionascut-Nedelcescu, C. Carlone, A. Houdayer, H. Von Bardeleben, J.-L. Cantin, and S. Raymond, "Radiation hardness of gallium nitride," *IEEE Transactions on Nuclear Science*, vol. 49, no. 6, pp. 2733–2738, 2002.

[57] J. Chen, "Radiation Response and Reliability of AlGaN/GaN HEMTs," Master's thesis, Vanderbilt University, August 2013.

[58] S. J. Sque, *A First-Principles Study on Bulk and Transfer Doping of Diamond*. PhD thesis, University of Exeter, April 2007.

[59] S. Koizumi, C. Nebel, and M. Nesladek, *Physics and Applications of CVD Diamond*. Wiley-VCH Verlag GmbH & Co. KGaA, 2008.

[60] R. S. Sussmann, ed., *CVD Diamond for Electronic Devices and Sensors*. Materials for Electronic and Optoelectronic Applications, Chichester, U.K.: Wiley, 2009.

[61] F. P. Bundy, H. T. Hall, H. M. Strong, and R. H. Wentorf Jun, "Man-Made Diamonds," *Nature*, vol. 176, 1955.

[62] J. E. Butler, R. L. Woodin, L. M. Brown, and P. Fallon, "Thin-film Diamond Growth Mechanisms," *Philosophical Transactions of the Royal Society of London A: Mathematical, Physical and Engineering Sciences*, vol. 342, no. 1664, pp. 209–224, 1993.

[63] P. Bergonzo, D. Tromson, C. Mer, B. Guizard, F. Foulon, and A. Brambilla, "Particle and Radiation Detectors Based on Diamond," *Physica Status Solidi A*, vol. 185, no. 1, pp. 167–181, 2001.

[64] A. Galbiati, *Development of CVD Diamond Radiation Detectors*. PhD thesis, University of Surrey, September 2003.

[65] D. Kania, M. Landstrass, M. Plano, L. Pan, and S. Han, "Diamond radiation detectors," *Diamond and Related Materials*, vol. 2, no. 5-7, pp. 1012–1019, 1993.

[66] R. Tapper, "Diamond Detectors in Particle Physics," *Reports on Progress in Physics*, vol. 63, no. 8, p. 1273, 2000.

[67] G. T. Betzel, *Development of a Prototype Synthetic Diamond Detector for Radiotherapy Dosimetry*. PhD thesis, University of Canterbury, 2010.

[68] L. Black, *New Perspectives on Surface Passivation: Understanding the Si-AL2O3 Interface*. Springer Theses, Springer International Publishing, 2016.

[69] I. Volovichev, G. Logvinov, O. Y. Titov, and Y. G. Gurevich, "Recombination and lifetimes of charge carriers in semiconductors," *Journal of Applied Physics*, vol. 95, no. 8, pp. 4494–4496, 2004.

[70] L. Rayleigh, "On Waves Propagated along the Plane Surface of an Elastic Solid," *Proceedings of the London Mathematical Society*, vol. 1, no. 1, pp. 4–11, 1885.

[71] D. P. Morgan, "A History of Surface Acoustic Wave Devices," *International Journal of High Speed Electronics and Systems*, vol. 10, no. 03, pp. 553–602, 2000.

[72] R. White and F. Voltmer, "Direct Piezoelectric Coupling to Surface Elastic Waves," *Applied Physics Letters*, vol. 7, no. 12, pp. 314–316, 1965.

[73] D. B. Go, M. Z. Atashbar, Z. Ramshani, and H.-C. Chang, "Surface acoustic wave devices for chemical sensing and microfluidics: a review and perspective," *Analytical Methods*, vol. 9, no. 28, pp. 4112–4134, 2017.

[74] I. Voiculescu and A. N. Nordin, "Acoustic wave based MEMS devices for biosensing applications," *Biosensors and Bioelectronics*, vol. 33, no. 1, pp. 1–9, 2012.

[75] D. P. Morgan, *Surface Acoustic Wave Filters with Applications to Electronic Communications and Signal Processing.* Academic Press, 2nd ed., 2007.

[76] C. C. Park, *A Dictionary of Environment and Conservation.* Oxford Paperback Reference, Oxford University Press, 2008.

[77] M. Rotter, *Wechselwirkungen zwischen Oberflächenwellen und zweidimensionalen Elektronensystemen in $LiNbO_3$/GaAs-Schichtstrukturen.* PhD thesis, Ludwig-Maximilians-Universität München, 1999.

[78] W. P. Jakubik, "Surface acoustic wave-based gas sensors," *Thin Solid Films*, vol. 520, no. 3, pp. 986–993, 2011.

[79] D. A. Fleisch, *A Student's Guide to Maxwell's Equations.* Cambridge, UK: Cambridge University Press, 2008.

[80] C. Campbell, *Surface Acoustic Wave Devices and their Signal Processing Applications.* Boston: Academic Press, 1989.

[81] J. W. Gardner, V. K. Varadan, and O. O. Awadelkarim, *Microsensors, MEMS, and Smart Devices.* Chichester: J. Wiley, 2001.

[82] A. Reiner, "Untersuchung Quasizweidimensionaler Elektronensysteme mittels DC-Messungen und akustischer Oberflächenwelle," Master's thesis, Augsburg Universität, August 2014.

[83] N. Y. Kozlovski, *Passive Wireless SAW Sensors with New and Novel Reflector Structures: Design and Applications.* PhD thesis, University of Central Florida, 2011.

[84] A. Hutson and D. L. White, "Elastic Wave Propagation in Piezoelectric Semiconductors," *Journal of Applied Physics*, vol. 33, no. 1, pp. 40–47, 1962.

[85] L. Bandhu and G. R. Nash, "Controlling the properties of surface acoustic waves using graphene," *Nano Research*, vol. 9, no. 3, pp. 685–691, 2016.

[86] M. Hiebel, *Fundamental of Vector Network Analysis.* Rohde & Schwarz GmbH & Co. KG, 2005, fifth ed., 2011.

[87] A. Tilke, "Dynamik des quantisierten Hall Effektes: Absorption von akustischen Oberflächenwellen an AlSb/InAs/AlSb-Quantentöpfen," Master's thesis, Technische Universität München, 1996.

[88] M. R. Zakaria, M. A. F. Shamsuddin, U. Hashim, T. Adam, and A. W. Al-Mufti, "Design and Fabrication of IDT Surface Acoustic Wave Device For Biosensor Application," in *5th International Conference on Intelligent Systems, Modelling and Simulation (ISMS)*, pp. 760–764, IEEE, 2014.

[89] V. Bandalo, *Nanopore-cavity Devices for Characterization of Biological Systems*. PhD thesis, Technische Universität Carolo-Wilhelmina zu Braunschweig, 2015.

[90] S. Ahmadi, F. Hassani, C. Korman, M. Rahaman, and M. Zaghloul, "Characterization of multi- and single-layer structure SAW sensor [gas sensor]," in *Sensors, 2004. Proceedings of IEEE*, pp. 1129–1132, IEEE, 2004.

[91] S. Krishnamurthy, *Wireless Passive Surface Acoustic Wave (SAW) Sensing System*. PhD thesis, Western Michigan University, 2007.

[92] A. Ternawly, "Effect of Radiation on SAW Resonators," Master's thesis, McMaster University, 2007.

[93] W. Stapor, J. Hines, and D. Wilson, "Ionizing space radiation effects on surface acoustic wave resonators," *IEEE transactions on nuclear science*, vol. 38, no. 6, pp. 1329–1335, 1991.

[94] R. Velcheva, L. Spassov, Y. Filippov, E. Kulagin, and V. Miklayev, "Thermosensitive Quartz Crystal Resonators under Fast Neutrons and Gamma Rays," *Bulgarian Journal of Physics*, vol. 29, p. 30, 2003.

[95] I. Sayago, M. Fernández, J. Fontecha, M. Horrillo, C. Vera, I. Obieta, and I. Bustero, "New sensitive layers for surface acoustic wave gas sensors based on polymer and carbon nanotube composites," *Sensors and Actuators B: Chemical*, vol. 175, pp. 67–72, 2012.

[96] Q. Li, H. Liu, G. Li, F. Zeng, F. Pan, J. Luo, and L. Qian, "Growth and Characterization of Polyimide-Supported AlN Films for Flexible Surface Acoustic Wave Devices," *Journal of Electronic Materials*, vol. 45, no. 6, pp. 2702–2709, 2016.

[97] S. Tavernier, *Radiation Detectors for Medical Applications*. NATO Security Through Science, Springer, 2006.

[98] S. J. Crossley, "The suitability of active personal dosimeters as the legal dosimeter for PET radioisotope workers," Master's thesis, The University of Western Australia, September 2016.

[99] C. R. Hirning and P. S. Yuen, "Type testing of the Siemens Plessey electronic personal dosemeter.," *Health physics*, vol. 69, no. 1, pp. 46–66, 1995.

[100] J. Kahilainen, "The Direct Ion Storage Dosemeter," *Radiation Protection Dosimetry*, vol. 66, no. 1-4, pp. 459–462, 1996.

[101] H. Fuchs, S. Stähler, and M. Dittmar, "New data on direct ion storage dosemeters," *Radiation Protection Dosimetry*, vol. 128, no. 1, pp. 120–123, 2007.

[102] J. A. Crowhurst, G. M. Scalia, M. Whitby, D. Murdoch, B. J. Robinson, A. Turner, L. Johnston, S. Margale, S. Natani, A. Clarke, *et al.*, "Radiation Exposure of Operators Performing Transesophageal Echocardiography During Percutaneous Structural Cardiac Interventions," *Journal of the American College of Cardiology*, vol. 71, no. 11, pp. 1246–1254, 2018.

[103] M. Gårdestig and H. B. Pettersson, "Approved Personal Dosimetry for Medical Personnel using Direct Ion Storage Dosimeters," in *World Congress on Medical Physics and Biomedical Engineering, September 7-12, 2009, Munich, Germany*, pp. 352–354, Springer, 2009.

[104] "Commercial booklet of Instadose+ dosimeter by Mirion Technologies."

[105] "E-mail communication with Ferdinard-Braun-Institut," February 2015.

[106] K. I. Inc., *Model 2400 Series SourceMeter User's Manual*, May 2002.

[107] R. Tompkins, I. Mahaboob, F. Shahedipour-Sandvik, and N. Lazarus, "Electrical properties of AlGaN/GaN HEMTs in stretchable geometries," *Solid-State Electronics*, vol. 136, pp. 36–42, 2017.

[108] Z. H. Zaidi and P. A. Houston, "Highly sensitive UV detection mechanism in AlGaN/GaN HEMTs," *IEEE Transactions on Electron Devices*, vol. 60, no. 9, pp. 2776–2781, 2013.

[109] Y. Huang, D. Chen, H. Lu, H. Shi, P. Han, R. Zhang, and Y. Zheng, "Photocurrent characteristics of two-dimensional-electron-gas-based AlGaN/GaN metal-semiconductor-metal photodetectors," *Applied Physics Letters*, vol. 96, no. 24, p. 243503, 2010.

[110] A. Varghese, R. S. Livingstone, L. Varghese, S. Dey, J. Jose, V. S. Thomson, O. K. George, and P. V. George, "Radiation dose from percutaneous transluminal coronary angioplasty procedure performed

using a flat detector for different clinical angiographic projections," *Journal of Radiological Protection*, vol. 38, no. 2, p. 511, 2018.

[111] P. Kouyoumdjïan, G. Gras-Combe, M. Grelat, S. Fuentes, B. Blondel, P. Tropiano, F. Zairi, J. Beaurain, Y.-P. Charles, A. Dhenin, *et al.*, "Surgeon's and patient's radiation exposure during percutaneous thoraco-lumbar pedicle screw fixation: A prospective multicenter study of 100 cases," *Orthopaedics & Traumatology: Surgery & Research*, vol. 104, no. 5, pp. 597–602, 2018.

[112] F. J. Cabrera, R. H. Shin, K. M. Waisanen, G. Nguyen, C. Wang, C. D. Scales, M. N. Ferrandino, G. M. Preminger, T. T. Yoshizumi, and M. E. Lipkin, "Comparison of radiation Exposure from Fixed Table Fluoroscopy to a Portable C-Arm during Ureteroscopy," *Journal of Endourology*, vol. 31, no. 9, pp. 835–840, 2017.

[113] E. C. Beckmann, "CT Scanning the Early Days," *The British Journal of Radiology*, vol. 79, no. 937, pp. 5–8, 2006.

[114] A. Johnston, *Reliability and Radiation Effects in Compound Semiconductors*. World Scientific, 2010.

[115] A. Y. Polyakov, S. Pearton, P. Frenzer, F. Ren, L. Liu, and J. Kim, "Radiation effects in GaN materials and devices," *Journal of Materials Chemistry C*, vol. 1, no. 5, pp. 877–887, 2013.

[116] S. J. Pearton, R. Deist, F. Ren, L. Liu, A. Y. Polyakov, and J. Kim, "Review of radiation damage in GaN-based materials and devices," *Journal of Vacuum Science & Technology A: Vacuum, Surfaces, and Films*, vol. 31, no. 5, p. 050801, 2013.

[117] O. Aktas, A. Kuliev, V. Kumar, R. Schwindt, S. Toshkov, D. Costescu, J. Stubbins, and I. Adesida, "60Co gamma radiation effects on DC, RF, and pulsed I–V characteristics of AlGaN/GaN HEMTs," *Solid-State Electronics*, vol. 48, no. 3, pp. 471–475, 2004.

[118] D. M. Fleetwood, "Total Ionizing Dose Effects in MOS and Low-Dose-Rate-Sensitive Linear-Bipolar Devices," *IEEE Transactions on Nuclear Science*, vol. 60, no. 3, pp. 1706–1730, 2013.

[119] B. D. Milbrath, A. J. Peurrung, M. Bliss, and W. J. Weber, "Radiation Detector Materials: An Overview," *Journal of Materials Research*, vol. 23, no. 10, pp. 2561–2581, 2008.

[120] A. Mirzaei, J.-S. Huh, S. S. Kim, and H. W. Kim, "Room Temperature Hard Radiation Detectors Based on Solid State Compound Semiconductors: An Overview," *Electronic Materials Letters*, vol. 14, no. 3, pp. 261–287, 2018.

[121] P. Edmonson and W. D. Hunt, "Surface acoustic wave sensors: attributes and advantages," in *Radio and Wireless Conference, 2004 IEEE*, pp. 47–50, IEEE, 2004.

[122] L. Bo, C. Xiao, C. Hualin, M. A. Mohammad, T. Xiangguang, T. Luqi, Y. Yi, and R. Tianling, "Surface acoustic wave devices for sensor applications," *Journal of Semiconductors*, vol. 37, no. 2, p. 021001, 2016.

[123] C. Müller, A. Nateprov, G. Obermeier, M. Klemm, R. Tidecks, A. Wixforth, and S. Horn, "Surface acoustic wave investigations of the metal-to-insulator transition of V_2O_3 thin films on lithium niobate," *Journal of applied physics*, vol. 98, no. 8, p. 084111, 2005.

[124] R. Rimeika, D. Ciplys, M. Shur, R. Gaska, M. Khan, and J. Yang, "Electromechanical Coupling Coefficient for Surface Acoustic Waves in GaN-on-Sapphire," *Physica Status Solidi (B): Basic Solid State Physics*, vol. 234, no. 3, pp. 897–900, 2002.

[125] M. Rotter, A. Wixforth, W. Ruile, D. Bernklau, and H. Riechert, "Giant acoustoelectric effect in GaAs/$LiNbO_3$ hybrids," *Applied Physics Letters*, vol. 73, no. 15, pp. 2128–2130, 1998.

[126] M. Rotter, A. Wixforth, J. P. Kotthaus, W. Ruile, D. Bernklau, and H. Riechert, "Quasi-monolithic GaAs/LiNbO/sub 3/-hybrids for acoustoelectric applications," in *Ultrasonics Symposium, 1997. Proceedings., 1997 IEEE*, vol. 1, pp. 201–204, IEEE, 1997.

[127] R. Di Benedetto, M. Marinelli, G. Messina, E. Milani, E. Pace, A. Paoletti, A. Pini, S. Santangelo, S. Scuderi, A. Tucciarone, G. Verona-Rinati, and G. Bonanno, "Influence of metal–diamond interfaces on the response of uv photoconductors," *Diamond and Related Materials*, vol. 10, no. 3, pp. 698–705, 2001. 11th European Conference on Diamond, Diamond-like Materials, Carbon Nanotubes, Nitrides and Silicon Carbide.

[128] Z. Remes, R. Petersen, K. Haenen, M. Nesladek, and M. D'Olieslaeger, "Mechanism of photoconductivity in intrinsic epitaxial cvd diamond studied by photocurrent spectroscopy and photocurrent decay measurements," *Diamond and Related Materials*, vol. 14, no. 3, pp. 556–560, 2005. Proceedings of Diamond 2004, the 15th European Conference on Diamond, Diamond-Like Materials, Carbon Nanotubes, Nitrides and Silicon Carbide.

[129] A. Secroun, A. Tallaire, J. Achard, G. Civrac, H. Schneider, and A. Gicquel, "Photoconductive properties of lightly n-doped single

crystal cvd diamond films," *Diamond and Related Materials*, vol. 16, no. 4, pp. 953–957, 2007. Proceedings of Diamond 2006, the 17th European Conference on Diamond, Diamond-Like Materials, Carbon Nanotubes, Nitrides and Silicon Carbide.

[130] M. Liao, Y. Koide, J. Alvarez, M. Imura, and J.-P. Kleider, "Persistent positive and transient absolute negative photoconductivity observed in diamond photodetectors," *Phys. Rev. B*, vol. 78, p. 045112, Jul 2008.

[131] M. Schreck, P. Ščajev, M. Träger, M. Mayr, T. Grünwald, M. Fischer, and S. Gsell, "Charge carrier trapping by dislocations in single crystal diamond," *Journal of Applied Physics*, vol. 127, no. 12, p. 125102, 2020.

[132] J. F. Fowler, "Radiation-induced Conductivity in the Solid State, and Some Applications," *Physics in Medicine & Biology*, vol. 3, no. 4, p. 395, 1959.

[133] F. Marsolat, D. Tromson, N. Tranchant, M. Pomorski, D. Lazaro-Ponthus, C. Bassinet, C. Huet, S. Derreumaux, M. Chea, G. Boisserie, J. Alvarez, and P. Bergonzo, "Diamond dosimeter for small beam stereotactic radiotherapy," *Diamond and Related Materials*, vol. 33, pp. 63–70, 2013.

[134] P. W. Hoban, M. Heydarian, W. A. Beckham, and A. H. Beddoe, "Dose rate dependence of a PTW diamond detector in the dosimetry of a 6 MV photon beam," *Physics in Medicine and Biology*, vol. 39, pp. 1219–1229, aug 1994.

[135] D. B. Douglas, J. L. Muldermans, and M. Wintermark, "Neuroimaging of brain trauma," *Current Opinion in Neurology*, vol. 31, no. 4, pp. 362–370, 2018.

[136] N. J. Lee, R. H. Hruban, and E. K. Fishman, "Pancreatic neuroendocrine tumor: review of heterogeneous spectrum of CT appearance," *Abdominal Radiology*, pp. 1–10, 2018.

[137] E. Mohamed, R. Jackson, C. M. Halloran, and P. Ghaneh, "Role of Radiological Imaging in the Diagnosis and Characterization of Pancreatic Cystic Lesions: A Systematic Review," *Pancreas*, vol. 47, no. 9, pp. 1055–1064, 2018.

[138] T. Calliess, M. Ettinger, P. Savov, R. Karkosch, and H. Windhagen, "Individualized alignment in total knee arthroplasty using image-based robotic assistance," *Der Orthopäde*, vol. 47, no. 10, pp. 871–879, 2018.

[139] A. Toepfer, N. Harrasser, M. Recker, U. Lenze, F. Pohlig, L. Gerdesmeyer, and R. von Eisenhart-Rothe, "Distribution patterns of foot and ankle tumors: a university tumor institute experience," *BMC Cancer*, vol. 18, no. 1, p. 735, 2018.

[140] F. Bachmair, *CVD Diamond Sensors In Detector For High Energy Physics*. PhD thesis, ETH Zürich, 2016.

[141] R. P. Feynman, R. B. Leighton, and M. L. Sands, *The Feynman Lectures on Physics*. New York: Hachette Book Group USA, 2010.

[142] E. B. Podgorsak, ed., *Radiation Oncology Physics: A Handbook for Teachers and Students*. International Atomic Energy Agency, July 2005.

[143] J. H. Hubbell and S. M. Seltzer, "Tables of X-ray mass attenuation coefficients and mass energy-absorption coefficients 1 keV to 20 MeV for elements Z=1 to 92 and 48 additional substances of dosimetric interest," tech. rep., National Inst. of Standards and Technology-PL, Gaithersburg, MD (United States). Ionizing Radiation Div., 1995.

[144] J. F. Fowler and F. Farmer, "Conductivity induced in Insulating Materials by X-rays," *Nature*, vol. 173, no. 4398, pp. 317–318, 1954.

[145] N. W. Ashcroft and N. D. Mermin, *Solid State Physics*. New York: Holt, Rinehart and Winston, 1976.

[146] J. C. Gillespie, "Measurement of The Temperature Dependence of Radiation Induced Conductivity in Polymeric Dielectrics," Master's thesis, Utah State University, 2013.

[147] A. Rose, "An outline of some photoconductive processes," *RCA Review*, vol. 12, no. 3, pp. 362–414, 1951.

[148] M. Vissenberg and M. Matters, "Theory of the field-effect mobility in amorphous organic transistors," *Physical Review B*, vol. 57, no. 20, p. 12964, 1998.

List of Figures

List of Tables

Acknowledgements

Firstly, I would like to express my gratitude to my PhD thesis advisor **Prof. Dr. Werner Rühm** from Helmholtz Zentrum München, whose continuing assistance and thoughtful guidance paved the way for the successful completion of this thesis.

Prof. Dr. Michael John Atkinson, who made it possible for me to make this thesis at the School of Medicine of Technische Universität München, providing me his support as direct academic supervisor.

Prof. Dr. Shawn Bishop for the holistic and productive discussions during the Meetings of Thesis Committee, as external expert member from Physics Department of Technische Universität München.

I am especially grateful to **Prof. Dr. Achim Wixforth** (Institute of Physics of Augsburg Universität) and his group for the scientific and technical support on the development and the experiments with SAW devices. **Dr. Andreas Hörner** for the support on my experiments in his laboratory. **Alexander Reiner** for teaching me all necessary knowledge relating to SAW devices. **Matthias Küß** for the support on $LiNbO_3$ delay-lines. Moreover, I would like to convey my gratitude to **Andreas Spörhase** and **Adrian Mainka** for the technical support and guidance.

Dr. Matthias Schreck (Institute of Physics of Augsburg Universität) and his group for the development of diamond samples.

I am especially grateful to the **staff of Instytut Technologii Elektronowej (Institute Electronic Technology)** in Warsaw, Poland, for the support concerning the development of AlGaN/GaN−HEMT samples.

I would also like to express my gratitude to **Florian Wagner** (Helmholtz Zentrum München) for the technical support during the radiation experiments in SSDL/HMGU.

I am grateful to **Dr. Marek Wielunski** for all the scientific guidance prior leaving Helmholtz Zentrum München.

I acknowledge **Dr. Vedran Bandalo** for teaching me all necessary knowledge about clean room related techniques, as well as for the scientific support whenever was necessary, prior and after leaving Helmholtz Zentrum München.

I feel inclined to express my gratitude to **Dr. John Howgate** and **Martin Schmid** for the numerous scientific and technical discussions prior leaving Helmholtz Zentrum München.

Last but not least, I am grateful to **my parents, Panagiotis and Kaiti,** to **my brother, Efthimis,**, as well as to **my life partner, Silvia Massaro,** for their support throughout this scientific journey.